Imperial College London

Imperial College London

Department of Physics

Characterisation and Control
of Trapped-ion Qubit

Author:

Chungsun Lee

Supervisor:

Prof. Richard Thompson

Declaration

I hereby declare that the work presented in this thesis is original unless otherwise referenced and acknowledged appropriately.

Abstract

Trapped ions are one of the promising platforms that realise a quantum bit, or qubit, in quantum computation. The fundamental quantum operations, such as single- and two-qubit gates, have been demonstrated. However, the fidelity of a quantum gate is easily compromised by inadequate qubit initialisation or incorrect settings of experimental parameters. This thesis aims to address those issues, allowing for the complete coherent control of the trapped ion qubit.

This thesis describes the construction and testing of a new ion trap apparatus for optimal control of a trapped ion qubit, which ideally makes the quantum gates more robust against experimental parameters.

This thesis extends the two-level Ramsey interferometry to higher order in a trapped ion. Creation and certification of the motional superposition require excellent control of the trapped ion qubit. We prepare a motional superposition state with undesired AC Stark shift due to the off-resonant carrier compensated by our compensation scheme. We successfully certify the superposition consists of three motional Fock states, $(|0\rangle + |1\rangle + |2\rangle)/\sqrt{3}$, using a robust certifier derived from statistical moments of the interference pattern.

The thesis presents the results of a Bayesian estimator that estimates the Rabi frequency and detuning frequency by processing the measurement records via Bayes' theorem. We compare the estimate from the Bayesian estimator and the standard fitting method, in which Rabi frequency and detuning are estimated by fitting the Rabi oscillation and the frequency spectrum of the ion, and found the Bayesian estimator can estimate those unknown parameters as accurately as the standard fitting method, but only requires less than one-hundredth of measurements necessary for the fitting method.

We also experimentally demonstrate measurement-based cooling, which is an alternative way to cool the ion to its ground state. Contrary to resolved sideband cooling, which is routinely used for the ground state cooling in our experiment, this cooling method probabilistically prepares the ion in its motional ground state. We perform a state-dependent mapping operation that maps the ion's atomic state to either $|g\rangle$ or $|e\rangle$ conditioned on its motional states: the ion's atomic state is mapped to $|e\rangle$ if its motional state is $|0\rangle$; otherwise the ion's atomic state is mapped to $|g\rangle$.

The following projective measurement of the atomic state of the ion enables the discrimination between the motional ground state and the motional excited states. Therefore we can prepare the ion in the motional ground state by selecting the instances where the ion is measured to be in $|e\rangle$, which heralds the motional ground state.

In the near future, the group will begin a project to implement and evaluate recent proposals for making quantum gates robust against a mis-set of frequency using a polychromatic light field.

Acknowledgements

keep working hard when I was worried because of slow progress during the COVID pandemic.

Contents

List of Figures

Chapter 1

Introduction

1.1 Background and Motivation

The profound advancements in science and engineering in the last few decades would not be possible without the invention of the computer, and the sustained improvement of technology comes along with the continuing improvement of the computing power of the digital computer; in modern scientific research, a supercomputer is widely used and plays an essential role. However, for the last few decades, certain types of problems have been proved to be fundamentally intractable by the classical computer; for instance, factorising large composite integers cannot be efficiently completed even by the world's fastest supercomputer. This fact acts as the fundamental foundation of modern cryptography [1].

Simulating a quantum system is one such problem. In 1982, Richard Feynman [2] proposed the idea of a *quantum simulator*, arguing that conventional Turing machines, which provide the technological basis for the digital computer, could not efficiently simulate a quantum system due to the probabilistic nature of a quantum system: simulating a quantum system requires an exponential increase in the size of computational resources with the growth in scale of the system. He argues that a quantum computer could address those issues, but he failed to provide a comprehensive methodology – it was just an early theoretical proposal.

The first theoretical groundwork for quantum computation was done by David Deutsch [3]. He proposed the existence of a universal quantum Turing machine that processed information using the probabilistic nature of quantum mechanics. In 1992, he expanded on this idea in partnership with Richard Jozsa [4] as they demonstrated the Deutsch-Jozsa algorithm; the first quantum algorithm that tests whether a hidden Boolean function f, which takes n bits as an input and returns either 0 or 1, is constant or balanced. If it is balanced, the function gives 0 or 1 equally for many inputs, otherwise, it is constant and always outputs 0 or 1 regardless of the input.

They also observed that this algorithm was exponentially faster than any classical algorithm. Although the algorithm does not provide any practical application, it was the first quantum algorithm to demonstrate that quantum computing can bring exponential speed-up to certain computational problems. Meanwhile, Seth Lloyd [5] showed that quantum computers, even with tens of qubits, can simulate another quantum system much more efficiently than the latest supercomputer can.

In 1994, Peter Shor [6] published a paper that demonstrated a quantum algorithm for integer factorisation, Shor's algorithm. The algorithm drew considerable attention from computer scientists as well as physicists because this algorithm enables a quantum computer to solve the factorisation of large integers, an intractable problem for classical Turing machines because of the exponential increase in the size of the required computing resources. The tremendous difficulty of the factorisation problem even when using the latest supercomputer underpins the current cryptosystem. Quantum computation has attracted massive attention as those algorithms have theoretically proved that quantum computers are practically valuable, providing an exponential acceleration in some applications.

In 2019, there was a monumental event in the history of quantum information science. Google experimentally demonstrated quantum supremacy for the first time using their superconducting circuits that accommodate 53 superconducting qubits [7]. It was the first experimental demonstration of quantum supremacy. Using their superconducting qubits, they perform a calculation that is expected to take more than a million years even with the world's best supercomputer within 200 seconds. Although the calculation itself the quantum computer performs has no practical interest, this provides a milestone of quantum information science as it experimentally proves a quantum computer can provide exponential speed-up of a quantum computer compared to its classical counterpart.

The feasibility of quantum computing has been proved not only theoretically but also experimentally. As the discovery of several quantum algorithms promised that a quantum computer could outperform a classical computer when dealing with particular problems, researchers became more interested in the physical realisation of a quantum computer. In 2000, DiVincenzo suggested specific requirements we have to consider to physically realise the quantum computing device, the so-called DiVincenzo's criteria [8]:

- A scalable physical system with well-characterised qubits

- The ability to initialise the state of the qubits to a simple fiducial state

- Long relevant decoherence times

- A 'universal' set of quantum gates

- A qubit-specific measurement capability

Until now, many different platforms have been experimentally demonstrated, fulfilling the creteria above : superconducting circuits [9, 10, 11, 12, 13, 14], nitrogen vacancy (NV) centres [15, 16, 17, 18], silicon [19, 20, 21, 22, 23], ion traps [24, 25, 26, 27, 28, 29]. However, the development of quantum computing is still in its infancy, and it is still uncertain which physical system would be ideal for making the quantum computer a reality. However, researchers and engineers have reached a consensus that the creation of a quantum computer is a feasible goal [1, 30].

Among the many possible candidates, an ion trap has been considered to be one of the promising candidates to realise the quantum computer in reality. An ion trap is a device where the charged particles are confined in free space, providing a system well isolated from its environment. The atomic structure of the ion provides a long-lived state, which can define a qubit, and applicable transitions that can be used for cooling and manipulation of the ion. Each trapped ion can act as a qubit, and well-studied light-matter interaction via coherent light sources such as a laser can allow for coherent manipulation of the qubits. When multiple ions are trapped in the same trap, the ions share the harmonic motion as the ions interact with each other via long-range Coulomb interaction. This shared motional degree of freedom can be used as the quantum bus that transports the quantum information between the ions, realising the multi-qubit operation, which is essential for a large-scale quantum computing device.

In 1995, Ignacio Cirac and Peter Zoller [31] suggested a viable approach of creating the controlled-NOT gate via a collective motional degree of freedom that can be excited by a laser field directed at each target ion, as well as a two-qubit logic operation with a trapped ion. The gate was experimentally realised later that same year [32]. However, it imposes strict requirements that the ion must be in its motional ground state. A few years later, In 1999, Mølmer and Sørensen proposed a two-qubit gate, namely the Mølmer–Sørensen (MS) gate, by using state-dependent force generated by a bichromatic light field [33, 34]. The MS gate relaxes the ground state cooling requirement, which is imposed on the Cirac-Zoller gate. This scheme was experimentally implemented in Be^+ ions in 2000 [35]. Since then, the fidelity of the two-qubit gate was improved to 99.6% for optical qubits [36] and 99.91% for hyperfine qubits [37].

However, as the number of trapped ions increases (i.e. a large-scale quantum computer), the cooling becomes more difficult, and the gate is more sensitive to experimental conditions, requiring a better understanding of the environment and capability of more robust control of the trapped ion qubits. There have been many variants of the MS gate scheme where more complicated pulse sequences are employed [38, 39].

The focus of this thesis is to build a system capable of doing this and to demonstrate the capability of our system to more rapidly characterise the trapped ion qubit and control the qubit more robustly against the imperfection of the experiment. Our long-term goal is to demonstrate the experimental implementation of those robust two-qubit gate schemes proposed, proving the viability of quantum computation with the presence of noise and disturbance of the system.

1.2   Outline of Thesis

The rest of thesis will be structured as the follows :

- **Chapter 2** provides an underlying theory of a linear Paul trap. First, we treat an ion as a classical particle and describe the ion's motion using a classical equation of the motion derived from the ion's electromagnetic interaction with the applied field. We next quantise the ion's motion, providing a complete quantum mechanical picture of the trapped ion: atomic state and a quantum harmonic oscillator. Also, this chapter aims to give a concise explanation of how we can use the trapped ion as a qubit, showing the relevant atomic transitions of $^{40}\text{Ca}^+$ for Doppler cooling, state detection, state initialisation, and manipulation of the ion.

- **Chapter 3** begins with a succinct summary of how an ion confined in an ion trap interacts with an applied light field, showing how the atomic state and the motional state of the ion can be coherently entangled via the sideband transitions. The second section explains the Raman interaction, which can make the effective coupling between the Zeeman sublevels of $\text{S}_{1/2}$, allowing the two Zeeman sublevels to form a qubit (i.e. Zeeman qubit).

- **Chapter 4** explains how we can cool the ion down to its motional ground state using laser cooling methods, including Doppler and sideband cooling. The chapter begins with a quantitative description of Doppler cooling, which rapidly cools the ion to the Doppler limit, and the following section gives a concise explanation of resolved sideband cooling with two different schemes: pulsed and continuous sideband cooling.

- **Chapter 5** presents the brief descriptions of each experimental apparatus, which includes lasers at different wavelengths, and optics to steer the beams to the trap and collect the florescence from the ion.

- **Chapter 6** presents the initialisation of the new $729\,\text{nm}$ laser.

- **Chapter 7** explains why off-resonant coupling is unavoidable and how the undesirable off-resonant coupling influences the coherent operations on the ion. The chapter also presents the methods to counteract the adverse effects, and the experimental demonstration of creating motional superposition states and verification of motional coherence.

- **Chapter 8** explains the working principle of Bayesian inference and how we can apply the Bayesian inference to characterise a trapped-ion qubit (Rabi frequency and detuning frequency of the driving laser).

- **Chapter 9** explains the general principle of measurement-based cooling, which can be applied to an oscillator coupled to an auxiliary level (e.g. trapped ions). As rapid adiabatic passage (RAP) is the primary operation, the chapter gives a brief introduction of RAP and the results of the transfer efficiency achieved through RAP. The chapter also presents the measured cooling efficiency of the measurement-based cooling with the use of RAP.

- **Chapter 10** summarises experimental results presented in this thesis and proposes possible future projects where the results can be applied to extend the ideas discussed in the thesis for different purposes.

Chapter 2

The Linear Paul Trap

An ion trap provides a well-isolated quantum system by localising and confining atomic particles in free space. Thus, an ion trap has been used in different quantum applications ranging from precision frequency metrology to quantum computation. The basic idea of an ion trap is to confine charged particles in free space using their electromagnetic interaction with applied fields. In simple terms, three-dimensional confinement requires a potential that has a minimum in space, leading to restoring forces in all three directions. An electrostatic field would be the most straightforward choice if it could be set in the form of a three-dimensional harmonic potential. Earnshaw's theorem, however, clearly states that an electrostatic potential cannot be set in such a configuration [40]. Two common configurations are used to circumvent that limitation imposed by the theorem – Penning and Paul traps. The Penning trap uses a combination of electrostatic and magnetic fields [41], while the Paul trap only uses an electric field. However, the field consists of static and time-varying components and produces a time-averaged trapping force [42].

In this chapter, general working principles of a linear Paul trap, which is the configuration used in our experiment, will be discussed. The classical and quantum mechanical dynamics of a single trapped ion are presented. Also, this chapter discusses the use of $^{40}\text{Ca}^+$, which is our choice of ion species, as a qubit – the atomic energy structure of $^{40}\text{Ca}^+$, how to create and load the ion into the trap, and our method to detect the qubit state of the ion.

2.1   Trapping an Ion

A generalised harmonic potential that leads to trapping force in three dimensions is given by

$$\phi(x, y, z) = ax^2 + by^2 + cz^2, \tag{2.1}$$

6
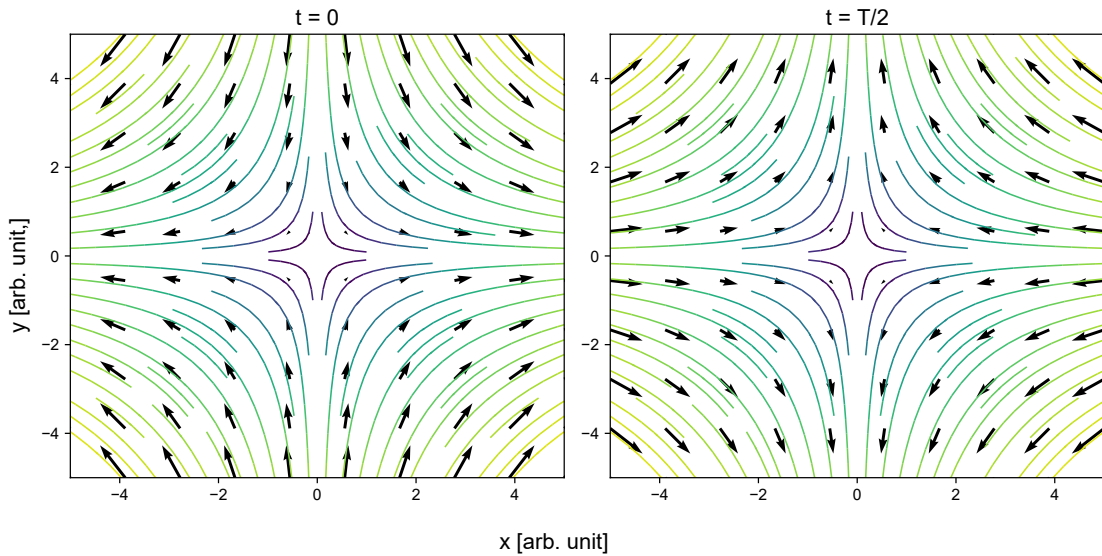
Figure 2.1: Contour plot of an equipotential surface of the time-varying quadrupole potential applied for a Paul trap on a radial plane with vectors indicating the direction of resulting forces at $t = 0$ (left) and $t = T/2$ (right). In the radial plane, one axis becomes stable and the other unstable, and each axis alternates between trapping and anti-trapping with a period of T, leading to a time-averaged radial trapping force.

where a, b, and c are constants, and the electric field derived from this electric potential $\phi(\mathbf{r})$ where $\mathbf{r} = \{x, y, z\}$ is

$$\vec{E}(\mathbf{r}) = -\nabla\phi(r) = -2ax\hat{\boldsymbol{\imath}} - 2by\hat{\boldsymbol{\jmath}} - 2cz\hat{\boldsymbol{k}}. \tag{2.2}$$

Gauss's law states that the divergence of an electric field must be zero unless extra charges are present $\nabla \cdot \mathbf{E} = 0$. Therefore, at least one of coefficients (a, b, c) in Eqn. (2.1) must be negative unless all coefficients are zero, which is equivalent to free space. In other words, the ion is pushed away from the trap centre in at least one direction, which is anti-trapping. To overcome this problem, the Paul trap employs an electrostatic field superimposed on the time-dependent oscillating field. As illustrated in Fig. 2.1, the time variation of the field makes each axis alternate between trapping and anti-trapping. With appropriate settings of frequency and amplitude of the applied oscillating field, a time-averaged trapping potential in all three dimensions can be achieved [43]. A more rigorous mathematical description of the trapping technique will be presented in section 2.1.1.

2.1.1 Classical Motion of a Trapped Single Ion

A linear Paul trap, which is a variant of the conventional Paul trap, is used in our experiment. The linear Paul trap allows for more optical access than the conventional Paul trap arrangement, whose electrodes are in hyperbolic shape. More optical access
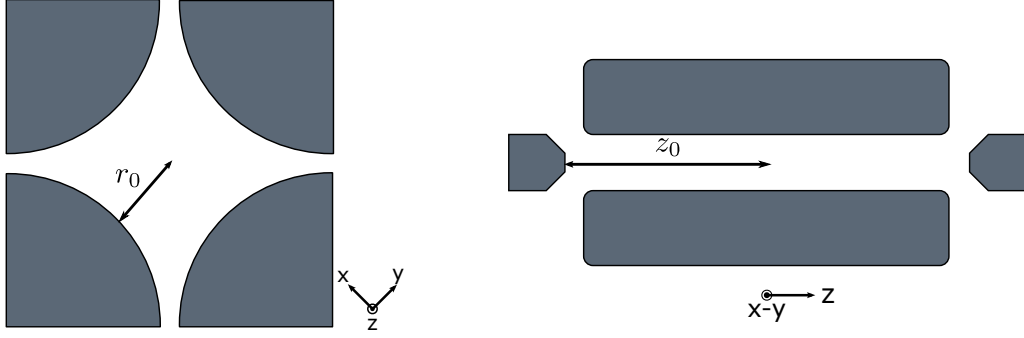
Figure 2.2: Schematic diagram of linear Paul trap based on a quadrupole mass analyser. Left: Electrodes for the Paul mass filter. The circular shaped inner surface results in a quadrupole potential. Right: Side view of the trap. A pair of end-caps is added to the electrodes shown in the left image to confine the ion axially.

is advantageous in state detection, where photons emitted from ions are collected, and in laser-induced logic operations. The symmetry of the linear Paul trap along the trap axis makes an elongated rf zero-potential along the trap axis, and this makes the trapped ions form a linear chain of single ions aligned along the trap axis when multiple ions are trapped. Each ion is stored close to the zero-potential line where ions experience reduced micromotion, and the actual potential near the trap axis can be approximated to a quadrupole-like shape [44, 45]. An oscillating rf field of the form $V_{ac} \cos \Omega t$ is applied to one pair of diagonally opposite radial electrodes, and the other pair is grounded. Also, a static voltage V_{dc} is applied to two end-caps. The resulting electric potential generated by applied voltages to those electrodes is in the following form:

$$\phi(x, y, z, t) = \frac{k_r V_{ac} \cos(\Omega t)}{2r_0^2} \left(x^2 - y^2\right) + \frac{k_z V_{dc}}{2z_0^2} \left(2z^2 - x^2 - y^2\right), \qquad (2.3)$$

where r_0 and z_0 (defined in Fig. 2.2) are trap dimensions, and k_r and k_z are geometric factors, which are reduced from the ideal of unity to account for non-hyperbolic shape of electrodes. An ion with mass m and charge $-e$ placed in electric field $\vec{E} = -\nabla \phi(r, t)$ experiences a force $\vec{F} = -e\nabla \cdot \vec{E}$. Thus, the classical equations of motion can be written as

$$\frac{\partial^2 x}{\partial t^2} + \left[\frac{-ek_z V_{dc}}{mz_0^2} + \frac{ek_r V_{ac}}{mr_0^2} \cos \Omega t\right] x = 0$$

$$\frac{\partial^2 y}{\partial t^2} + \left[\frac{-ek_z V_{dc}}{mz_0^2} - \frac{ek_r V_{ac}}{mr_0^2} \cos \Omega t\right] y = 0 \qquad (2.4)$$

$$\frac{\partial^2 z}{\partial t^2} + \frac{2qk_z V_{dc}}{mz_0^2} z = 0.$$

8

An axial confinement is achieved by the static field, and it is straightforward to show that the axial motion is a simple harmonic oscillator at frequency

$$\omega_z = \sqrt{\frac{2qk_zV_{dc}}{mz_0^2}}.$$ (2.5)

The radial equation is more complicated. However, by introducing new parameters a_u and q_u for $\{u = x, y\}$, which are defined by experimental conditions,

$$a_x = a_y = -\frac{4qk_zV_{dc}}{mz_0^2\Omega^2}$$
$$q_x = -q_y = \frac{2qk_rV_{ac}}{mr_0^2\Omega^2},$$ (2.6)

the equations of radial motion (in $x - y$ plane) in Eqn. (2.4) can be transformed into the Mathieu equation[46], which is a special form of a linear differential equation:

$$\frac{\partial^2 u}{\partial t^2} + [a_u + 2q_u \cos\Omega t]\frac{\Omega^2}{4}u = 0.$$ (2.7)

The Mathieu equation Eqn.(2.7) can be solved using Floquet's theorem [47], and its solutions are given as

$$u(t) = A\sum_{n=-\infty}^{\infty} C_{2n}\cos(\beta+2n)\frac{\Omega t}{2} + B\sum_{n=-\infty}^{\infty} C_{2n}\sin(\beta+2n)\frac{\Omega t}{2},$$ (2.8)

where A and B are constants determined by the initial position and velocity of the ion, and C_{2n} are the amplitudes of the Fourier components of the solution. The oscillation of the ion's motion is characterised by

$$\omega_u = \frac{1}{2}\beta_u\Omega,$$ (2.9)

where β is written as an iterative fraction of a_u and q_u:

$$\beta_u^2 = a_u + \cfrac{q_u^2}{(\beta_u+2)^2 - a_u - \cfrac{q_u^2}{(\beta_u+4)^2-q_u-\cfrac{q^2}{(\beta_u+6)^2-q_u-\cdots}}}$$
$$+ \cfrac{q_u^2}{(\beta_u-2)^2 - a_u - \cfrac{q_u^2}{(\beta_u-4)^2-q_u-\cfrac{q^2}{(\beta_u-6)^2-q_u-\cdots}}}$$ (2.10)

The solutions can be either stable or unstable, depending on the choices of a_u and q_u. Fig. 2.3 shows that there is a region in parameter space of a_u and q_u where the ion is stably trapped. If $q_u < 0.4$ and $a_u \ll q_u$, the solutions (Eqn. 2.8) can be simplified
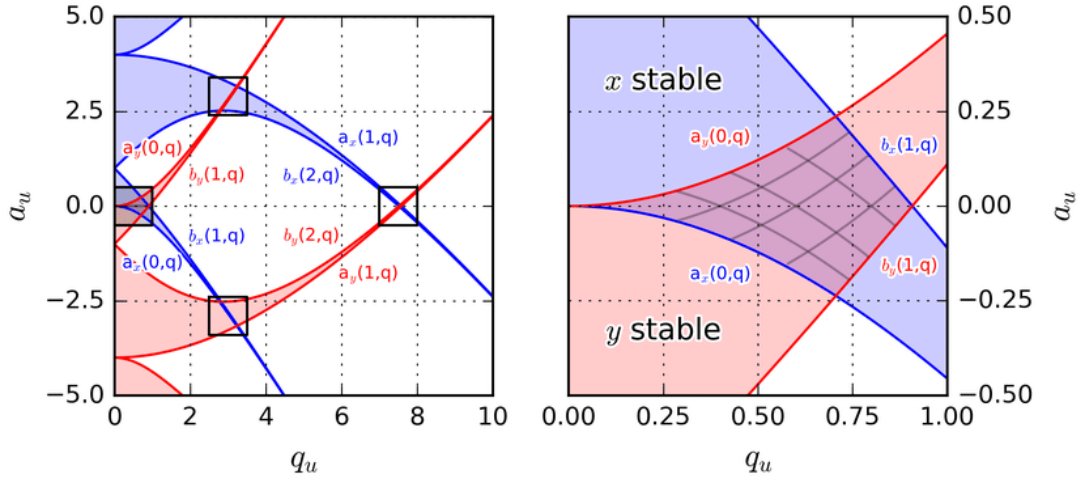
Figure 2.3: Stability diagram for the Mathieu equation as a function of trap parameters (a_u, q_u), showing stability regions for the ion in the linear rf trap. Left: the trap parameters have to lie within the overlapping regions. Right: the zoom-in of the boxed area in the figure on the left. The diagram is adapted from Johannes [48].

by using an adiabatic approximation [49, 50]:

$$u(t) = R_u \cos \omega_u t \left(1 + \frac{q_u}{2} \cos \Omega t \right) \tag{2.11}$$

with

$$\beta_u = \sqrt{a_u + \frac{q_u^2}{2}}, \quad \text{and} \quad \omega_u = \frac{1}{2} \beta_u \Omega, \tag{2.12}$$

where the first term describes the harmonic oscillation with the frequency ω_u, which is called secular motion, and the second represents additional contribution at the frequency Ω, which is referred to as micromotion. The adiabatic approximation ensures the amplitude of the micromotion is small compared to that of the secular motion; the micromotion is usually ignored.

2.1.2 Excess Micromotion

In an ideal case of trapping potential, the minimum of the static field coincides with the null of the rf field. There are, however, several occasions where the minimum of static potential and rf null are misaligned – for example, the phase of the rf field applied to each blade is different, the electrodes are misaligned during the assembly, or unevenly distributed patches of neutral calcium are created on the surface of the trap electrodes during loading of the ion. The misalignment of the two fields effectively introduces an additional static field to the trapping field $E_d u_0$, and consequently, the equations of motion are modified as follows:

10

$$\frac{\partial^2 u}{\partial t^2} + [a_u + 2q_u \cos \Omega t] \frac{\Omega^2}{4} u = \frac{qE_d u_0}{m}. \tag{2.13}$$

The solution of Eqn. (2.13) resembles Eqn. (2.11):

$$u(t) = [u_{i,0} \cos (\omega_{i,1} t) + u_{u,1}][1 + \frac{q_u}{2} \cos (\Omega t)], \tag{2.14}$$

where $u_{u,1}$ quantifies the strength of the additional contribution to the micromotion, which is usually referred to as excess micromotion. The amplitude of the excess micromotion is proportional to the displacement of the ion. The excess micromotion can significantly affect the ion motion, degrading the fidelity of coherent operation on a trapped ion. Thus, it is crucial to measure and compensate for excess micromotion. An in-depth discussion of excess micromotion compensation and the experimental results will be presented in Section 5.5.

2.2 Quantisation of Motion of Trapped Single Ion

As discussed in the previous section, the dynamics of a single trapped ion follow a trajectory described by a harmonic oscillator. In other words, the ion can be considered to be confined by a harmonic quasi-potential. This argument is valid even in a quantum regime, and therefore the motion of the ion can be quantised as motional Fock states $|n\rangle$ that are the solutions of the quantum harmonic oscillator. The harmonic frequency is given by the frequency of secular motion, and the resultant Hamiltonian can be written as a three-dimensional harmonic oscillator:

$$\hat{H} = \sum_u \frac{1}{2} \omega_u \hat{a}_u \hat{a}_u^\dagger, \quad u \in \{x, y, z\}. \tag{2.15}$$

ω_u is harmonic frequency, and $\hat{a}_u$ ($\hat{a}_u^\dagger$) is an annihilation (creation) operator.

2.3 $^{40}\text{Ca}^+$ as a Qubit

We historically choose the $^{40}\text{Ca}^+$ ion for several reasons. Calcium is one of the alkali-earth metals, and its atomic structure becomes 'alkali-like', which has a simple energy level structure, when it is singly ionised. Also, all transitions involved in laser cooling and coherent manipulation of the ion can be addressed by a commercially available diode laser, providing inexpensive and easy solutions for realising a trapped ion qubit.
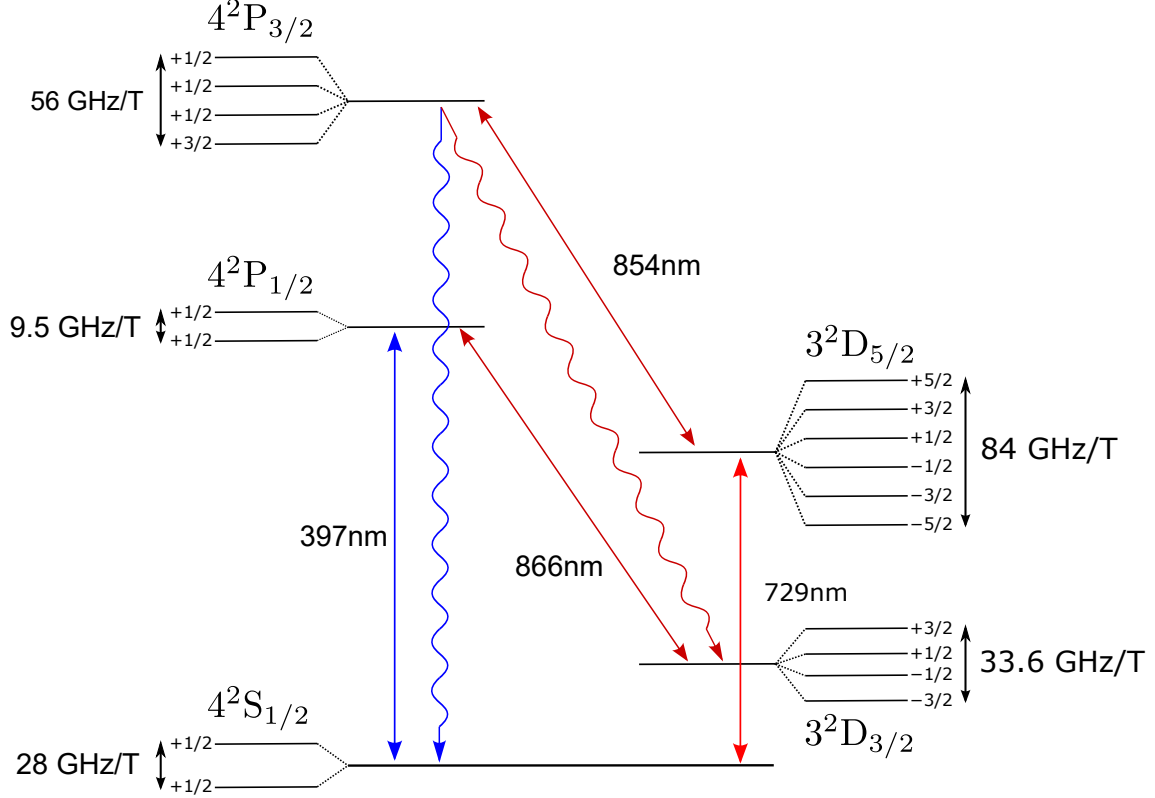
Figure 2.4: Energy diagram of $^{40}\text{Ca}^+$. All relevant transitions used in experiments described in this thesis are shown – solid lines indicate transitions actively driven by lasers, and the curly arrows represent spontaneous decay from the $P_{3/2}$ state to $S_{1/2}$ and $D_{3/2}$.

2.3.1 Atomic Structure of $^{40}\text{Ca}^+$

Fig. 2.4 shows an atomic structure diagram of $^{40}\text{Ca}^+$ with all transitions relevant to our experiment. We denote $S_{1/2}$ and $D_{5/2}$ as $|g\rangle$ and $|e\rangle$, respectively, and use those states as a qubit, which is a basic unit of quantum information. $D_{5/2}$ is meta-stable state with a lifetime of $\approx 1.2\,\text{s}$ [51], which limits the ultimate coherence time of the qubit. A coupling between these states is made through a weak quadrupole transition $S_{1/2} \longleftrightarrow D_{5/2}$ mediated by a narrow-linewidth laser at $729\,\text{nm}$. A dipole transition $S_{1/2} \longleftrightarrow P_{1/2}$ at $397\,\text{nm}$ is exploited for Doppler cooling. As this transition is cyclic, an ion repeatedly absorbs and emits the photons at $397\,\text{nm}$. A fraction of the population in the $P_{1/2}$ and $P_{3/2}$ states can decay to the $D_{3/2}$ state. However, this population is pumped back to the $P_{1/2}$ state by driving a dipole transition $D_{3/2} \longleftrightarrow P_{1/2}$ at $866\,\text{nm}$. The branching rate to $D_{3/2}$ is low (6%); this state is often ignored when we discuss the dynamics related to the qubit.

2.3.2 State Detection

At the end of quantum computation, the stored information is inferred by measuring the state of the ion or qubit. In an ion trap, state detection is performed via state-
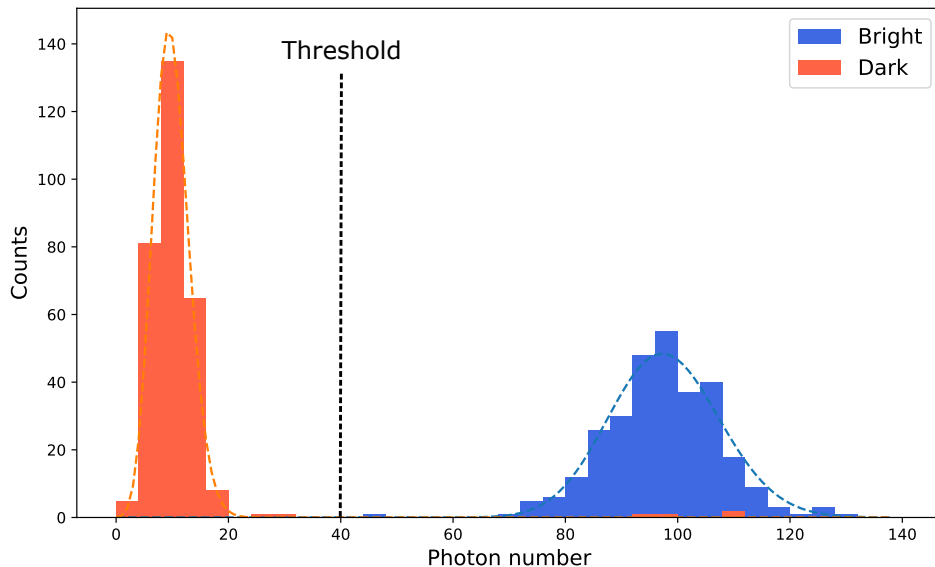
Figure 2.5: Histogram of photon counts collected during the detection period of 5 ms. The ion is prepared in the 'dark'and 'bright'state 300 times for each state. Bright and dark states can be distinguished by thresholding the measurement records. There are few occasions where the ion is prepared in the dark state, but those ions scatter as many photons as the ions in the bright state, which reduce detection fidelity. See the text for more details

dependent fluorescence as only one of the qubit states ($S_{1/2}$) is coupled to a detection laser at 397 nm[52, 53, 54]. In our trap, the qubit is defined by one of $S_{1/2}$ and $D_{5/2}$ manifolds. When the Doppler transition $S_{1/2} \leftrightarrow P_{1/2}$ is driven by a laser at 397 nm, the ion is projected into either $S_{1/2}$ or $D_{5/2}$, and the ion scatters the photons from the laser if and only if the ion is in the $S_{1/2}$ state. We measure the photons emitted from the ion using a photomultiplier tube (PMT) or an electron-multiplying CCD (EMCCD). We also denote $S_{1/2}$ and $D_{5/2}$ as bright and dark states. The detection can be modelled as a series of independent and random events, and the resulting distribution follows a Poissonian distribution of the number of photons n being detected in a time interval t_D:

$$P(n) = \frac{e^{-\lambda}\lambda^n}{n!}, \tag{2.16}$$

where R is the scattering rate, which varies dependent on the qubit state, and $\lambda = Rt_D$ is a mean photon number. If the ion is in the dark state, the coefficient R includes only photon scattering from the background R_d; otherwise, R consists of photon scattering from the ion R_b as well as background counts R_d. The distributions have different mean photon numbers, and consequently, this state-dependent fluorescence allows for discrimination between the bright and dark states.

Fig. 2.5 shows histograms of photon counts collected during 5 ms when the ion is prepared in bright ($S_{1/2}$) and dark ($D_{5/2}$) states 300 times each. The two

13

distributions are clearly separated without significant overlap. However, some of the dark counts lie within the bright distribution, reducing detection fidelity to 98.9%. This might be due to the finite lifetime of the $D_{5/2}$ state. The ion in the dark state can spontaneously decay to $S_{1/2}$ during the detection period and stays in $S_{1/2}$ for the rest of the detection period although the ion is initially in the $D_{5/2}$ state. If this is the case, we can alleviate this issue by reducing the detection time t_D so that the ion in $D_{5/2}$ is less likely to decay during the detection period, but the two distributions are then less separated as the mean photon numbers get closer to each other.

The detection efficiency of 98.9% might be underestimated. When we prepare the ion in $D_{5/2}$, we use a resonant π pulse. However, the π pulse might not be perfect, and there is no way to guarantee that the ion is perfectly prepared in the $D_{5/2}$ state before performing the measurement. This might suggest that the distribution overlap should be attributed to imperfect state preparation of the dark state.

For the Raman qubit, the qubit states are defined by $S_{1/2,\pm 1/2}$. In this case, the qubit states cannot be distinguished via state-dependent fluorescence because both states scatter the laser at 397 nm. Hence, using a π pulse of the 729 nm laser that is resonant to one of the $S_{1/2}$ states, we completely transfer the population of either of the $S_{1/2}$ sublevels to $D_{5/2}$, so that the standard detection method using the 397 nm laser can be applied to discriminate one qubit state from the other.

2.3.3   State Preparation
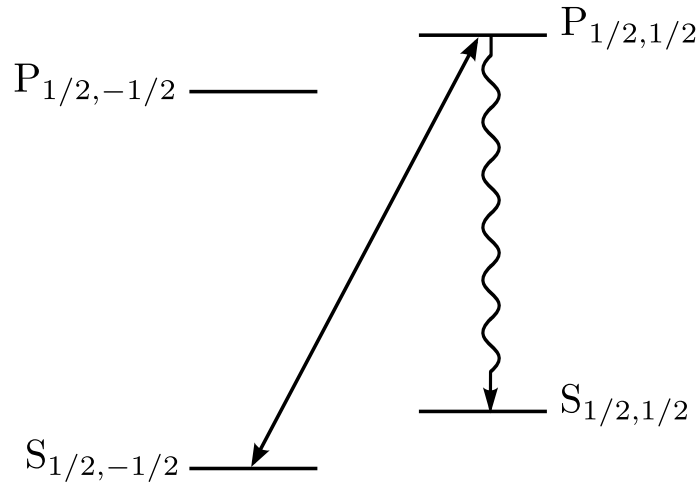
Figure 2.6: State preparation of $S_{1/2,1/2}$ via optical pumping. The σ_+ transition continuously excites the $S_{1/2,-1/2}$ state until the $P_{1/2,1/2}$ state spontaneously decays to $S_{1/2,1/2}$.

At the beginning of each experiment, we must first initialise the state of the ion to a specific state of $S_{1/2}$ – we need a well-defined ground state. Nevertheless, both sublevels of $S_{1/2}$ state can be populated during Doppler cooling because the ion in

either the $P_{1/2}$ or the $P_{3/2}$ state can spontaneously decay to both sublevels of $S_{1/2}$ with equal probability. State preparation of a certain manifold of $S_{1/2}$ can be achieved by driving the dipole transition $S_{1/2} \leftrightarrow P_{1/2}$ with either σ_- or σ_+ polarised light, which is known as optical pumping [55]. For example, if we drive the σ_+ transition, the transition cycles between $S_{1/2,-1/2}$ and $P_{1/2,1/2}$ until the ion eventually decays to $S_{1/2,1/2}$ (see Fig. 2.6): once the ion decays to the $S_{1/2,1/2}$ state, then there is no state σ_+ transition can couple $S_{1/2,1/2}$ with, and the ion stays in the $S_{1/2,1/2}$ state.

2.4   Trap Electrodes
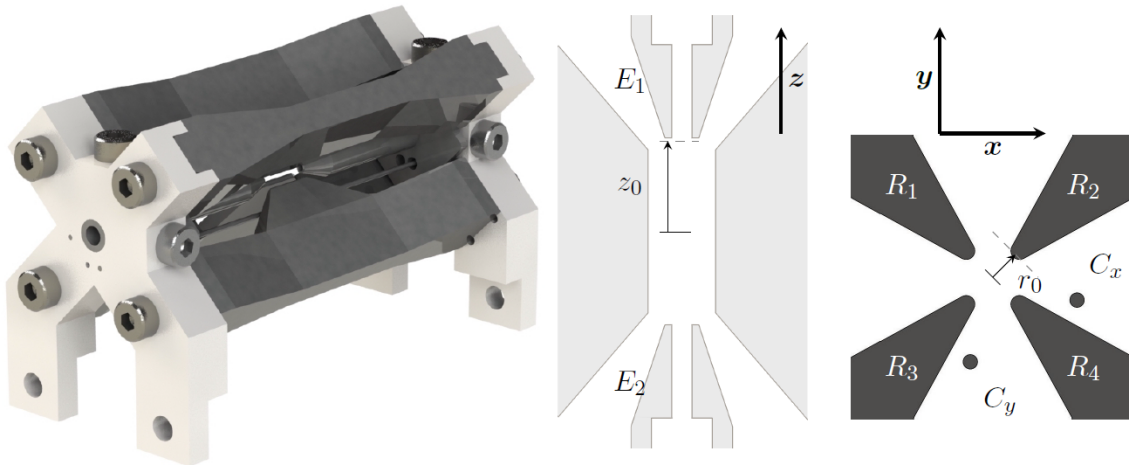
Figure 2.7: Trap electrodes consist of four blades and two end-caps: two end-caps are axially separated by $5.5\,\text{mm}$, and each blade is distanced $1\,\text{mm}$ from the trap centre ($z_0 = 2.75\,\text{mm}$ and $r_0 = 1\,\text{mm}$). This diagram is adapted from Oliver [56].

We recently built a macroscopic linear Paul trap. We adopt the design of the Innsbruck linear blade trap detailed in Ref.[45] – the trap electrodes consist of two end-caps and four blades as illustrated in Fig. 2.7. Using blades that replace hyperbolically shaped rf electrodes found in the Paul mass filter shown in Fig. 2.2 allows for better optical access, which benefits laser interrogation and fluorescence collection for state detection. There are holes $600\,\mu\text{m}$ in diameter in both end-cap electrodes. The holes allow us to project the laser along the trap axis, maximising the Lamb–Dicke (LD) parameter η associated with the axial motion, while nullifying the η associated with the radial motion, which we want to ignore in qubit manipulation. A time-dependent voltage at the trap frequency Ω is applied to one pair of diagonally opposite blades, and the other pair is grounded. The two end-caps are connected to a static voltage source. Those applied voltages generate the required time-varying and static electric fields in the forms described in Eqn. 2.3.

2.5   Loading
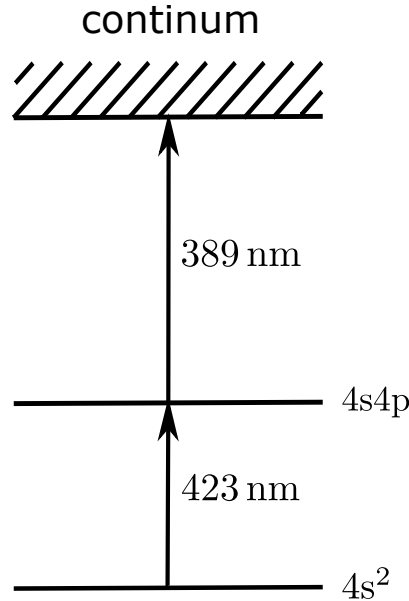
Figure 2.8: Energy diagram that shows the atomic states involved in isotope-selective photoionisation. Neutral calcium atomic particles are initially excited to the 4s4p state via a laser at 423 nm, and they are subsequently excited to the continuum state by a laser at 389 nm.

The trapped ion experiment starts with loading ions into the trap. The loading process has two steps. The first step is to produce an effusive beam of neutral calcium by resistively heating a tube filled with granules of calcium metal [57]. The tube has a hole facing the trap so that the emitted neutral calcium atoms are directed toward the trap centre. The second step is to ionise the neutral calcium. In the past, ionisation was achieved by bombarding calcium atoms with a high-power Nd:YAG laser. As this is a non-resonant process, the high-power laser can ionise not only the desired ^{40}Ca but also other calcium isotopes or potentially other species. Other calcium isotopes and other species cannot be properly Doppler cooled because the frequency of the Doppler-cooling laser is specifically tuned to address the dipole transition $S_{1/2} \leftrightarrow P_{1/2}$ of ^{40}Ca$^+$; those ions are seen as dark ions when they are illuminated by the Doppler beam because they do not scatter photons. We currently use isotope selective photoionisation (PI). The resonant photoionisation involves two processes [58, 59] – an electron bound to the outermost orbital of neutral calcium is excited to the 4s4p state via a laser at 423 nm and is subsequently excited to the continuum state via a laser at 389 nm (ionisation). The atomic ovens are positioned such that the resulting neutral atomic beam is mainly propagating perpendicular to the direction of the photoionisation lasers (see. Fig.2.9). As a result, the lasers experience minimised Doppler shift. A possible adverse consequence of the loading is to coat the trap electrodes with calcium, which alters the expected trapping field.

Therefore, we have carefully calibrated the current passed along the tube with the increase in pressure and typically use a current of 2.9–3.3 A to avoid depositing an excessive amount of calcium during the loading.
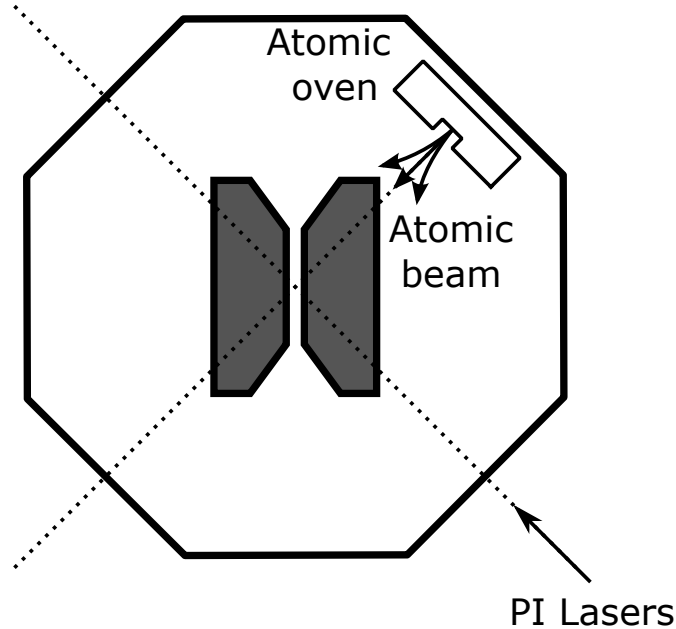
Figure 2.9: Geometry of the atomic beam effused from the atomic oven and photoionisation (PI) lasers. The atomic beam propagates perpendicular to the direction of the PI beams, minimising the Doppler shift due to moving atomic particles.

When we load ions, we switch on the two PI beams continuously, and ions are sequentially created and trapped one by one. This allows us to systematically control the number of ions trapped in our trap. However, sometimes we have more ions than we need (e.g. two ions when we need a single ion), and we have to extract some of the ions. We use Doppler heating for extraction. If we blue detune the Doppler beam, then the beam is heating the ions rather than cooling them, and the orbits of some ions become bigger and collide with the trap electrodes or a metal surface and are eventually ejected from the trap. We detune the Doppler beam roughly 100 MHz above the resonance for a few seconds and then detune the beam back to the frequency for Doppler cooling. We repeat this process until we have the number of ions we need. However, this method is trial and error, and we might lose all the ions.

Chapter 3

Atom-Light Interaction

This chapter focuses on the coherent interaction between an applied light field and a single trapped ion. This light–matter interaction is employed in many experimental techniques, such as coherent manipulation of a trapped ion and laser cooling. A trapped ion represents a composite quantum system that consists of an atomic internal state and a harmonic oscillator resulting from applied trapping potential. The internal and motional states of the trapped ion are coherently manipulated through the interaction between the ion and the resonant light field.

This chapter presents a theoretical foundation to describe the coherent interaction of the single ion tightly confined in the harmonic potential (i.e. a harmonic oscillator). In our experiment, two different routes are employed: a weak quadrupole transition addressing the $\mathrm{S}_{1/2} \leftrightarrow \mathrm{D}_{5/2}$ transition and Raman coupling, which is two-photon interaction, stimulating $\mathrm{S}_{1/2,-1/2} \leftrightarrow \mathrm{D}_{1/2,1/2}$ transition.

The interaction effectively couples the atomic internal state and motional degree of freedom.

3.1   Single Trapped Ion Interacting with Light

We use one of the ground states $\mathrm{S}_{1/2}$ and one of the meta-stable states $\mathrm{D}_{5/2}$ as basis states that constitute a qubit. We denote $\mathrm{S}_{1/2}$ and $\mathrm{D}_{5/2}$ by $|g\rangle$ and $|e\rangle$, respectively. These states are coupled via a weak quadrupole transition mediated by a narrow linewidth laser at $729\,\mathrm{nm}$. As shown in Fig. 2.4, $^{40}\mathrm{Ca}^+$ has many different atomic energy levels. However, if the frequency of a laser is tuned to the energy difference between $\mathrm{S}_{1/2}$ and $\mathrm{D}_{5/2}$, then the laser is far off-resonant to the other transitions, and we can ignore the other levels in our quantum picture and assume that the system is in a simple two-level structure. Here, we consider only the axial motion, which is along the trap axis, as our spectroscopic laser is directed along the trap axis. Consequently, any motion in the radial direction is not coupled to the laser. Thus, the unperturbed Hamiltonian, which consists of atomic H_e and motional H_m

degrees of freedom, is given as

$$\hat{H}_0 = \hat{H}_e + \hat{H}_m$$
$$= \frac{1}{2}\hbar\omega_{eg}\hat{\sigma}_z + \frac{\hat{p}^2}{2m} + \frac{m\omega_z^2\hat{z}^2}{2} \qquad (3.1)$$

where ω_{eg} and ω_z are the energy difference between $|g\rangle$ and $|e\rangle$ and the frequency of the harmonic oscillator along the trap axis, respectively, and $\hat{\sigma}_z$ is the Pauli operator. We consider a monochromatic light field that is described by the following equation:

$$\boldsymbol{E}_L(\boldsymbol{r}, t) = \frac{\hat{\boldsymbol{\epsilon}}E_0}{2}\left[e^{+i(\boldsymbol{k}_L\cdot\boldsymbol{r}-\omega_L t+\phi)} + e^{-i(\boldsymbol{k}_L\cdot\boldsymbol{r}-\omega_L t+\phi)}\right] \qquad (3.2)$$

where ω_L, $\hat{\boldsymbol{\epsilon}}$, $\boldsymbol{k}_L$ and ϕ are frequency, polarisation vector, wave vector and phase of the laser. The interaction between the light field and the ion is given by the following Hamiltonian:

$$\hat{H}_i = \frac{\hbar\Omega_0}{2}(\hat{\sigma}_+ + \hat{\sigma}_-)\left[e^{+i(k_z z-\omega_L t+\phi)} + e^{-i(k_z z-\omega_L t+\phi)}\right] \qquad (3.3)$$

where we consider only the axial motion, which is along the trap axis, as our spectroscopic laser is directed along the trap axis, so $\boldsymbol{k}_L$ and $\boldsymbol{r}$ are replaced with $\boldsymbol{k}_z$ and $\boldsymbol{z}$, respectively. Ω_0 is the Rabi frequency, which quantifies the coupling strength between the ion and the laser[1]. By quantisation of the ion motion, the position operator $\hat{z}$ and the momentum operator $\hat{p}$ can be written in terms of raising $\hat{a}^\dagger$ and lowering $\hat{a}$:

$$\hat{z} = \sqrt{\frac{\hbar}{2m\omega_z}}\left(\hat{a} + \hat{a}^\dagger\right) = z_0\left(\hat{a} + \hat{a}^\dagger\right)$$
$$\hat{p} = i\sqrt{\frac{\hbar m\omega_z}{2}}\left(\hat{a}^\dagger - \hat{a}\right) = \frac{i\hbar}{2z_0}\left(\hat{a}^\dagger - \hat{a}\right) \qquad (3.4)$$

Also, we define the LD parameter as

$$\eta = k_L z_0 = \sqrt{\frac{\hbar k_z^2}{2m\omega_z}}. \qquad (3.5)$$

The LD parameter is simply given as a product of laser wave vector $\boldsymbol{k}$ and the spatial extent of the ground state wavefunction z_0. The LD parameter quantifies the

---

[1]Approximated expressions for the Rabi frequency vary depending on the type of transitions (i.e. electric dipole and quadrupole transitions). A detailed discussion and calculations of the Rabi frequency Ω_0 for different types of transitions can be found in Appendix A of Ref [60].

confinement of the ion with respect to the laser wavelength, indicating the coupling strength between the atomic internal states and the motional states of the ion. Substituting $\hat{a}$, $\hat{a}^\dagger$ and η into Eqn. (3.1, 3.3) reformulates the laser–ion Hamiltonian as

$$
\begin{aligned}
\hat{H}_0 &= \frac{1}{2}\hbar\omega_{eg}\hat{\sigma}_z + \frac{1}{2}\hbar\omega_z(\hat{a}^\dagger\hat{a}) \\
\hat{H}_{int} &= \frac{1}{2}\hbar\Omega_0(\hat{\sigma}_+ + \hat{\sigma}_-)\left[e^{i\left(\eta(\hat{a}+\hat{a}^\dagger)-\omega_L t+\phi\right)} + e^{-i\left(\eta(\hat{a}+\hat{a}^\dagger)-\omega_L t+\phi\right)}\right]
\end{aligned}
\tag{3.6}
$$

where the zero-point energy of the harmonic oscillator is omitted as it produces only constant offsets to both of the states. When dealing with a time-dependent Hamiltonian, moving into the interaction picture makes it straightforward to solve the Schrödinger equation. In the interaction picture, the Hamiltonian and wavefunction are transformed as follows:

$$
\begin{aligned}
\hat{H}_{int} &= \hat{U}_0^\dagger \hat{H}_i \hat{U}_0 \\
|\Psi(t)\rangle_{int} &= \hat{U}_0^\dagger |\Psi(t)\rangle,
\end{aligned}
\tag{3.7}
$$

and the Schrödinger equation is reformulated as

$$
i\hbar\frac{d}{dt}|\Psi(t)\rangle_{int} = \hat{H}_{int}|\Psi(t)\rangle_{int}.
\tag{3.8}
$$

By transforming to interaction picture with respect to $\hat{U}_0 = e^{-i\hat{H}_0}$, the laser–ion Hamiltonian becomes

$$
\begin{aligned}
\hat{H}_{int} &= \hat{U}_0^\dagger \hat{H}_i \hat{U}_0 \\
&= \frac{\hbar\Omega_0}{2}e^{\frac{i\hat{H}_e t}{\hbar}}(\hat{\sigma}_+ + \hat{\sigma}_+)e^{\frac{-i\hat{H}_e t}{\hbar}}e^{\frac{i\hat{H}_m t}{\hbar}}\left(e^{-i(\omega_L t-\eta_z(\hat{a}+\hat{a}^\dagger)+\phi)}\right)e^{\frac{-i\hat{H}_m t}{\hbar}} \\
&= \frac{\hbar\Omega_0}{2}(\hat{\sigma}_+ e^{+i(\eta_z(\tilde{a}+\tilde{a}^\dagger)-\delta t+\phi)} + \hat{\sigma}_- e^{-i(\eta_z(\tilde{a}+\tilde{a}^\dagger)-\delta t+\phi)})
\end{aligned}
\tag{3.9}
$$

where $\delta = \omega_L - \omega_{eg}$ is a detuning frequency. The last equation is obtained by making the rotating wave approximation that eliminates terms in the Hamiltonian oscillating with frequencies of $\omega_{eg} + \omega_z$, and raising and lowering operators are transformed as

$$
\tilde{a} = e^{-i\omega_z t}\hat{a} \quad \text{and} \quad \tilde{a}^\dagger = e^{+i\omega_z t}\hat{a}^\dagger.
\tag{3.10}
$$

A general quantum state in the interaction picture can be written as

$$|\psi(t)\rangle = \sum_{n=0}^{\infty} c_{g,n}(t) |g, n\rangle + c_{e,n}(t) |e, n\rangle . \tag{3.11}$$

Substituting Eqn. (3.11) into Eqn. (3.8) yields

$$\sum_{n=0}^{\infty} \dot{c}_{g,n} |g, n\rangle + \dot{c}_{e,n} |e, n\rangle = -\frac{i}{2}\Omega_0 \sum_{n}^{\infty} \left(c_{e,n} e^{i\delta t} e^{-i\eta(\tilde{a}+\tilde{a}^{\dagger})} |g, n\rangle + c_{g,n} e^{-i\delta t} e^{+i\eta(\tilde{a}+\tilde{a}^{\dagger})} |e, n\rangle \right) . \tag{3.12}$$

Multiplying by $\langle g, n|$ and $\langle e, n|$ respectively and expanding the exponential in power series of $\tilde{a}$ and $\tilde{a}^{\dagger}$ using the Taylor expansion, we obtain the following coupled equations:

$$\begin{aligned}
\dot{c}_{g,n}(t) &= \frac{-i\Omega_0}{2} e^{i(\delta t - \phi)} \sum_{m=0}^{\infty} c_{e,m} \langle n| \sum_{k=0}^{\infty} \frac{(-i\eta)^k}{k!} (\hat{a}_z^{\dagger} e^{-i\omega_z t} + \hat{a}_z e^{i\omega_z t})^k |m\rangle \\
\dot{c}_{e,n}(t) &= \frac{-i\Omega_0}{2} e^{i(\delta t - \phi)} \sum_{m=0}^{\infty} c_{g,m} \langle n| \sum_{k=0}^{\infty} \frac{(i\eta)^k}{k!} (\hat{a}_z^{\dagger} e^{i\omega_z t} + \hat{a}_z e^{-i\omega_z t})^k |m\rangle
\end{aligned} \tag{3.13}$$

Eqn. (3.10) indicates the $\hat{a}$ and $\hat{a}^{\dagger}$ operators carry a time-dependent exponential $e^{-i\omega_z t}$ and $e^{+i\omega_z t}$, respectively. Therefore, a term with p raising and q lowering operators in the expansion in Eqn. (3.13) is associated with the total frequency term of $e^{i(\delta - m\omega_z)t}$ where $m = p - q$. In addition, this term raises or lowers the motional state $|n\rangle$ to $|n + m\rangle$; the orthogonality of the motional states guarantees this term preserves only m in the summation. If the laser has a linewidth $\Delta_{\omega_L} \ll \omega_z$, its associated Rabi frequency $\Omega_0 \ll \omega_z$, and its frequency is set such that $\delta - m\omega_z$ is close to zero (i.e. the laser is tuned close to the resonance of the mth-order sideband transition), then only the term associated with the mth-order sideband dominates the sum, ignoring the terms with the other sidebands, which is analogous to the rotating wave approximation. Thus, Eqn. (3.13) can be simplified to

$$\begin{aligned}
\dot{c}_{g,n}(t) &= -i\frac{\Omega_{n,n+m}}{2} e^{i(\Delta t - \phi)} c_{e,n+m} \\
\dot{c}_{e,n+m}(t) &= -i\frac{\Omega_{n,n+m}}{2} e^{-i(\Delta t - \phi)} c_{g,n}
\end{aligned} \tag{3.14}$$

where $\Delta = \delta - m\omega_z$ is the detuning with respect to the mth-order sideband. $\Omega_{n,n+m}$ is given as [61, 62]

21
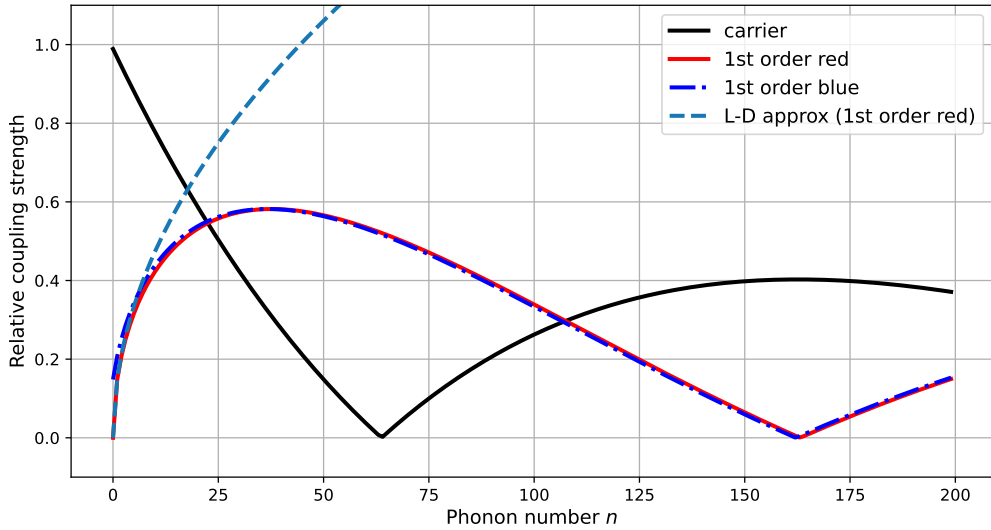
Figure 3.1: Relative strength of the carrier and first-order sideband as a function of a phonon number n with $\eta = 0.9$, which is the typical value of η in our experiment. The dotted line represents the strength of the first-order blue sideband with the LD approximation applied. Contrary to the LD regime, the coupling strength does not increase monotonically with n, and the coupling strength becomes null at $n \approx 65$. This point leads to motional trapping when we perform sideband cooling outside the LD regime because the motional state at that trapping point no longer interacts with the ion and stays as it is. [63, 64, 65].

$$
\begin{aligned}
\Omega_{n,n+m} &= \Omega_0 \langle n| e^{i\eta_z(\hat{a}+\hat{a}^\dagger)} |n+m\rangle \\
&= \Omega_0 e^{-\frac{\eta_z^2}{2}} (i\eta_z)^{|m|} L_k^{|m|}(\eta_z^2) \left[\frac{n!}{(n+m)!} \right]^{\frac{\mathrm{sgn}(m)}{2}}
\end{aligned}
\tag{3.15}
$$

where $k = \mathrm{Min}(n, n+m)$, and the generalised Laguerre polynomial is defined by

$$
L_k^{|m|}(\eta^2) = \sum_{l=0}^{k} (-1)^l \binom{k+|m|}{k-l} \frac{\eta^{2l}}{l!}.
\tag{3.16}
$$

Fig. 3.1 shows the relative coupling strength as a function of phonon number n. It is important to note that the coupling strength for all orders, including the carrier, becomes zero at some phonon numbers but at different n.

If the ion is initially in the internal ground state with motional quantum number n $|g,n\rangle$ (at $t=0$), then the solution of Eqn. (3.14) is given by

$$
P_e(t) = \frac{\Omega_{n,n+m}^2}{\Omega_{n,n+m}^2 + \Delta^2} \sin^2 \left(\frac{\sqrt{\Omega_{n,n+m}^2 + \Delta^2}}{2} t \right).
\tag{3.17}
$$

This is a generalised Rabi oscillation, which is periodic population transfer between

$|g, n\rangle$ and $|e, n + m\rangle$. If we drive the transition on resonance $\Delta = 0$, the interaction completely inverts the initially prepared $|g, n\rangle$ state to the $|e, n + m\rangle$ state, and we define π time at which the complete population inversion occurs.

We now consider a special case where the confinement of the ion, which is quantified by the wave function spread with an average phonon number $\bar{n}$, which is $z_0\sqrt{2\bar{n} + 1}$, is much smaller than the wavelength of the laser:

$$\eta_z\sqrt{2\bar{n} + 1} \ll 1. \tag{3.18}$$

Under this condition, the ion is said to be in the LD regime. In the LD regime, the ion is significantly coupled to the laser via the carrier and the first-order red and blue sideband transition, while the higher-order transitions are strongly suppressed. Also, the coupling strength specified in Eqn. (3.15) can be approximated by expanding the exponential to the second order:

$$
\begin{aligned}
\Omega_{n,n+l} &= \langle n| e^{i\eta_z(\hat{a} + \hat{a}^\dagger)} |n + l\rangle \\
&= \langle n| 1 + i\eta_z(\hat{a} + \hat{a}^\dagger) - \frac{1}{2}\eta_z^2(\hat{a} + \hat{a}^\dagger)^2 |n + l\rangle .
\end{aligned}
\tag{3.19}
$$

Then, the approximate Rabi frequencies for the carrier and the first-order red and blue sdiebands are given by

$$
\begin{aligned}
\Omega_{n,n-1} &= \Omega_0\eta_z\sqrt{n} \\
\Omega_{n,n} &= \Omega_0\left(1 - \frac{1}{2}\eta_z^2(2n + 1)\right) \\
\Omega_{n,n} &= \Omega_0\eta_z\sqrt{n + 1}.
\end{aligned}
\tag{3.20}
$$

3.2   Raman Interaction

We can also use the two Zeeman sublevels of $S_{1/2}$ as a qubit. These states nearly do not decay from one state to another, leading to substantially long energy relaxation time T_1. Thus, $S_{1/2}$ manifolds can form a stable qubit. There are two straightforward ways to couple these states – the first is that we can directly couple these two states using a microwave field whose frequency matches the energy difference between the states, and the other is that we can indirectly couple them using two-photon Raman interaction. The first method has a significant downside in that this interaction results in relatively weak coupling between the internal and the motional states due to a small LD parameter η because the microwave field has a relatively long wavelength compared to typical optical lasers used in ion trap experiment, and this long wavelength corresponds to a small LD parameter, making extremely weak
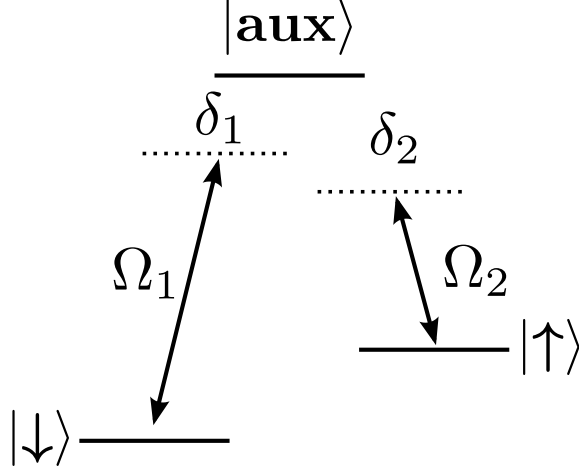
Figure 3.2: A level diagram for a three-level system that demonstrates a Raman interaction. We make an indirect coupling between $|\uparrow\rangle$ and $|\downarrow\rangle$ by off-resonantly driving the transitions $|\downarrow\rangle \leftrightarrow |\text{aux}\rangle$ with Rabi frequency Ω_1, detuning δ_1 and $|\uparrow\rangle \leftrightarrow |\text{aux}\rangle$ with Rabi frequency Ω_2 and detuning δ_2.

coupling between atomic internal and motional states. Thus, we exploit two-photon Raman interaction in a realisation of a Zeeman qubit in our experiments.

3.2.1 Raman Coupling

We first consider a three-level system that consists of $|\downarrow\rangle$, $|\uparrow\rangle$ and $|\text{aux}\rangle$. As illustrated in Fig. 3.2, we off-resonantly drive the transitions $|\downarrow\rangle \leftrightarrow |\text{aux}\rangle$ and $|\uparrow\rangle \leftrightarrow |\text{aux}\rangle$ with Rabi frequencies, detunings, phases and wave vectors Ω_1, Δ_1, ϕ_1, $\boldsymbol{k_1}$ and Ω_2, Δ_2, ϕ_2, $\boldsymbol{k_2}$. In the interaction picture, the Hamiltonian that describes the dynamics driven by those interactions can be written as

$$H = \frac{\hbar}{2}\Omega_1 e^{i(\boldsymbol{k_1}\cdot\boldsymbol{r}-\Delta_1 t+\phi_1)}|\text{aux}\rangle\langle\downarrow| + \frac{\hbar}{2}\Omega_2 e^{i(\boldsymbol{k_2}\cdot\boldsymbol{r}-\Delta_2 t+\phi_2)}|\text{aux}\rangle\langle\uparrow| + \text{h.c.} \qquad (3.21)$$

If the detuning of each laser is set to be far off-resonant, we can ignore a direct population transfer between $|\text{aux}\rangle$ and the two ground states, $|\downarrow\rangle$ and $|\uparrow\rangle$. In addition, if $|\delta_1 - \delta_2| \ll \delta_1, \delta2$, we can simplify the Hamiltonian in Eqn. (3.21) to the following effective Hamiltonian by applying the James–Jerk approximation [66]:

$$\begin{aligned} H = \frac{\hbar\Omega_1^2}{4\delta_1}\left(|\downarrow\rangle\langle\downarrow| - |\text{aux}\rangle\langle\text{aux}|\right) + \frac{\hbar\Omega_2^2}{4\delta_2}\left(|\uparrow\rangle\langle\uparrow| - |\text{aux}\rangle\langle\text{aux}|\right) \\ + \frac{\hbar\Omega_1\Omega_2}{4\Delta}\left(e^{i\Delta\boldsymbol{k}\cdot\boldsymbol{r}-i\delta t+i\phi}|\uparrow\rangle\langle\downarrow| + \text{h.c.}\right) \end{aligned} \qquad (3.22)$$

where $\phi := \phi_1 - \phi_2$, $\Delta\boldsymbol{k} := \boldsymbol{k_1} - \boldsymbol{k_2}$, $1/\Delta := \frac{1}{2}\left(\frac{1}{\delta_1} + \frac{1}{\delta_2}\right)$ and $\delta := \delta_1 - \delta_2$. The first two terms in Eqn. (3.21) correspond to the AC Stark shift, and the last term

indicates an effective coupling between $|\downarrow\rangle$ and $|\uparrow\rangle$. This effective coupling term is in a similar form to the standard light–matter interaction described by Eqn. (3.3), with $\boldsymbol{k} \to \Delta\boldsymbol{k}$, $\phi \to \phi_1 - \phi_2$, and $\delta \to \delta_1 - \delta_2$; with an appropriate choice of δ, the Raman interaction can be applied to address the carrier ($\delta = 0$) and the first-order sideband transitions ($\delta = \pm\omega_z$).

3.2.2 Photon Scattering

In the typical implementation of Raman interaction, the detunings, δ_1 and δ_2, are set to be sufficiently large to ensure the upper level $|\text{aux}\rangle$ is barely populated. However, the ion can be excited to the $|\text{aux}\rangle$ state with finite detunings, although it is very unlikely with large detunings. The ion in the $|\text{aux}\rangle$ state spontaneously decays to either $|\downarrow\rangle$ or $|\uparrow\rangle$. According to the Kramers–Heisenburg formula, the scattering rate from $|i\rangle$ to $|f\rangle$ is given by [67, 68]

$$\Gamma_{i,f} = \gamma \sum_j \left| \frac{\Omega_{i,e_j} \Lambda_{e_j,f}}{\delta_{e_j}} \right|^2 \tag{3.23}$$

where the sum runs over all auxiliary states $|\text{aux}\rangle_j$, γ is the Einstein A coefficient for $P_{1/2}$ manifold, Ω_{i,e_j} is the Rabi frequency of the driving field on the transition $|i\rangle \leftrightarrow |e_j\rangle$ and $\Lambda_{e_j,f}$ is the respective 3-j symbol. There are two distinct routes – the first is Raman scattering, where the final state is different from the initial state, and the other is Rayleigh scattering, where the excited ion decays back to the initial state. Both scattering processes accompany a momentum kick resulting from photon emission and consequently result in motional decoherence. Raman scattering decoheres the internal state of the atom because the Raman scattering alters the ion's internal state; thus, the internal state is entangled with the scattered photon while the Rayleigh scattering does not always result in decoherence – the Rayleigh scattering barely induces decoherence if the scattering rates from both qubit states are approximately equal [69], but if the scattering rates are quite different, then the rate of decoherence due to the Rayleigh scattering is proportional to the difference in the scattering probabilities [70].

3.3 Raman Interaction in $^{40}\text{Ca}^+$

Fig. 3.3 presents a simplified energy level structure of $^{40}\text{Ca}^+$ with the atomic transitions relevant to implementation of the Raman coupling. Unlike the theoretical model described in Sec 3.2.1, our system consists of four levels, including two auxiliary levels ($P_{1/2,\pm1/2}$) instead of one. An applied external magnetic field $B \approx 0.32\,\text{mT}$ produces Zeeman splitting between $P_{1/2,\pm1/2}$ states of $\approx 3.04\,\text{MHz}$, which
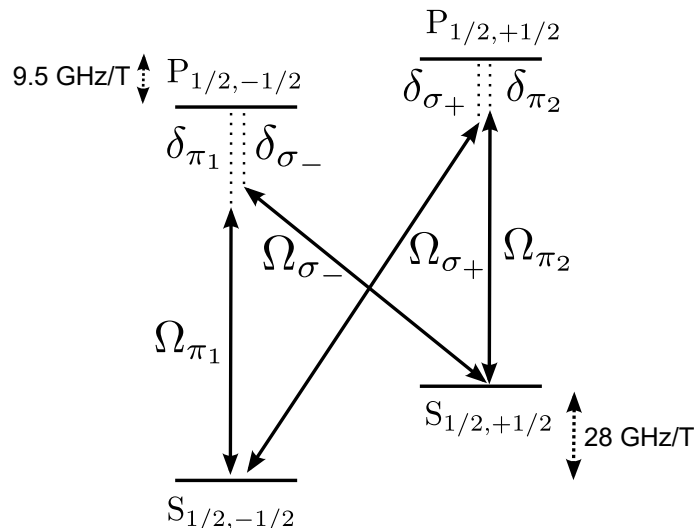
Figure 3.3: Simplified energy level diagram of ^{40}Ca$^+$ with the transitions involved in realisation of the Raman coupling between the $S_{1/2,-1/2}$ and $S_{1/2,1/2}$ states. Zeeman splittings for the $S_{1/2}$ and $P_{1/2}$ levels are shown. A pair of Raman beams shown in Fig. 3.4 (*perpendicular* and *parallel* beams) drives π and $\sigma_\pm$ transitions between the $S_{1/2}$ and $P_{1/2}$ manifolds.

is comparable to the linewidth of the driving lasers. Hence, we cannot couple each S state exclusively to one of the P states, and we drive four different transitions simultaneously, including two π and $\sigma_\pm$ transitions. As illustrated in Fig. 3.4, two 397 nm beams are used as Raman beams – one of the beams is directed along the quantisation axis, which is labelled *parallel* beam, while the other propagates perpendicular to the quantisation axis, which is called *perpendicular* beam. The *parallel* and *perpendicular* Raman beams drive two π and $\sigma_\pm$ transitions respectively. Each pair of π and σ transitions induces the Raman coupling between $S_{1/2,-1/2}$ and $S_{1/2,1/2}$ but via different routes.

P$_{1/2}$ states can also decay to D$_{3/2}$, which is not included in the energy level diagram, and we have to empty the population of D$_{3/2}$ to avoid population trapping in this state. So, we exploit a laser at 866 nm, which drives a dipole transition D$_{3/2} \leftrightarrow$ P$_{1/2}$, as a re-pumper. The branching ratio to D$_{3/2}$ is relatively small, and thus we ignore this in the rest of the discussion.

3.3.1 Rabi Frequencies and AC Stark Shifts

Although our system includes two auxiliary states, unlike the theory presented in Sec 3.2.1, the effective Rabi frequency of the coupling between the Zeeman sublevels is simply given as the sum of each path as long as the condition that detunings are far off-resonant is satisfied:

$$\Omega_{12} = \frac{\Omega_{\pi_1}\Omega_{\sigma_-}}{2\Delta_1} + \frac{\Omega_{\pi_2}\Omega_{\sigma_+}}{2\Delta_2} \tag{3.24}$$
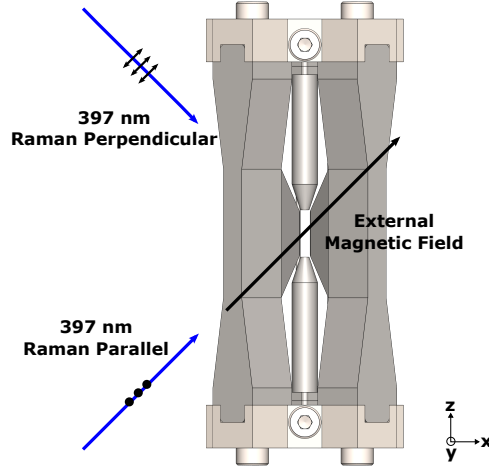
Figure 3.4: Orientation and polarisation of the Raman beams with respect to the trap electrodes and an applied magnetic field, which define quantisation axis. Two linearly polarised 397 nm laser beams are used. One beam propagates perpendicular to the applied magnetic field (*perpendicular* Raman beam), while the other is directed along the magnetic field (*parallel* Raman beam).

where Ω_i is the Rabi frequency of each transition, and Δ_i is the mean detuning of the beams with respect to the corresponding $|\text{aux}\rangle_i$ state (defined in Eqn. 3.22).

The AC Stark shift due to the off-resonant coupling of each beam is given as

$$
\begin{aligned}
\Delta_{\text{ac},\downarrow} &= \frac{\Omega_{\pi_2}^2}{4\delta_{\pi_2}} + \frac{\Omega_{\sigma_-}^2}{4\delta_{\sigma_-}} \\
\Delta_{\text{ac},\uparrow} &= \frac{\Omega_{\pi_1}^2}{4\delta_{\pi_1}} + \frac{\Omega_{\sigma_+}^2}{4\delta_{\sigma_+}}
\end{aligned}
\tag{3.25}
$$

where δ_i is detuning of each beam.

3.3.2 Ratio of Scattering Rate to AC Stark Shift

To characterise our Raman qubit, we wish to measure the scattering rate, which quantifies the decoherence of the qubit due to photon scattering. The scattering rate varies depending on the power of the beam, but as we take a ratio of the scattering rate Γ to the AC Stark shift Δ_{SS}, we can obtain the power-independent quantity:

$$
\frac{\Gamma}{\Delta_{SS}} = \frac{5}{12}\gamma \left| \frac{\omega_0}{\Delta(\delta - \omega_0)} \right|
\tag{3.26}
$$

where Δ is detuning from the resonance of $S_{1/2} \leftrightarrow P_{1/2}$ transition, and ω_0 is the Zeeman splitting of $S_{1/2}$.

In our experiment, we initially prepare the ion in the $S_{1/2,1/2}$ state. We then turn
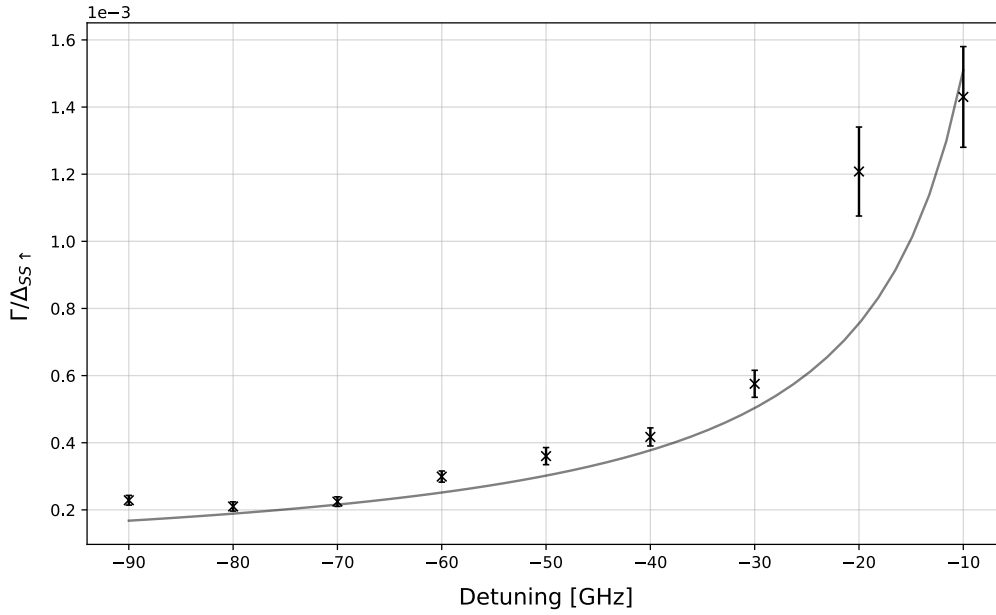
Figure 3.5: Ratio of Raman scattering ratio to the AC Stark shift to $|\downarrow\rangle$. The solid line indicates the theoretical prediction. The measurements well agree with the theory, except for one point at $\delta = -20\mathrm{GHz}$.

on one of the Raman beams and measure the population of the $\mathrm{S}_{1/2,1/2}$ state. The population of $\mathrm{S}_{1/2,1/2}$ is initially unity but exponentially decays and converges to the half as the Raman beam excites the ion to the $\mathrm{P}_{1/2}$ state, and the ion decays to either sub-level of $\mathrm{S}_{1/2,1/2}$ with equal probability:

$$P_{\mathrm{S}_{1/2,1/2}}(t) = \frac{1}{2}(1 + e^{-\Gamma t}) \tag{3.27}$$

3.3.3 Differential AC Stark Shift

All transitions involved in Raman interaction are driven off-resonantly, so these off-resonant interactions produce an AC Stark shift to the two lower-level states, $|\downarrow\rangle$ and $|\uparrow\rangle$. If the shift to each level is in the same direction with the same amount, the energy difference between $|\downarrow\rangle$ and $|\uparrow\rangle$ stays the same; otherwise, the energy difference can be shifted, and the net change $\Delta_{\downarrow,\uparrow}$ can be obtained by rearranging Eqn. 3.25:

$$\Delta_{\downarrow,\uparrow} = \Delta_{SS,\uparrow} - \Delta_{SS,\downarrow}$$
$$= \underbrace{\left[\frac{\Omega_{\pi_2}^2}{4\delta_{\pi_2}} + \frac{\Omega_{\sigma_-}^2}{4\delta_{\sigma_-}}\right]}_{\Delta_{SS,\uparrow}} - \underbrace{\left[\frac{\Omega_{\pi_1}^2}{4\delta_{\pi_1}} - \frac{\Omega_{\sigma_+}^2}{4\delta_{\sigma_+}}\right]}_{\Delta_{SS,\downarrow}} \tag{3.28}$$

A pair of π transitions are addressed by a single laser, which is labelled as the *parallel* beam, leading to the same amount of Ω_{π_1} and Ω_{π_2} and no net change in energy

difference between the two lower states. However, the two $\sigma_\pm$ are driven by orthogonal components of a laser (left and right circularly polarised components). Thus, the Rabi frequency of each transition can be different, although those transitions are also addressed by the single laser, which is referred to *parallel* beam, if the laser contains different powers of σ_- and σ_+ beams. As shown in Fig. 3.4, this laser is directed along the quantisation axis, and the beam is linearly polarised. Hence, in principle, the beam contains an equal amount of left and right circularly polarised components, resulting in no differential AC Stark shift. However, if the beam contains any ellipticity, then the Rabi frequency of each σ transition is different, causing a differential AC Stark shift and a net change in $\Delta_{\downarrow,\uparrow}$. This differential AC Stark shift is power dependent; this power-dependent differential shift requires us to calibrate the qubit resonance frequency every time we use a different power of the beam and, more importantly, convert the power fluctuation of the beam to the fluctuation of the phase accumulated on the qubit, leading to the faster decoherence of the qubit. Therefore, we need to measure the ellipticity of the laser and ensure the differential shift is zero.

In our experiment, the differential AC Stark shift is measured using a Ramsey-type scan where we apply two $\pi/2$ pulses separated by a fixed wait time T, and only the *parallel* Raman beam, which induces $\sigma_\pm$ transitions, is switched on for a variable amount of time $\tau < T/2$. The spin-echo pulse, which is a π pulse of Raman interaction, is applied at $T/2$ to eliminate phase accumulated due to constant detuning with respect to the Raman qubit frequency. We also measure the AC Stark shift due to only the σ_- polarised beam using the Ramsey scan, but here we apply the π and $\pi/2$ pulses of the $S_{1/2,1/2} \leftrightarrow D_{5/2,1/2}$ transition at $729\,\text{nm}$ in this Ramsey experiment to infer only the frequency shift to $S_{1/2,1/2}$. To measure the ellipticity of the beam, we need to know the ratio between $\Omega_{\sigma_+}^2$ and $\Omega_{\sigma_-}^2$. This ratio can be calculated through the differential AC Stark shift $\Delta_{\downarrow,\uparrow}$ and $\Delta_{SS,\downarrow}$:

$$\frac{\Omega_{\sigma_+}^2}{\Omega_{\sigma_+}^2} = 1 - R \qquad (3.29)$$

where $R := \Delta_{\downarrow,\uparrow}/\Delta_{SS,\uparrow}$, and we assume $\delta_{\sigma_+} \simeq \delta_{\sigma_-}$.

Fig. 3.6 clearly suggests that the differential AC Stark shift varies with the angle of the waveplate that changes the angle of linearly polarised *parallel* beam – this indicates that the amount of ellipticity of the beam changes as we change the waveplate angle. The birefringence of the vacuum window can account for this observation. The windows introduce retardance of the two components that are parallel and orthogonal to the principal axis of the window, leading to ellipticity in the linearly polarised beam. The amount of the ellipticity varies depending on the relative polarisation angle of the beam with respect to the principal axis of the
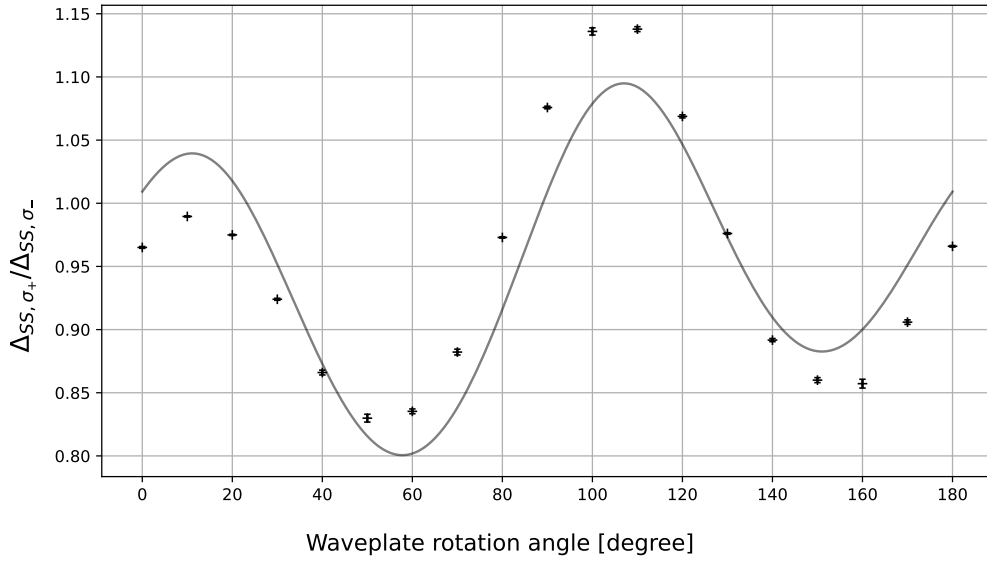
Figure 3.6: Ratio between the AC Stark shifts to two lower states $|\downarrow\rangle$ and $|\uparrow\rangle$ as a function of waveplate angle. The solid line represents a fit curve modelled by the birefringence of the vacuum window, which introduces ellipticity into the beam.

window. Fig. 3.6 includes a fitting curve that is modelled by the birefringence of the window. The fitting curve follows the experimental results in their overall shape, but each data point is relatively inconsistent with the fitting curve. This might suggest that other sources add ellipticity to the Raman beam, but unfortunately, they are unknown. Fig. 3.6 indicates there are several waveplate angles such that the differential AC Stark shift becomes null; we set the waveplate to one of those angles to minimise the power-dependent AC Stark shift. However, those angles that lead to zero differential shift might be different if the environment around the trap changes. So, we must routinely perform the scan to ensure the waveplate angle is appropriately set.

Chapter 4

Laser Cooling

When an ion is loaded into the trap, its initial velocity distribution roughly follows the Maxwell–Boltzmann distribution at room temperature, where the classical effect dominates over quantum behaviour. In addition, the ion cannot be localised. Therefore, most ion trap experiments start with the preparation of the ion in its motional ground state, and the ground state cooling is achieved by laser cooling techniques in our experiment. Laser cooling is the most commonly used cooling technique in atomic physics experiments. This was firstly proposed for trapped ions by Dehemlt and Wineland in the late 1900s [71], and experimentally demonstrated shortly afterwards [61]. In our experiments, the ground state cooling is achieved via two cooling steps – the ion is first cooled to Doppler temperature, in which a significant fraction of the motional population still lies outside the motional ground state, using Doppler cooling. Subsequently, resolved sideband cooling is applied to achieve a sub-Doppler temperature and ultimately prepare the ion in its motional ground state, which is a pure state and a critical requirement for coherent logic operations with high fidelity. In this chapter, the general description of Doppler cooling and resolved sideband cooling will be discussed, as will the frequency spectra and Rabi oscillations with a single ion properly cooled through the two cooling methods. The spectra enable us to estimate the average photon number $\bar{n}$ of the ion, which is related to the temperature of the ion.

4.1   Doppler Cooling

When an ion is illuminated by a resonant laser, the ion absorbs a photon from the laser and experiences a net change in its momentum by the momentum of the photon $\hbar k_L$ in the direction of the beam:

$$\boldsymbol{P}' = \boldsymbol{P} + \hbar\boldsymbol{k}_L \tag{4.1}$$
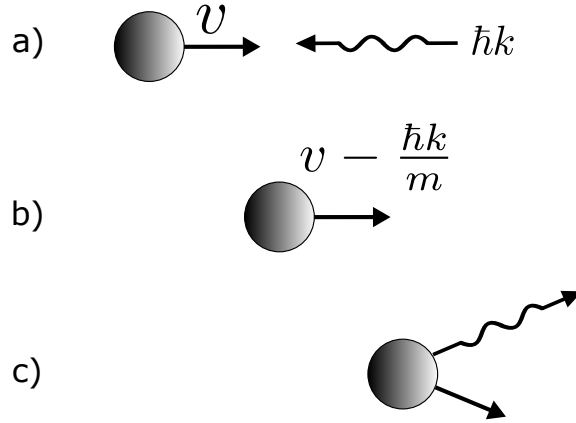
Figure 4.1: Doppler cooling process. a) a particle moves to the right at velocity v while
a photon moves toward the particle with momentum $\hbar k$. b) The particle
absorbs the photon and loses its momentum by $\hbar k/m$, which is the amount of
momentum the photon carries . c) The particle emits the photon in a random
direction via spontaneous emission, leading to no net change in its momentum
on average. The particle repeatably goes through the processes a), b), and c),
and its average change in momentum is attributed to momentum change due
to the absorption, which corresponds to the reduction of its kinetic energy.
The diagram is adapted from William[72].

The ion that absorbs the photon becomes excited. Once the ion is excited, the
excited ion decays back to the initial ground state via spontaneous decay, and the
absorption and emission occur repeatedly. This transition is referred to a *cyclic*
transition, and $S_{1/2} \leftrightarrow P_{1/2}$ in $^{40}Ca^+$, which is *cyclic*, is used for the Doppler cooling
in our experiment.

Doppler cooling is performed in a weak-binding limit where the linewidth of the
involved transition is much greater than the harmonic frequencies of the trap. Many
absorptions and emissions occur while the ion completes one cycle of periodic motion.
In this limit, the ion can be considered as a free particle, the momentum change due
to photon scattering can be considered to be instantaneous, and the dynamics of ions
under the influence of the interacting laser can be described semi-classically [73] –
the dynamics of the internal state are described by quantum mechanics, whereas the
dynamics of the motional state follow classical mechanics as we formulate a radiative
force, which is a classical force, due to photon scattering in the following form:

$$\boldsymbol{F} = \frac{\text{momentum transfer}}{\text{time}} = \hbar\boldsymbol{k}R \tag{4.2}$$

where R is the scattering rate. Assuming the internal state of the ion is in the steady
state, the scattering rate is derived from the steady-state solution of Einstein's rate
equations [60]:

$$R = \Gamma \rho_{ee} = \frac{\Gamma \Omega^2}{\Gamma^2 + \Omega^2 + 4(\delta - \boldsymbol{k} \cdot \boldsymbol{v})^2}$$
$$= \frac{\Gamma \Omega^2}{\Gamma_B^2 + 4(\delta - \vec{k} \cdot \vec{v})^2} \tag{4.3}$$

where $\Gamma_B = \Gamma^2 + \Omega^2$ is a power-broadened linewidth, and the $\boldsymbol{k} \cdot \boldsymbol{v}$ term indicates the frequency shift seen by the moving ion due to the Doppler effect. The Doppler effect makes the radiative force velocity dependent. In the low-velocity limit, Eqn. 4.3 can be approximated to the first order of $\boldsymbol{v}$ by the Taylor expansion around $\boldsymbol{v} = 0$:

$$R \approx \frac{\Gamma \Omega^2}{\Gamma^2 + 4\delta} + \frac{8k\delta\Gamma\Omega^2}{(\Gamma^2 + 4\delta^2)^2} v_z \tag{4.4}$$

where, for simplicity, $\boldsymbol{k} \cdot \boldsymbol{v}$ is replaced with v_z assuming the Doppler beam propagates along the $\hat{z}$ direction. The linearisation around $v_z = 0$ makes the radiative force be in the form of $F = F_0 + \beta v_z$ – the radiative force consists of constant light pressure[1] and a force linearly dependent on the ion's velocity. As the Doppler laser is red-detuned, which means δ is negative, the shifted frequency becomes closer to the resonance for the ion counter-propagating with the laser – the ion scatters more photons when the ion is moving toward the laser than when the ion is moving away from it and makes the coefficient of the v term β negative. The velocity-dependent force acts as a drag force that gradually decelerates the ion. We can obtain the cooling rate as an average rate of energy change in a unit of time:

$$\left(\frac{dE}{dt}\right)_{cool} = \langle F v_z \rangle = \frac{\Gamma \Omega^2}{\Gamma^2 + 4\delta} \langle v_z \rangle + \frac{8k\delta\Gamma\Omega^2}{(\Gamma^2 + 4\delta^2)^2} \langle v_z^2 \rangle$$
$$= -\frac{8\hbar k^2 \Gamma \delta \Omega^2}{(\Gamma_B^2 + 4\delta^2)^2} \left(\frac{k_B T}{m}\right) \tag{4.5}$$

The excited ion decays to the atomic ground state via spontaneous emission, emitting the photon in a random direction. The randomness of the emitted photon makes the average momentum change due to spontaneous emission $\langle \Delta P \rangle = 0$, but the discrete nature of the process causes Brownian-like motion, leading to diffusion in the momentum space. The diffusion results in heating, and the heating rate is given as

---

[1]The constant light pressure displaces the equilibrium position of the ion, and the ion is moved back to the original position when the Doppler beam is switched off. This leads to relaxation heating. The detailed analysis of this heating mechanism can be found in Ref. [60].

$$\left(\frac{dE}{dt}\right)_{heat} = \frac{1}{2m}\frac{d}{dt}\langle p^2 \rangle = \frac{(\hbar k)^2}{2m}\Gamma\rho_{ee} = \frac{(\hbar k)^2\Gamma\Omega^2}{2m(\Gamma_B^2 + 4\delta^2)} \qquad (4.6)$$

The ion reaches an equilibrium where the cooling and heating rate become balanced, and the Doppler temperature is given as

$$T_D = \frac{\hbar(\Gamma_B^2 + 4\delta^2)}{8\delta k_B}. \qquad (4.7)$$

The Doppler temperature T_D can be minimised by choosing $\delta = \Gamma_B/2$ and if the intensity of the Doppler beam is set to be well below the saturation intensity, so that $\Gamma_B \approx \Gamma$. Thus, the Doppler limit can be reduced to

$$T_{D,min} = \frac{\hbar\Gamma_B}{2k_B} \approx \frac{\hbar\Gamma}{2k_B} \qquad (4.8)$$

4.2 Resolved Sideband Cooling
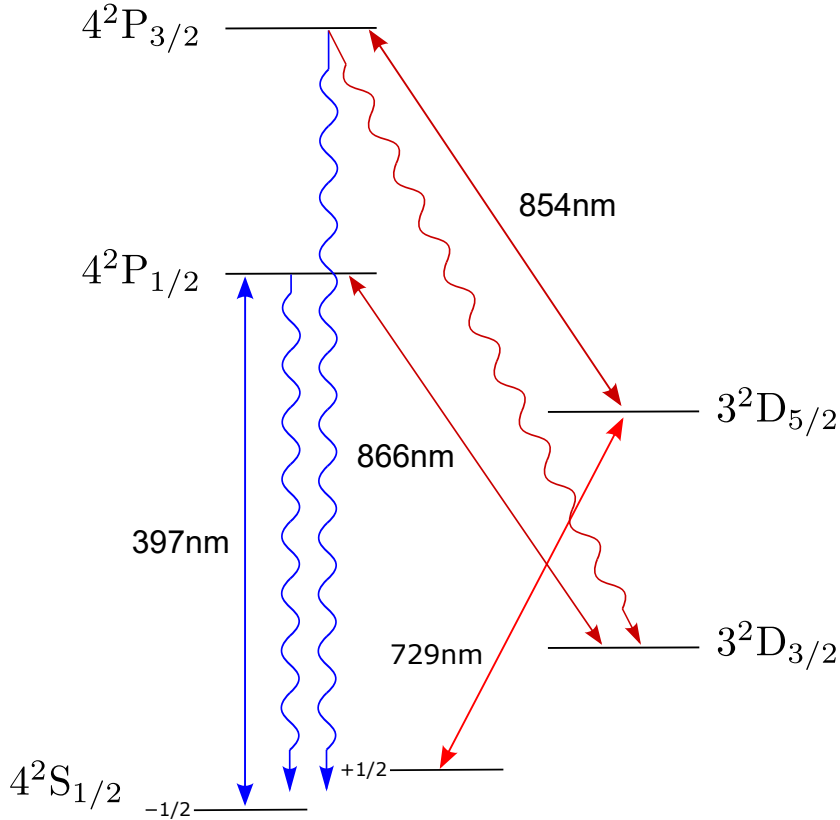
Figure 4.2: Simplified energy level diagram of ^{40}Ca$^+$ that indicates all lasers used in resolved sideband cooling. The 854 and 866 nm lasers are used to empty $D_{5/2}$ and $D_{3/2}$ respectively. The 397 nm laser drives σ_- transition to prepare the ion in $S_{1/2,1/2}$, which can be driven by the 729 nm laser, reducing ion's motional quanta

Even when the temperature of the ion reaches thermal equilibrium at the Doppler

limit, a significant fraction of the motional population still lies outside the motional ground state. Those populations outside the motional ground state result in rapid dephasing of different motional states as the coupling strengths of transitions vary depending on the associated phonon number n and consequently hinder coherent logic operations on the ion. That is why a subsequent cooling step is required. In our experiments, resolved sideband cooling (SBC), which is the widely used sub-Doppler cooling technique, is adopted to cool the ion to its motional ground state. Resolved SBC is performed in the strong-binding limit where the linewidth of the transition is much smaller than the harmonic frequency of the ion, so each sideband transition can be resolved, and we can selectively drive each sideband transition.

Fortunately, with typical trap frequencies used in our experiment, the Doppler temperature is cold enough to bring the ion into the LD regime, where the excited ion spontaneously decays to the internal ground state predominately on the carrier transition. Bringing the ion into the LD regime is a crucial prerequisite for resolved SBC because spontaneous decay on the sideband leads to motional heating and increases the final temperature of the ion. Fig. 4.2 summarises all lasers used in resolved sideband cooling. There are two distinct ways to implement resolved SBC in the experiments – pulsed and continuous SBC. We examined both schemes and found that both allow for cooling the ion to about the same temperature. However, the pulsed SBC takes a somewhat shorter time and is much less complicated. A more detailed description of the methods will be given below.

4.2.1 Pulsed Sideband Cooling
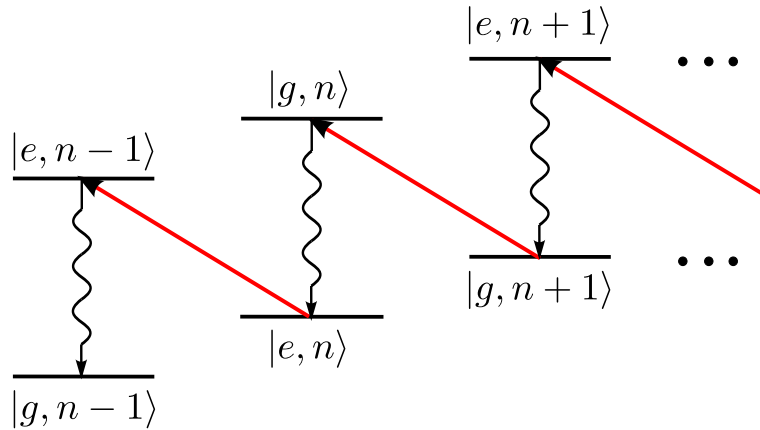
Figure 4.3: Principles of the resolved SBC. The ion is driven on the red sideband, exciting an ion from $|g\rangle$ to $|e\rangle$ while its associated motional quantum number is reduced from n to $n-1$. The curly arrow represents a spontaneous emission, and the decay occurs predominately on the carrier transition, leaving the motional quantum number n unchanged. The iterative absorption and emission cool the ion to the motional ground state.

As the name 'pulsed' may suggest, this protocol involves a series of pulses that include the first-order red sideband, re-pumping and state preparation pulses. A cooling sequence can be summarised as follows:

1. first-order red sideband pulse

2. re-pumping laser at $854\,\mathrm{nm}$ to empty $D_{5/2}$ state

3. state preparation to $S_{1/2,1/2}$ using σ_+ polarised beam

4. repeat steps (1) to (3)

Each cycle starts with an application of the first-order red sideband pulse that induces population transfer from $\left|S_{1/2,m_j=1/2},n\right\rangle$ to $\left|D_{5/2,m_j=1/2},n-1\right\rangle$ for $n\neq0$, which is indicated by the red arrow in Fig. 4.3, reducing the phonon number n by one unit of motional quanta. We must bring the population of $D_{5/2,1/2}$ state back to $S_{1/2,1/2}$ to be able to repeatedly drive the red sideband transition. However, the lifetime of the $D_{5/2}$ state is approximately $1.2\,\mathrm{s}$, so this long lifetime prolongs the whole cooling process.
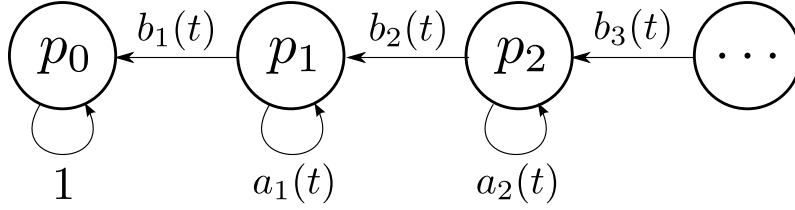
Figure 4.4: Diagram of flow of motional population during a single cycle of the cooling sequence. a_n indicates the portion of population that stays in the same motional state $|n\rangle$ (*non-cooling*), and b_n represents the population whose motional quanta is reduced by one unit (*cooling*). The diagram is adapted from Rasmusson et al.[74].

To accelerate the process, we use a re-pumping laser at $854\,\mathrm{nm}$ that empties the population of $D_{5/2}$ by driving a dipole transition $D_{5/2}\leftrightarrow P_{3/2}$ – the population of $D_{5/2}$ is optically pumped to the $S_{1/2}$ state via the $P_{3/2}$ state. However, the $P_{3/2}$ state can decay to either sublevel of $S_{1/2}$, but the $S_{1/2,-1/2}$ state is undesirable because this state is not addressed by the red sideband pulse that is precisely tuned close to the resonance of $S_{1/2,1/2}\leftrightarrow D_{5/2,1/2}$. Hence, we apply a σ_+-polarised $397\,\mathrm{nm}$ beam to transfer the population of $S_{1/2,-1/2}$ to the desired $S_{1/2,1/2}$ state. Assuming the ion is in the LD regime, the deshelving of the $D_{5/2,1/2}$ state, which involves $854\,\mathrm{nm}$ re-pumping and $397\,\mathrm{nm}$ state-preparation pulses, occurs predominantly on the carrier transition: we can assume that the associated motional quantum number is unchanged during the re-pumping process and effectively brings $\left|D_{5/2,1/2},n-1\right\rangle$ to $\left|S_{1/2,1/2},n-1\right\rangle$, leading to the cooling of the ion. Each cooling sequence aims to reduce the average phonon number $\bar{n}$ by at most one unit of motional quanta.

Fig. 4.4 illustrates the flow of the motional population during one SBC cycle. Using Eqn. 3.17, the cooling probability $a_n(t)$ and non-cooling probability $b_n(t)$ for each n, which are shown in Fig. 4.4, are computed as

$$a_n(t_p) = \cos^2(\frac{\Omega_{n,n-1}t_p}{2})$$
$$b_n(t_p) = 1 - a_n(t_p) = \sin^2(\frac{\Omega_{n,n-1}t_p}{2})$$
(4.9)

where t_p is the length of the RSB pulse. We construct a column vector whose elements correspond to the motional population p_n for each n:

$$\boldsymbol{p} = \begin{pmatrix} p_0 \\ p_1 \\ p_2 \\ \vdots \end{pmatrix}$$
(4.10)

The dynamics of the motional population by the single cooling cycle can be represented by the following matrix:

$$A(t) = \begin{pmatrix} 1 & b_1(t) & 0 & \cdots \\ 0 & a_1(t) & b_2t & \cdots \\ 0 & 0 & a_2(t) & \cdots \\ \vdots & \vdots & \vdots & \ddots \end{pmatrix}$$
(4.11)

where the diagonal elements indicate the probability that the motional state stays in the same state, and the off-diagonal elements represent the cooling

$$\boldsymbol{p}' = \begin{pmatrix} p_0' \\ p_1' \\ p_2' \\ \vdots \end{pmatrix} = \begin{pmatrix} 1 & b_1(t) & 0 & \cdots \\ 0 & a_1(t) & b_2t & \cdots \\ 0 & 0 & a_2(t) & \cdots \\ \vdots & \vdots & \vdots & \ddots \end{pmatrix} \begin{pmatrix} p_0 \\ p_1 \\ p_2 \\ \vdots \end{pmatrix}.$$
(4.12)

The final motional population at the end of a series of cooling cycles can be obtained by the following matrix equation:

$$P_{final} = A_m A_{m-1} \cdots A_1 P_{initial}$$
(4.13)

where A_n is a matrix in Eqn. 4.11 with a pulse time $t = t_n$ for each n.

The final achievable motional ground state population p_0 is strongly dependent

on the pulse sequence: the pulse time for each RSB pulse and the number of cooling cycles applied. This fact requires us to optimise our sequence such that we achieve p_0 close to the unity taking a sufficiently short time for the whole series of cycles. The main obstacle we face in terms of pulse optimisation is that the coupling strength of the red sideband transitions varies with n, so there is no such single probe time that leads to complete population inversion between $\left|S_{1/2,1/2}, n\right\rangle$ and $\left|D_{5/2,1/2}, n-1\right\rangle$ for all n (i.e. b_n cannot be 1 for all n).
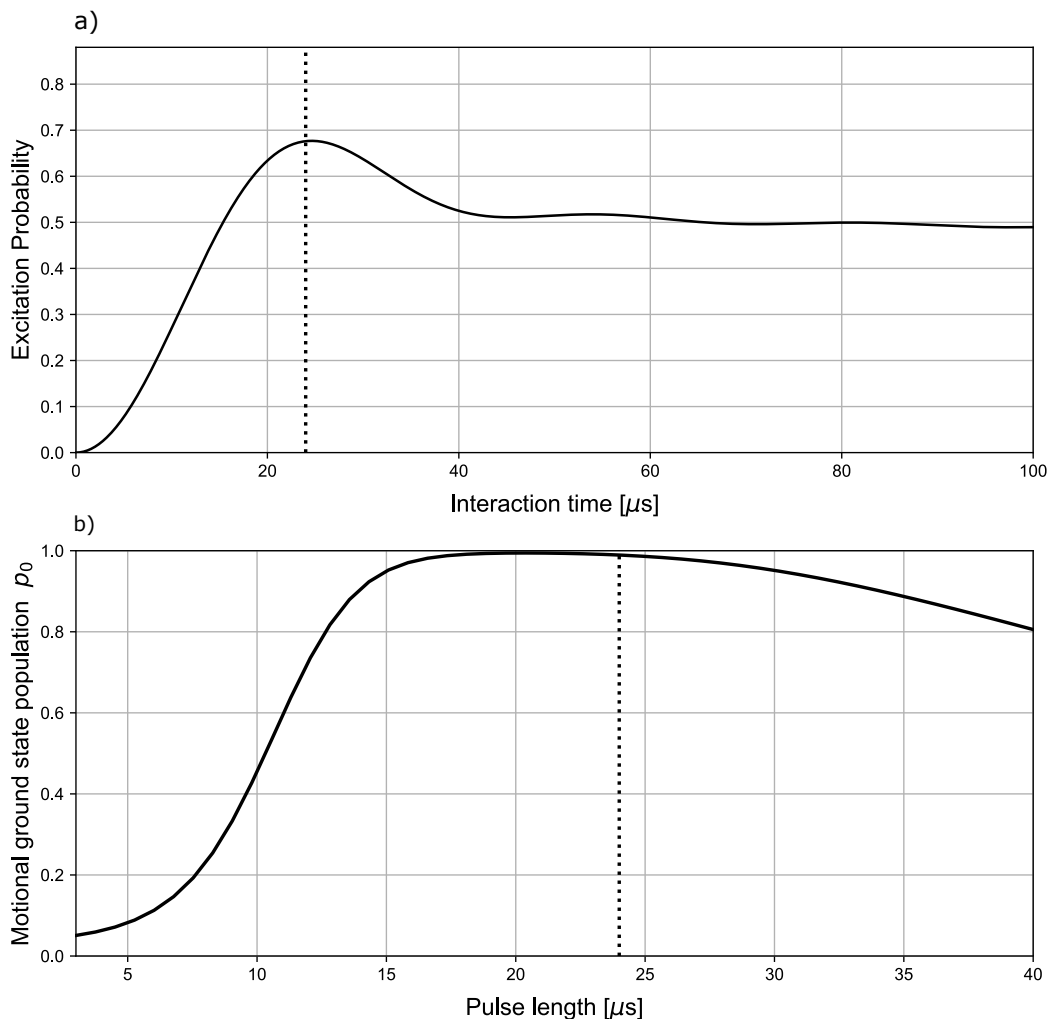
Figure 4.5: Pulsed sideband cooling with a constant pulse time with the initial $\bar{n} = 30$ a) Rabi oscillation on the red sideband with the ion Doppler cooled. The dotted line indicates the interaction time at which the excitation probability in the Rabi oscillation becomes maximum. b) Motional ground state population p_0 after 200 sideband cooling pulses with the different values of constant pulse time.

Fig. 4.5(b) shows the p_0 with different values of constant pulse time. The value of the constant pulse time is selected by the Rabi oscillation on the red sideband with an initially Doppler-cooled ion. We choose the pulse time such that the Rabi oscillation on the red sideband reaches the first maximum, which indicates the change

in $\bar{n}$ by the transition becomes maximised. The maximum occurs at roughly the same probe time even after some cooling cycles are performed. Fig. 4.5(b) shows our choice of t is not optimal but brings p_0 to close to the minimum possible value, and the corresponding constant time t_p can be easily determined by measuring the Rabi oscillation on the red sideband.
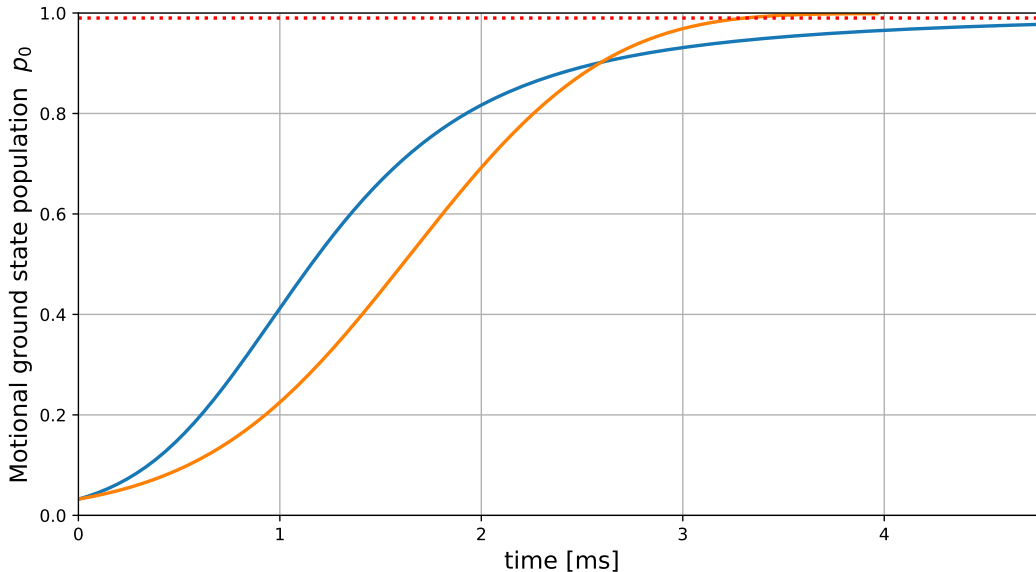
Figure 4.6: The motional ground state population p_0 while the SBC pulses are applied, following the two different pulse schemes: constant time (blue) and variable time (orange). Initially, p_0 increases more rapidly with the constant time method, but the cooling rate significantly decreases afterwards.

The next approach is to vary the pulse time for each pulse. We first decide the number of cycle applied n_{max}, and we choose the probe time for the first pulse as $t_1 = \pi/\Omega_{n_{max},n_{max}-1}$, which is π time for motional state $|n = n_{max}\rangle$. Then, we choose π time for $|n_{max} - 1\rangle$ for the pulse time of the subsequent RSB pulse. Finally, the last pulse time is $t_{n_{max}} = \pi/\Omega_{1,0}$. This pulse sequence ideally transfers the population of $|n\rangle$ for $n \leq n_{max}$ to the motional ground state $|0\rangle$. If we achieve $\bar{n} \approx 30$ after Doppler cooling, more than 99% of total population lies in the motional state $|n\rangle$ with $n \leq 200$, so 200 RSB pulses should be sufficient to prepare the ion in the motional ground state with fidelity greater than 99%.

Fig.4.6 compares the two schemes. The constant pulse time shows the motional ground state population p_0 initially increases much faster but also rapidly saturates below 0.99. In contrast, the variable time method takes a shorter time to achieve p_0 above 0.99.

4.2.2 Continuous Sideband Cooling

In contrast to pulsed SBC, in continuous SBC, the red sideband transition is continuously driven together with the re-pumping lasers at 854 nm. The lifetime of the $D_{5/2}$ state is 1.2 s, which prolongs the cooling process, but the laser at 854 nm continuously re-pumps any population of $D_{5/2}$ to the $P_{3/2}$ state, and the ions are adiabatically transferred to $S_{1/2}$. This re-pumping laser effectively broadens the linewidth of the transition $S_{1/2} \leftrightarrow D_{5/2}$, and a mathematical description of the dynamics is more complicated than the case of the pulsed SBC[2].

One caveat regarding the implementation of the continuous SBC is that the measured trap frequency through frequency spectra is different from the trap frequency required for the continuous SBC because the re-pumping laser, which is continuously switched on during the cooling, produces an AC Stark shift to $\mathbf{D}_{5/2}$. The re-pumping laser, however, must be turned off while we measure frequency spectra of the ion to avoid deshelving of the $D_{5/2}$ state, and the measured trap frequency does not account for the AC Stark shift by the re-pumping laser. In other word, we have to measure the amount of AC Stark shift by the 729 nm laser.

The cooling rate and cooling limits are strongly dependent on the power of the 729 nm laser and the detuning. This requires us to optimise the laser parameters.

4.3 Temperature Diagnostic

After all cooling processes (Doppler cooling, SBC) are completed, we must ensure the ion is properly initialised to its motional ground state by measuring its temperature. To measure the temperature of the ion, we measure either the frequency spectra of the ion, including the carrier and the first order of the red and blue sidebands or the Rabi oscillation, because their features change depending on the ion's temperature. If the ion reaches its Doppler cooling limit (i.e. thermal equilibrium), a so-called thermal state of the ion's motion is given by

$$\rho_{th} = \sum_{n=0}^{\infty} p_n \left| n \right\rangle \left\langle n \right|, \quad p_n = \frac{\bar{n}^n}{(\bar{n}+1)^{n+1}} \tag{4.14}$$

where $\bar{n}$ is the average phonon number. Using the generalised Rabi oscillation in Eqn. 3.17, the Rabi oscillation of the ion in thermal state with $\bar{n}$ can be written as follows:

$$P_e(t) = \sum_{n=0}^{\infty} p_n \frac{\Omega_{n,m}^2}{\Omega_{n,m}^2 + \Delta^2} \sin^2\left(\frac{\Omega_{n,m}t}{2}\right) \tag{4.15}$$

---

[2]The more rigorous mathematical description of the cooling process can be found in Ref. [75, 76]
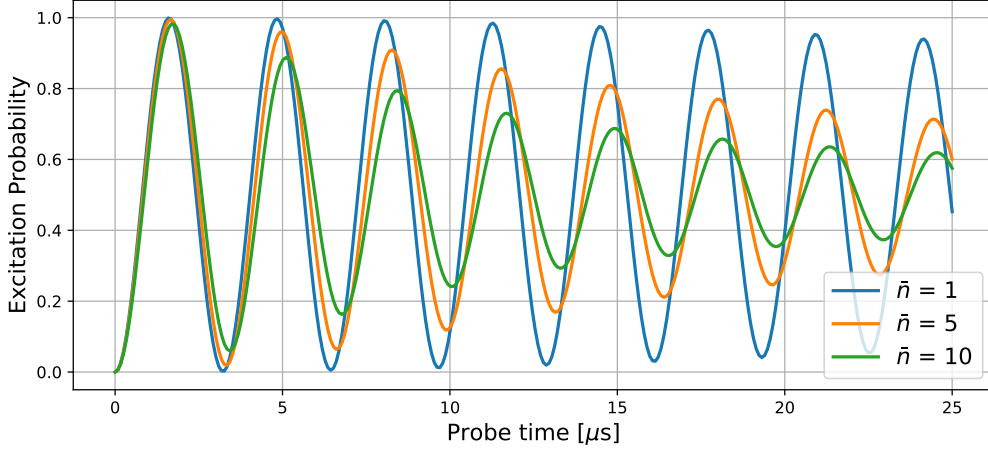
Figure 4.7: Numerical simulation of Rabi oscillation on the carrier with different $\bar{n}$. The contrast of the oscillation decays faster as $\bar{n}$ increases.

where p_n is defined in Eqn. 4.14. Eqn. 4.15 suggests that the frequency spectrum and Rabi oscillation have different features, depending on average phonon number $\bar{n}$. For instance, Fig. 4.7 suggests that the visibility of the Rabi oscillation decays due to dephasing of the different motional states and decays faster as $\bar{n}$ increases. Hence, the frequency spectrum and the Rabi oscillation can be used to estimate the temperature of the ion. Fig. 4.8 shows experimental results of Rabi oscillation on the carrier to support that argument: the visibility of Rabi oscillation on the carrier is not rapidly washed out if the ion is sideband cooled, and the fit suggests its $\bar{n}$ is 0.3.

If the average phonon number $\bar{n}$ approaches zero, most of the motional populations are in the motional ground state, and $\bar{n}$ can be more straightforwardly estimated by measuring the ratio of the heights of the first-order red and blue sideband spectral peaks. From Eqn. 4.15, we can obtain an expression for the excitation probability of the ion when the ion is driven by the first-order red sideband, and the expression can be rewritten in terms of the excitation probability of the first-order blue sideband $P_{e,rsb}(t)$:

$$
\begin{aligned}
P_{e,rsb}(t) &= \sum_{n=1}^{\infty} p_n \sin^2\left(\frac{\Omega_{n,n-1}t}{2}\right) \\
&= \sum_{n=0}^{\infty} p_{n+1} \sin^2\left(\frac{\Omega_{n,n+1}t}{2}\right) \\
&= \frac{\bar{n}}{\bar{n}+1} \sum_{n=0}^{\infty} p_{n+1} \sin^2\left(\frac{\Omega_{n,n+1}t}{2}\right) \\
&= \frac{\bar{n}}{\bar{n}+1} P_{e,rsb}(t)
\end{aligned}
\tag{4.16}
$$

By re-arranging Eqn. 4.16, we can write $\bar{n}$ in terms of the ratio of red and blue

41
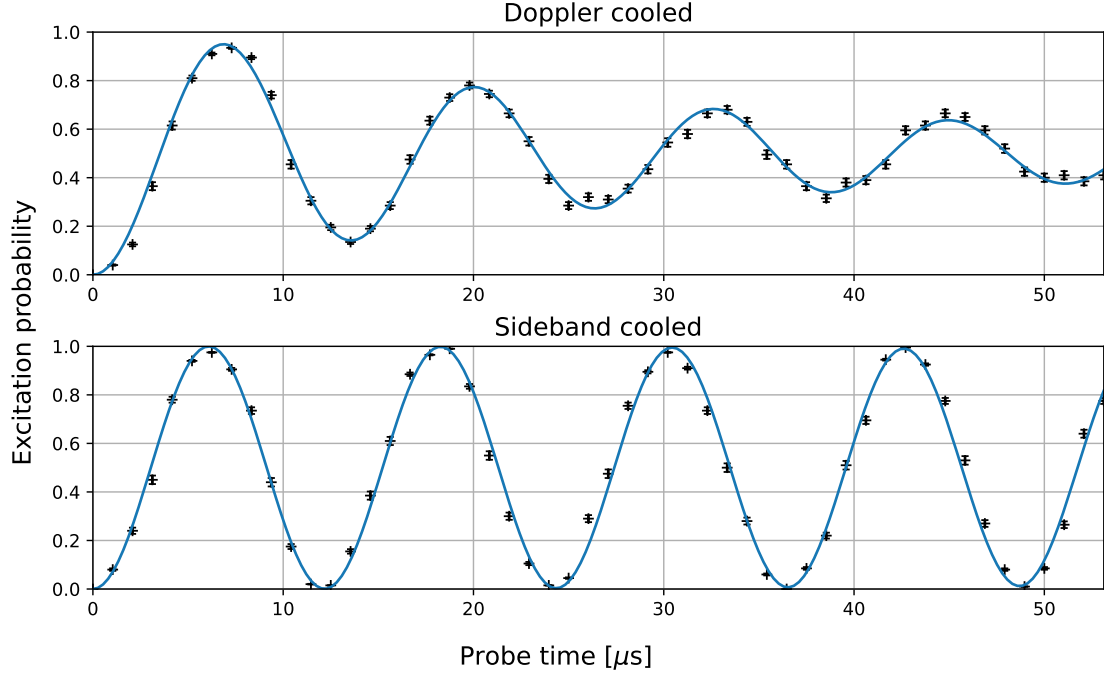
Figure 4.8: Rabi oscillation on the carrier with the ion Doppler (upper) and sideband (lower) cooled. The fits suggests the Doppler temperature and the sideband temperature are $\bar{n} = 18$ and $\bar{n} = 0.3$, respectively.

sideband spectral amplitudes $R = P_{e,rsb}(t)/P_{e,bsb}(t)$:

$$\bar{n} = \frac{R}{1-R}. \tag{4.17}$$

We can simply estimate the temperature of the ion by looking at the ratio of heights of red and blue sideband spectral peaks. For instance, if $\bar{n} = 0$, the ratio is zero as the red sideband does not induce any population transfer if the ion is in the motional ground state. Fig. 4.9 and 4.10 show frequency spectra including the carrier and the first-order red and blue sidebands with the ion Doppler cooled and sideband cooled, respectively. It is important to note that the excitation probability of the red sideband frequency is nearly zero while the blue sideband and the carrier still excite the ion if the ion is sideband cooled. This is because if the ion is in the motional ground state, the ion is excited when it is driven on the resonance of the blue-sideband transition, while it is decoupled from the laser when the laser is on the resonance of the red sideband.

4.4   Heating Rate

The trapped ion experiences motional heating due to many different sources, including the electrical noise of the trap electrodes. Unfortunately, the exact mechanism of the heating is still unknown. It is important to measure the heating rate to make
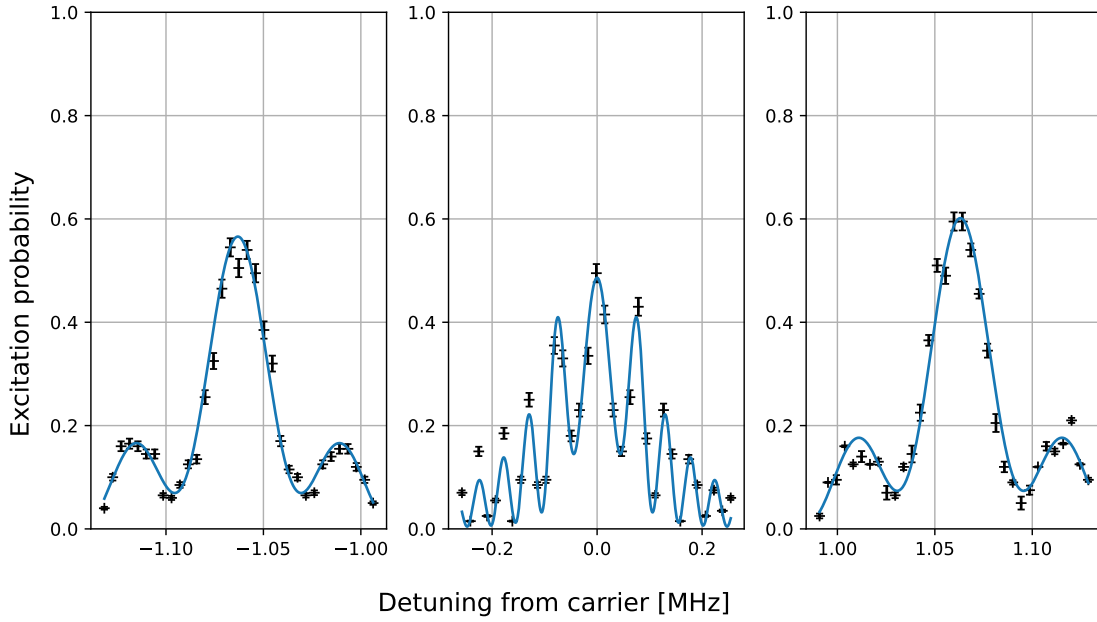
Figure 4.9: Motional spectra of the Doppler-cooled ion taken on $S_{1/2,1/2} \leftrightarrow D_{5/2,1/2}$, including the carrier and the red and blue sidebands. The trap frequency is 1.064 MHz and the Rabi frequency is 80 kHz. The fits suggests $\bar{n} \approx 17(9)$, which is consistent with $\bar{n}$ given by the Doppler limit ≈ 17.2.

sure the temperature of the ions is kept sufficiently low while a single- or two-qubit gate is driven. We use Eqn. 4.17 to measure the temperature. Thus, we measure the red and blue sideband peaks in our measurement of heating rate, but in this case, we insert a delay with a variable amount of time between the cooling and a spectroscopic pulse. Fig. 4.11 illustrates that the average phonon number $\bar{n}$ increases as the length of the delay increases. Assuming the ion is heated at the constant rate $\dot{\bar{n}}$, the fit estimates $\dot{\bar{n}} = 36.7(1)$ phonon/s. This magnitude of the heating rate is somewhat higher than the typical value found in the linear Paul trap in the similar size. This suggests there must be some heating sources, but unfortunately we could not identity them. Reducing the heating rate has to be be a priority to implement quantum gates with high fidelity.
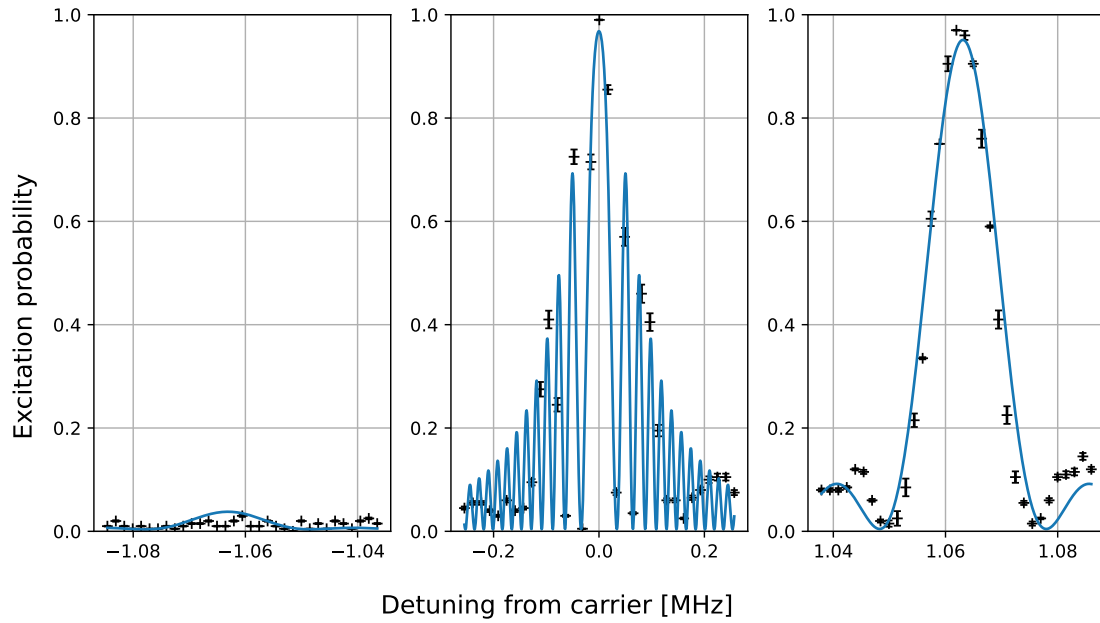
Figure 4.10: Motional spectral of sideband cooled ion. The trap frequency is $1.064\,\text{MHz}$, and the Rabi frequency is $81.6\,\text{kHz}$. The fit suggests $\bar{n}$ is $0.3(2)$.
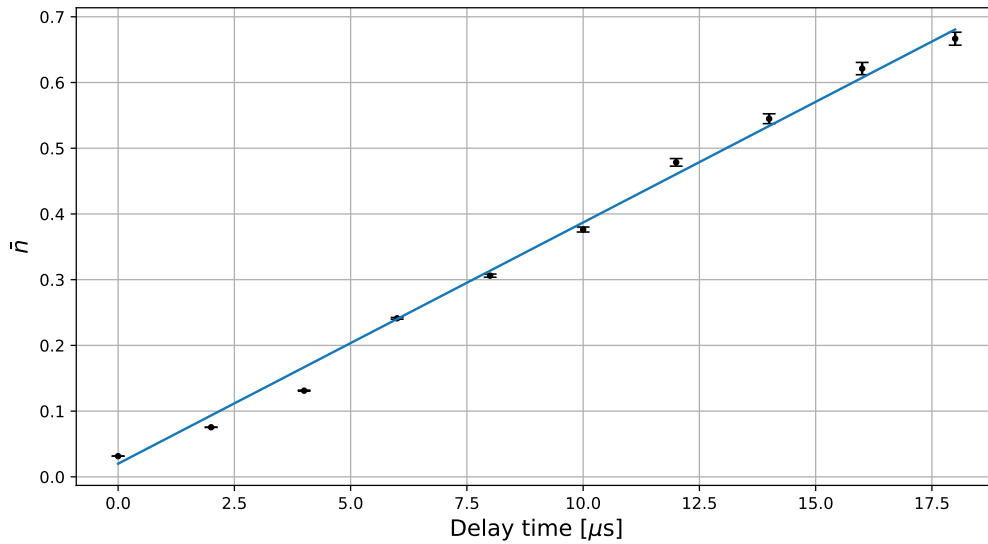
Figure 4.11: Averaged phonon number $\bar{n}$ as a function of the length of delay time inserted between the cooling and spectroscopic probes.

Chapter 5

Experimental Setup

This chapter will present the experimental apparatus, which comprises a vacuum system, lasers, associated optical setups, electronics that generate the required electric and magnetic fields and an experimental control system. As we recently built a macroscopic linear Paul trap, in the early stage of this PhD, we characterised the new trap before we proceeded to the main experiment: we measured the atomic resonance frequency and harmonic frequency of the trap and assembled and characterised optical setups and the associated electronics to ensure they worked as expected. Preparing the experimental apparatus for the main experiment required extensive collaboration with my colleagues; I will cite their works to acknowledge their contributions.

5.1 Vacuum System

It is imperative to achieve an appropriate vacuum level inside a chamber that accommodates trap electrodes because trapped ions can be ejected from the trap by colliding with any other particles left in the vacuum chamber (background gas). Storing ions as long as we desire (i.e. a few hours or even a few days) requires an ultra-high vacuum (UHV) inside the chamber. The vacuum system includes a vacuum chamber, associated vacuum pumps and an atomic oven. The vacuum system was designed, assembled and initially characterised primarily by Oliver Corfield and Johannes Heinrich. Typical design choices include the structure of the chamber, the vacuum components and the materials used. In addition, achieving a UHV inside the chamber involves several processes [43]: (i) bakeout of the system to eliminate gas molecules adsorbed on the trap electrodes and the surface of the chamber, which degas as the pressure inside the chamber decreases, (ii) initial pumping to $\approx 10^{-7}$ mbar with a scroll pump and a turbo pump (iii) pumping further to UHV using an ion pump. The details of chamber design, all vacuum parts and the procedures involved in pumping the chamber to UHV with the relevant experimental results from the initial characterisation are available in the PhD thesis of Oliver Corfield [56].
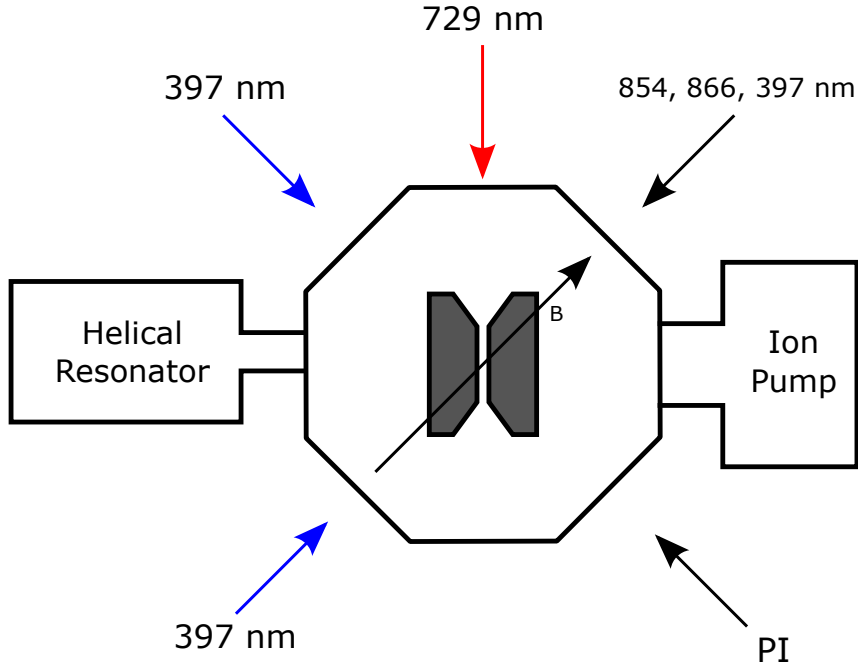
Figure 5.1: Diagram of vacuum chamber with attached components and the lasers shooting at the trap. The 729 nm laser is directed along the trap axis. The quenching lasers (854 and 866 nm) and the Doppler cooling and state preparation lasers (two 397 nm lasers) are co-propagating along the quantisation axis, which is defined by an external magnetic field $\boldsymbol{B}$. There are two sets of 397 nm lasers: one counter-propagating to the quenching lasers, and the other is directed perpendicular to the quantisation axis. These two lasers are used for Raman interaction. Lastly, the photoionisation (PI) beam is also propagating perpendicular to the quantisation axis.

The chamber is an octagon; it has one viewport on each side. One viewport has the rf electrical feedthrough, which is connected to a helical resonator that produces the required time-varying trapping field, and another is connected to an ion pump that keeps the pressure inside the chamber below 10^{-11} mbar. The other viewports are equipped with anti-reflective coated windows, and the lasers are delivered to trapped ions through those windows. There is another window on the top of the chamber. The window is connected to a tube that houses lenses that focus light scattered from the ion to either a photomultiplier tube (PMT) or electron-multiplying CCD camera (EMCCD) to better collect the fluorescence from the ion (see Fig. 5.7 for more details of the detection optics). The DC feedthrough that is positioned on the bottom of the chamber is connected to a pair of end-cap electrodes and compensation electrodes.

5.2 Lasers

In our experiments, cooling and all coherent logic operations on trapped ions are performed via lasers; lasers at many different wavelengths are used in our experiment:

375, 397, 423, 729, 854, 866 nm. The lasers can be mainly categorised into four purposes: Doppler cooling, re-pumping, photoionisation and spectroscopy. The first three categories will be discussed in this section. The details of the optical setup and maintenance procedure concerning the primary spectroscopy laser at 729 nm will be given in the next chapter (Chapter 6).
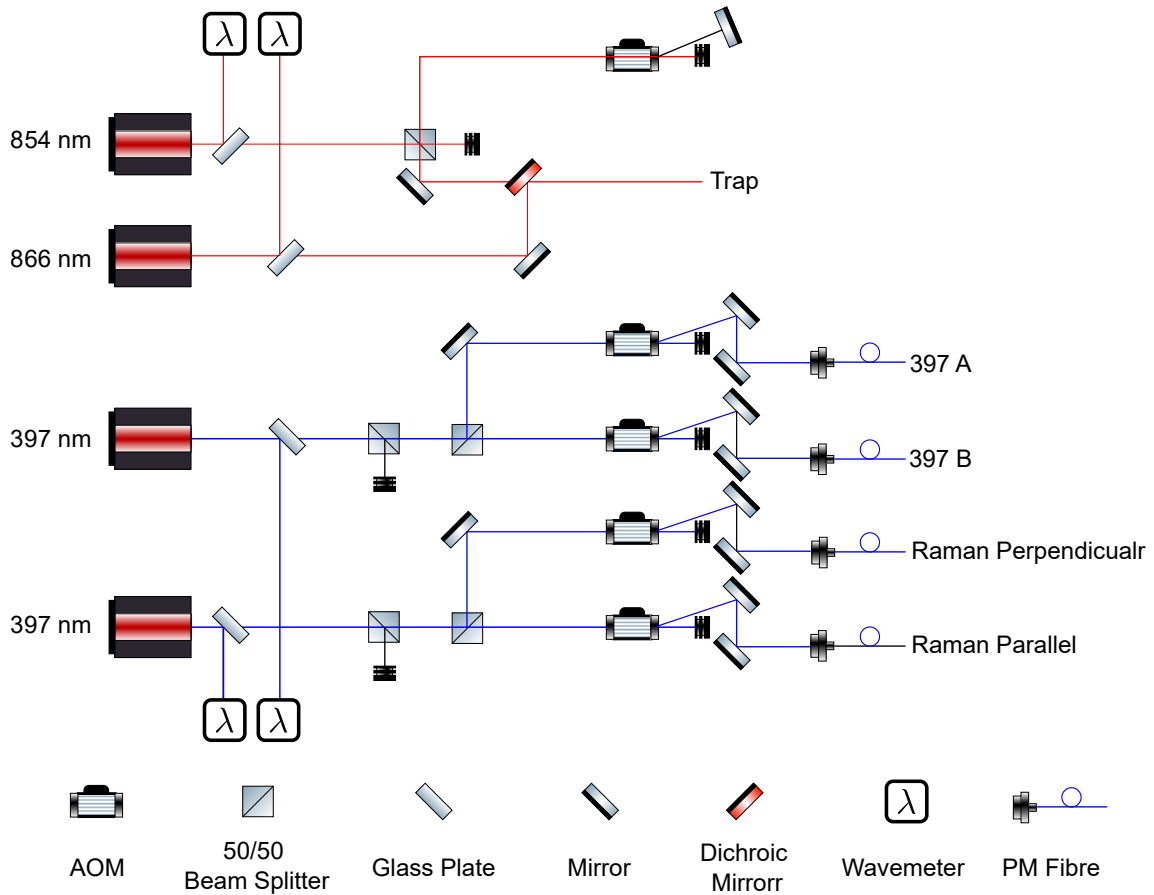
Figure 5.2: Layout of optics in the first stage, including mirrors and beam splitters. Some mirrors are omitted in the diagram to simplify the diagram.

The laser system is divided into two stages. In the first stage, the light beams emitted from the commercial EDCLs are directed to the corresponding AOMs by a set of mirrors, and the first-order diffracted beams from the AOMs are coupled to the optical fibres and sent to the next stage. The second stage consists of the mirrors and lenses that direct the beams to the trap at an appropriate angle with respect to the trap axis (see Fig. 5.1).

All lasers, except the 866 and 854 nm lasers[1], are fibre coupled before they are delivered to the trap. The alignment of the beams with respect to the trap and quantisation axis is unchanged as long as the optics after the fibre couplers stay the same. This makes it easy to modify the optics in the first stage without the need

---

[1]We plan to make these two lasers fibre coupled as well.

to re-align the beams to the trapped ion if we need to add optical components and lasers: coupling the beam into the optical fibre is much more straightforward than aligning the beam with respect to the ion.

5.2.1 Wavemeter Frequency Locking

The lasers other than the primary spectroscopic laser at 729 nm drive dipole transitions, whose linewidths typically are a few tens of MHz; hence, these lasers is not required to have sub-kHz stability. All lasers involved in our experiment are external cavity diode lasers (ECDL)[2], and they are equipped with voltage modulators, which control a piezo attached to the laser cavity so that the laser frequency can be systematically manipulated by changing the voltage applied to the cavity piezo. The frequencies of these lasers are stabilised via a PID feedback loop based on the frequency measurement by a wavemeter[3]. The wavemeter, which is an optical interferometer, can measure the wavelength of a laser with an accuracy of approximately 2 MHz, and the measurements are sent to the experimental computer. We used a computer program to construct the PID controller, which digitally computes a control signal based on the received measurements rather than an electric circuit (analog controller). The dedicated program[4] takes the frequency measurement from the wavemeter, calculates the error signal $\Delta = \nu_{\text{target}} - \nu_{\text{L}}$ and generates the control signal. Then, the control signal is sent to the corresponding laser controllers via Ethernet network, manipulating the frequency of the laser accordingly and suppressing frequency jitter. The frequency locking with the wavemeter stabilises a laser within a level of roughly 1 MHz, which is much narrower than the linewidth of the dipole transitions the lasers are targeting.

5.2.2 Acousto-optic Modulator (AOM)

A laser-induced coherent logic operation on a trapped ion requires precise timing ($\approx 1\,\mu$s) and frequency manipulation of the laser pulse. We use an acousto-optic modulator (AOM) that diffracts the light incident on a crystal in the AOM using the acousto-optic effect to generate the pulse that satisfies those strict requirements.

---

[2]All commercial lasers from Toptica. The specific models of each laser: DLC pro 729 for the 729 nm laser, DLC pro 850s for the 854 and 866 nm lasers and DLC pro HP 397s for two 329 nm lasers.

[3]HighFinesse WS8-10

[4]The laser locking program is written in Python. Johannes Heinrich initially wrote the program to replace the commercial software provided by HighFinesse, a manufacturer of the wavemeter, to be able to customise the program such that it supports features for the specific needs of our experiment. Simon Webster subsequently modified the program for a better user interface and compatibility with the new control system, ARTIQ.
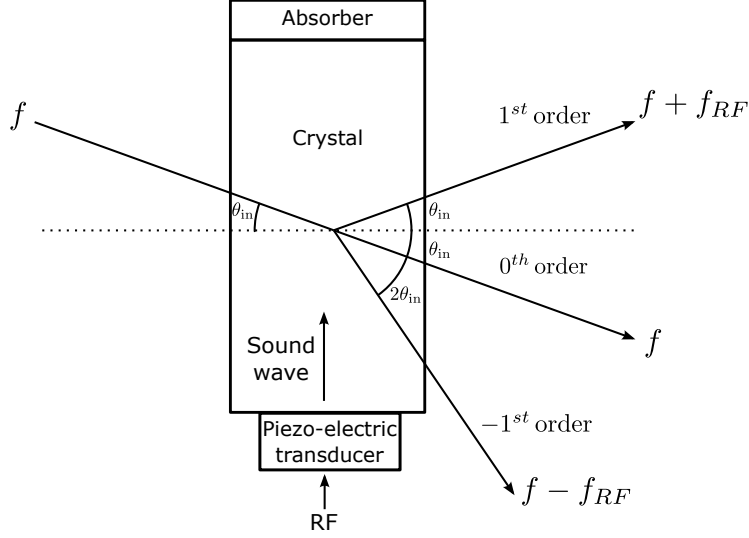
Figure 5.3: Schematic diagram of acousto-optic modulator (AOM), showing the beam geometry of incoming and outgoing beams ({-1,0,1}th-order diffracted beams)

A piezoelectric transducer is attached to the AOM crystal (see. Fig. 5.3), and the diffraction efficiency varies with the rf power applied to the piezo [77]:

$$\eta = \frac{I_1}{I_0} = \sin^2\left(\frac{\pi}{2}\sqrt{\frac{P_{\text{in}}}{P_{\text{sat}}}}\right) \tag{5.1}$$

P_{in} and P_{sat} are the power of the applied rf field to the piezo and the saturation power at which the maximum diffraction efficiency is achieved, respectively. The AOM also shifts the frequency of the light. The frequency of the mth-order diffraction is shifted by the frequency of the applied acoustic wave f_{RF}, which can be controlled by controlling the frequency of the rf signal applied to the piezo: $f \rightarrow f + mF_{RF}$. The AOM allows for fast power and frequency manipulation, and the AOM also effectively serves as a switch for the laser – it turns the beam on and off with a short latency (100s ns).

We routinely measure the optical power of the 729 nm laser, which is related to the Rabi frequency, with different rf powers applied to the AOM (see Fig. 5.4) to calibrate the AOM. We can measure the conversion factor between the optical power and Rabi frequency by measuring the Rabi oscillation with the given optical power. Consequently, we can relate the AOM rf power to the Rabi frequency, and this calibration allows for a calculation of the rf power required to achieve a particular Rabi frequency. This is convenient in performing many scan routines (i.e. frequency spectrum to measure resonance frequency and Rabi-type time scan to measure the Rabi frequency). We can easily set the frequency and time span range for the frequency and time scan.

The AOM can be used to generate a polychromatic laser, which is required for AC Stark shift compensation and implementation of a Mølmer–Sørensen gate [78].

49
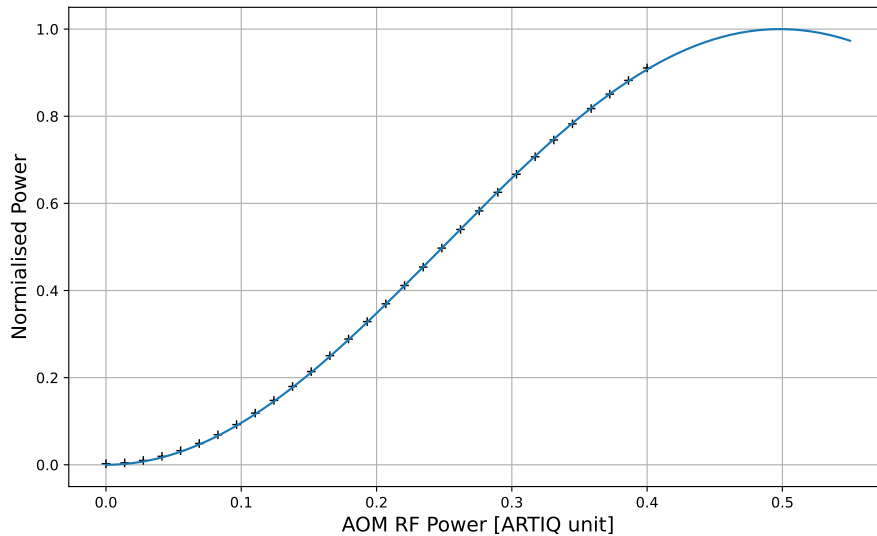
Figure 5.4: Normalised power of the first-order diffraction of the AOM as a function of the rf power applied to the AOM. The rf power to the AOM is controlled by ARTIQ. Its absolute power is not important, but the rf power in the ARTIQ unit, which is the numerical value used in the ARTIQ script only matters.

If the rf signal applied to an AOM consists of multiple frequency components, each tone of the signal causes frequency shifts individually to the diffracted beam by the frequency of respective components; for example, if the rf signal has two frequency components, f_1 and f_2, then the frequency of the first-order diffracted beam includes $f' = f + f_1 + f_2$.

5.2.3 Doppler Cooling and State Preparation

Both Doppler cooling and state preparation are performed via a dipole transition $S_{1/2} \leftrightarrow P_{1/2}$ that is driven by a $397\,\mathrm{nm}$ laser. As shown in Fig. 5.1, both $397\,\mathrm{nm}$ lasers are directed along the magnetic field, which makes an angle of 45 degrees with reference to the trap axis. The wavevector of the Doppler beam is projected onto all principal axes of the trap, and this geometry allows the single Doppler beam to cool the ion's motion in all three directions.

The beams are transmitted through respective polarising beam splitters (PBS). The beams are horizontally polarised; both $\sigma_\pm$ transitions are used for Doppler cooling. However, the beam for state preparation has to induce only a σ_+ transition, which optically pumps the population of $S_{1/2,-1/2}$ into $S_{1/2,-1/2}$. Hence, we additionally place a $\lambda/4$ waveplate [5] in this beam to make the beam left-circularly polarised. There are $\lambda/2$ waveplates before the PBSs, and those waveplates allow for systematic control of the optical power of the beams sent to the ion by rotating the principal

---

[5]We can selectively prepare the ion in either state of the $S_{1/2}$ sublevels with appropriate settings of the $\lambda/4$ waveplate.

axis of the waveplates.

5.2.4   Re-pumping
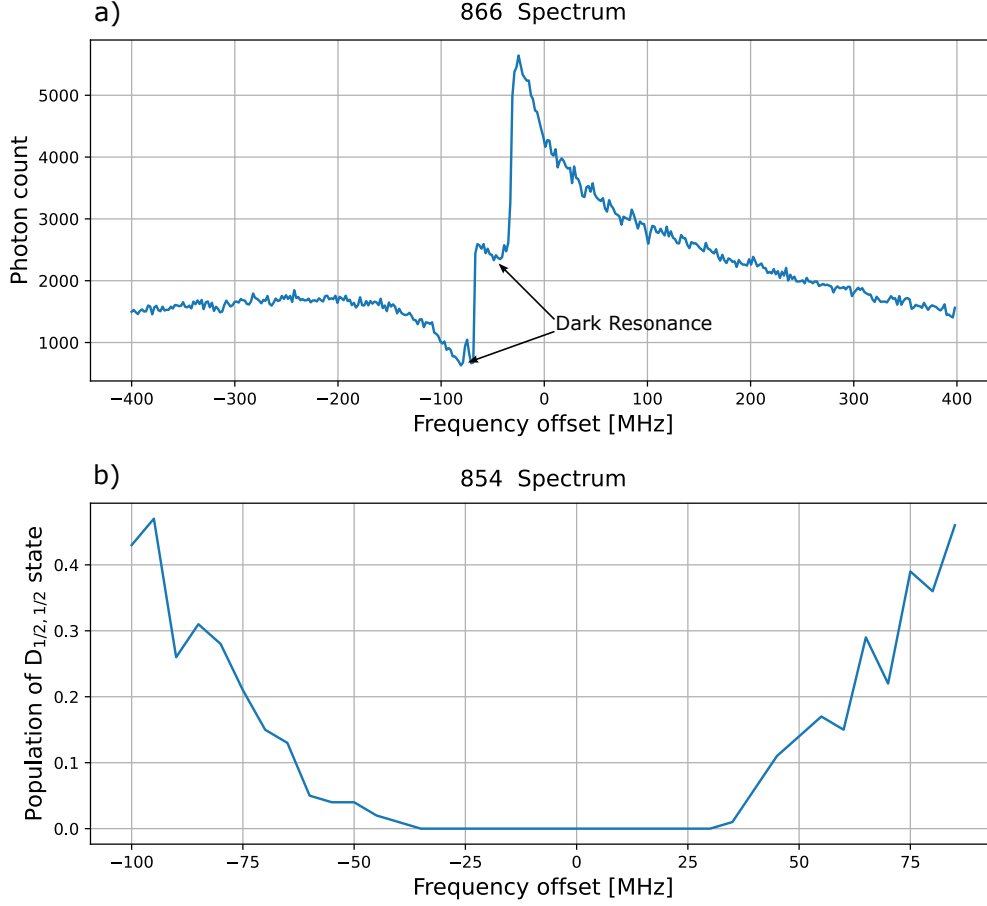
Figure 5.5: 866 and 854 nm frequency spectra. a) collected fluorescence during the time bin of 200 ms as we scan the frequency offset of the 866 nm laser. There are several dips, indicating dark resonances. b) Population of the $D_{5/2,1/2}$ state after the de-shelving the $D_{5/2,1/2}$ state using a 854 nm laser for 6 μs. As the frequency approaches resonance, more of the population of $D_{5/2,1/2}$ is re-pumped to $S_{1/2}$. This allows us to estimate the resonance frequency.

Two quenching lasers at 866 and 854 nm allow for optical pumping of the population of $D_{3/2}$ and $D_{5/2}$ states, respectively. The 866 nm laser does not pass through an AOM because the beam is always switched on, continuously pumping the population of the $D_{3/2}$ state out. In contrast, the 854 nm laser must be turned off while we manipulate the qubit via the $S_{1/2} \leftrightarrow D_{5/2}$ transition; the 854 nm laser is coupled to an AOM, which acts as a switch.

We set the frequency of the 866 nm laser slightly blue detuned to avoid dark resonances. The Doppler beam at 397 nm is red detuned. If the 866 nm laser is also red detuned such that the detuning is comparable to the detuning of the Doppler beam, these two lasers result in population trapping, stopping the ion from scattering

397 nm photons and significantly reducing the Doppler cooling rate [79, 80]. As shown in Fig. 5.5, the dark resonance modifies the spectral shape of the Doppler transition and results in a narrow dip in fluorescence.

The 854 nm laser's frequency must be tuned close to the resonance to efficiently quench the $D_{5/2}$ state, and we need to measure the resonance of the transition. We prepare the ion in $D_{5/2}$ using a resonant π pulse of the 729 nm laser, turn off the 729 nm laser and apply a $6\,\mu s$ pulse of the 854 nm laser. Then, we measure the excitation probability and repeat this with different frequencies of the 854 nm laser. As the frequency approaches resonance, the laser more quickly re-pumps the $D_{5/2}$ state, reducing the excitation probability to zero, which is indicated by a dip in Fig. 5.5(b).

5.2.5   Photoionisation

As explained in Sec. 2.5, the loading of $^{40}Ca^+$ into the trap is achieved by isotope-selective photoionisation that involves two lasers at 375 and 423 nm. The first excitation driven by the 423 nm laser is a resonant process, while the second excitation driven by the 375 nm laser is not. The frequency of the 423 nm laser is locked using the wavemeter, but the 375 nm laser runs freely without frequency stabilisation as the linewidth of the laser is not crucial.
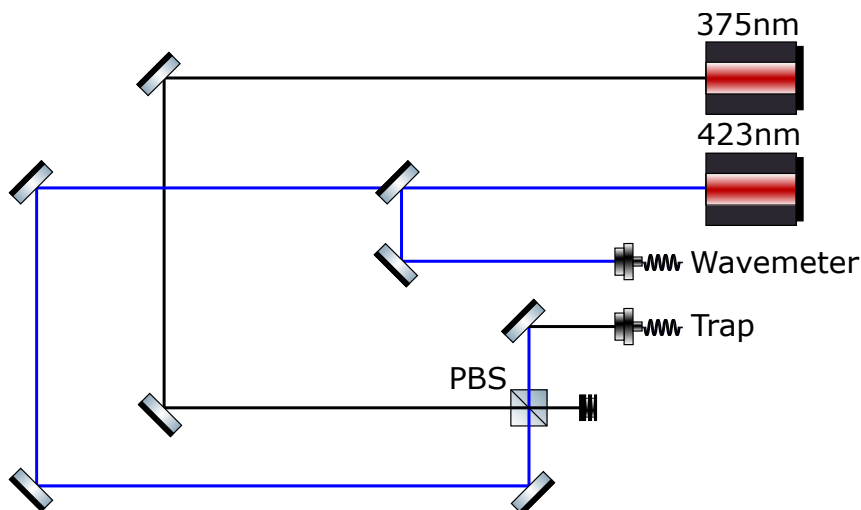
Figure 5.6: Optical setup for two photoionisation beam. Only the frequency of the 423 nm laser is monitored. The two beams are combined on the PBS and launched into the single optical fibre.

To increase the efficiency of photoionisation, the two beams must be maximally spatially overlapped so that the two transitions involved in the loading process occur simultaneously. Hence, we combine the beams on PBS and couple the combined beams into a single optical fibre (see Fig. 5.6); the other end of the fibre coupler outputs the beams where these two lasers are co-propagating. In addition, we use a

telescope, which consists of two concave lenses, to collimate the beams with a smaller beam size of $60\,\mu$m.

5.2.6 Raman Beams

Fig. 5.2 illustrates the optics layout for the Raman beams. The Raman interaction requires two beams at $397\,$nm whose frequencies are separated by the energy difference between the two states we wish to couple. We adopt a single laser to realise the required two beams: we split the single beam into two with the use of a PBS, and each beam goes through independent AOMs. The two beams are derived from the single laser source, so they have the same base frequency. We can make a controllable frequency difference between the two beams by independently controlling the rf frequencies applied to the respective AOMs. Similarly to the other lasers, the two Raman beams are also fibre coupled. The coupling efficiency may drop when we change the frequency of the rf to the AOM; to minimise optical power variation with frequency, we fix the frequency of the rf to the AOM for the *parallel* beam, while the driving frequency of the other AOM is varied when we want to tune the interaction to different transitions (carrier and sidebands).

To make the Raman coupling, each beam must address a different type of transition (π and $\sigma_\pm$). For the given geometry of each beam to the quantisation axis, if we linearly polarise both beams, then the *parallel* beam addresses only the $\sigma_\pm$ transition, while the *perpendicular* beam drives the π transitions.

5.2.7 Imaging System

As explained in Sec. 2.3.2, we measure the qubit state of the ion by counting the photons scattered from the ion while it is illuminated by the Doppler beam at $397\,$nm. We must collect enough photons to discriminate two different photon distributions resulting from two qubit states ($\mathrm{S}_{1/2}$, $\mathrm{D}_{5/2}$). Therefore, the state detection requires an imaging system that sufficiently focuses the beam emitted from the ion down to either a photomultiplier tube (PMT) or an electron-multiplying CCD (EMCCD[6]). Jacopo Mosca Toba primarily designed and built the optical system for the state detection. The detailed optical design and relevant simulation results are available in his master's thesis [81].

As can be seen in Fig. 5.7, the EMCCD cannot only discriminate the bright and dark state of the ion, but also can tell which one is in the bright state when we have multiple ions. However, as the PMT has a better quantum efficiency and allows for much faster measurements, the PMT is more suited for the state detection unless

---

[6]Andor IXon Ultra 897
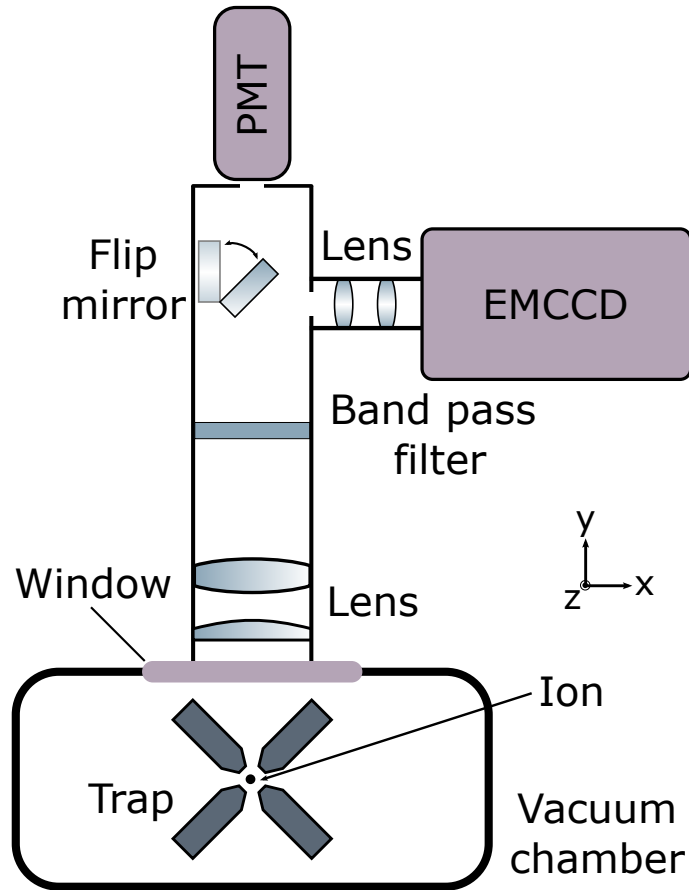
Figure 5.7: Schematic diagram of optical elements involved in collection of fluorescence from the ion, including lenses, mirrors, PMT, and camera. A pair of the lenses focuses the beam scattered from the ion to the PMT and the other pair of the lenses images the ion onto the EMCCD. This diagram was prepared by Jacopo Mosca Toba and is reproduced with permission.

spatial information of ions are required. The detection device can be easily swapped between the PMT and the EMCCD with the use of the customised flip mirror.

5.3   Power Supplies

We use both static and time-varying electric fields in the Paul trap. The static field is generated by a high-precision voltage supply[7]. For the time-dependent electric field, the rf signal is initially generated by the DDS on the ARTIQ board, which is our main control framework, and the signal is subsequently amplified by a high-voltage rf amplifier and a homemade helical resonator with a quality factor Q of approximately 600. The helical resonator resonates at a frequency of 12.38 MHz, which determines the driving frequency of the trap field.

We have found the resonance frequency of the resonator slowly drifts day to day. The drift may be attributed to ohmic heating from the resonator itself while we

---

[7]BK Precision BK9185B
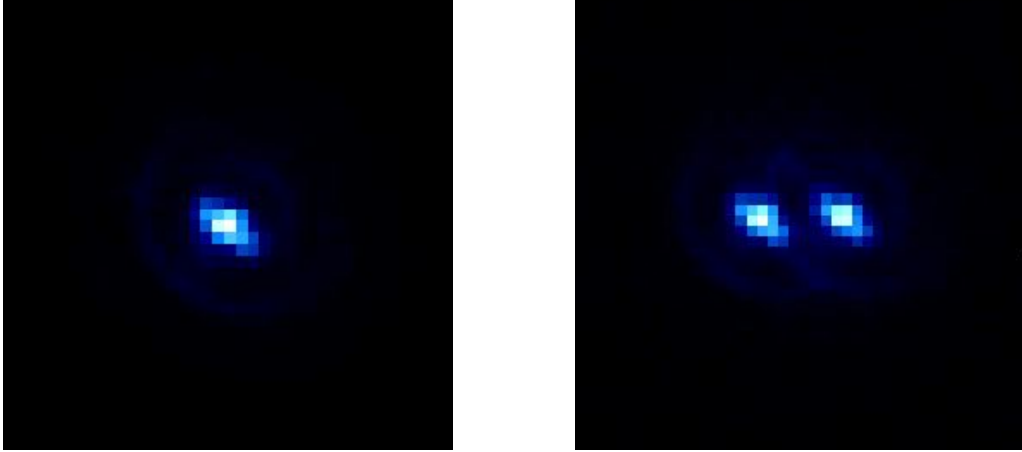
Figure 5.8: Image of a single (Left) and two ion (Right) trapped in our Paul trap using the EMCCD. Each pixel is separated by $16\,\mu$m. The diagram shows our imaging system can spatially resolve each ion.

drive it. We monitor the reflected and transmitted signals from the resonator to ensure our driving frequency is close to the resonance – the reflection is strongly suppressed when the resonator is driven on the resonance. If the driving frequency is somewhat detuned from the resonance, the amount of reflected signal from the resonator increases, and the reflected power might damage the electronics connected to the resonator. Also, if the resonator is not driven on resonance, we need more input power to maintain the same output power – more heat is dissipated, making the ground state cooling more difficult. Thus, before trapping an ion, we routinely measure the resonance frequency of the resonator.

5.4   Magnetic Field Coils

We apply an external magnetic field to define the definite quantisation axis, which determines the coupling strength of each transition (π, σ, δ) with the given geometry of the lasers. There are three orthogonal sets of coils around the vacuum chamber. The main coils generate the primary magnetic field. The vertical and horizontal trim coils are used to precisely align the magnetic field along the desired direction by generating a relatively small amount of the field along the respective directions. As shown in Fig.5.10, the *main* coils are placed at an angle of 45 degrees to the trap axis. The amount of magnetic field generated by the coils increases as the current to the coils increases; we calibrate the coils as we measure the Zeeman splitting of $S_{1/2,1/2}$ and $S_{1/2,-1/2}$ for different current in the coils. At the current status, we use a current of 1.28 A to the *main* coils to produce a magnetic field of approximately $0.32\,$mT, which corresponds to Zeeman splitting of $8.96\,$MHz between $S_{1/2,1/2}$ and $S_{1/2,-1/2}$.
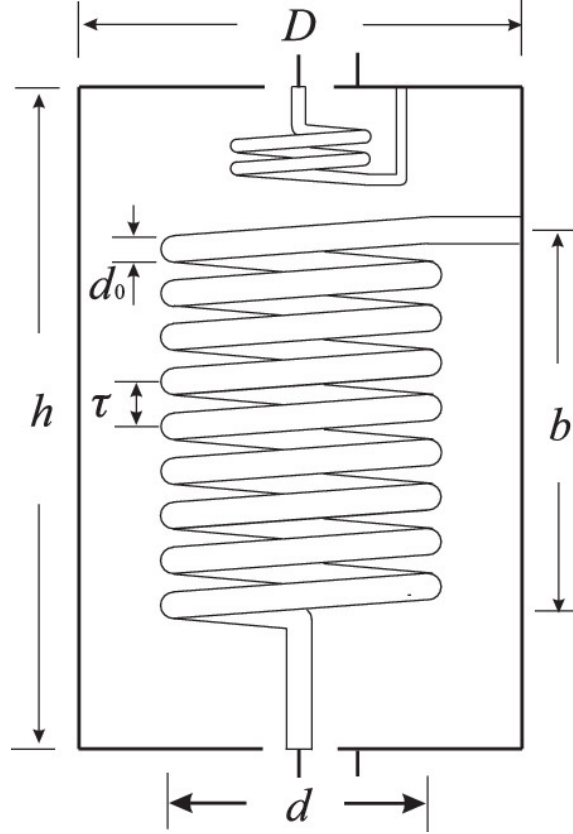
Figure 5.9: Schematic diagram of a helical resonator indicating relevant physical dimension of the resonator. The diagram is adapted from Deng et al.[82]

The magnetic field must be aligned to the direction of the 397 nm laser for state preparation because this laser has to be circularly polarised to address only σ_+. A misalignment makes the laser address the σ_- transition as well, reducing the fidelity of state preparation. For the alignment, we turn on only the state preparation laser and finely tune the direction of the magnetic field with trim coils until the fluorescence level from the ion reaches a minimum. If the laser address only the σ_+ transition, then initially, the ion scatters the photons from the laser because both sublevels of $S_{1/2}$ are populated, but the interaction optically pumps the population of $S_{1/2,-1/2}$ to $S_{1/2,1/2}$. The ion stops scattering the photons, and the fluorescence level becomes as low as background counts.

5.5 Micromotion Compensation

As discussed in Sec 2.1.2, an excess micromotion leads to heating, limiting the final temperature after the resolved sideband cooling. Hence, we need to minimise the amplitude of the excess micromotion. We first need to measure the strength of the excess micromotion, and we use the rf-photon correlation method [83, 84]. The micromotion is oscillatory at the driving frequency Ω of the trap field. As the ion
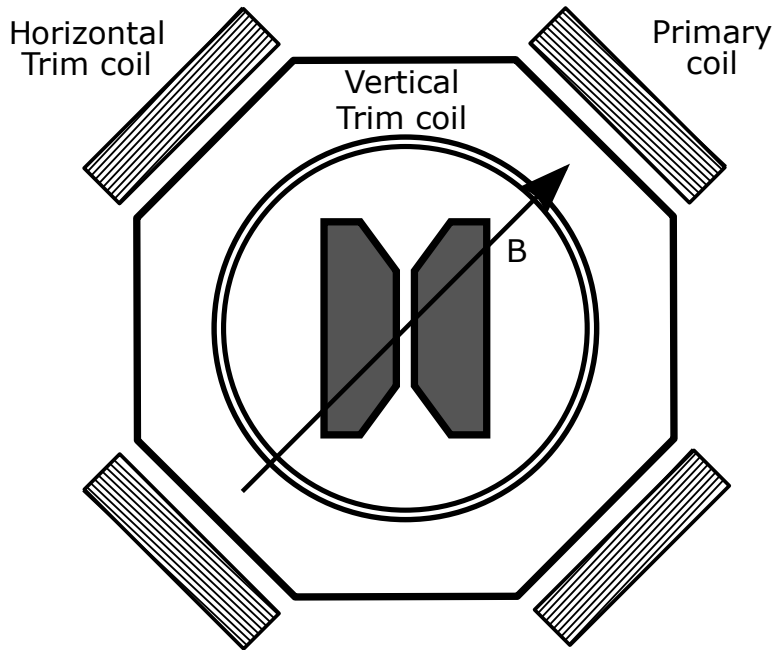
Figure 5.10: The primary coils make a 45-degree angle to the trap axis. There are two pairs of coils. One is on the x-y plane and perpendicular to the orientation of the primary coil, and the other is oriented vertically. The direction of the field is finely tuned by applying a current to each pair of coils.
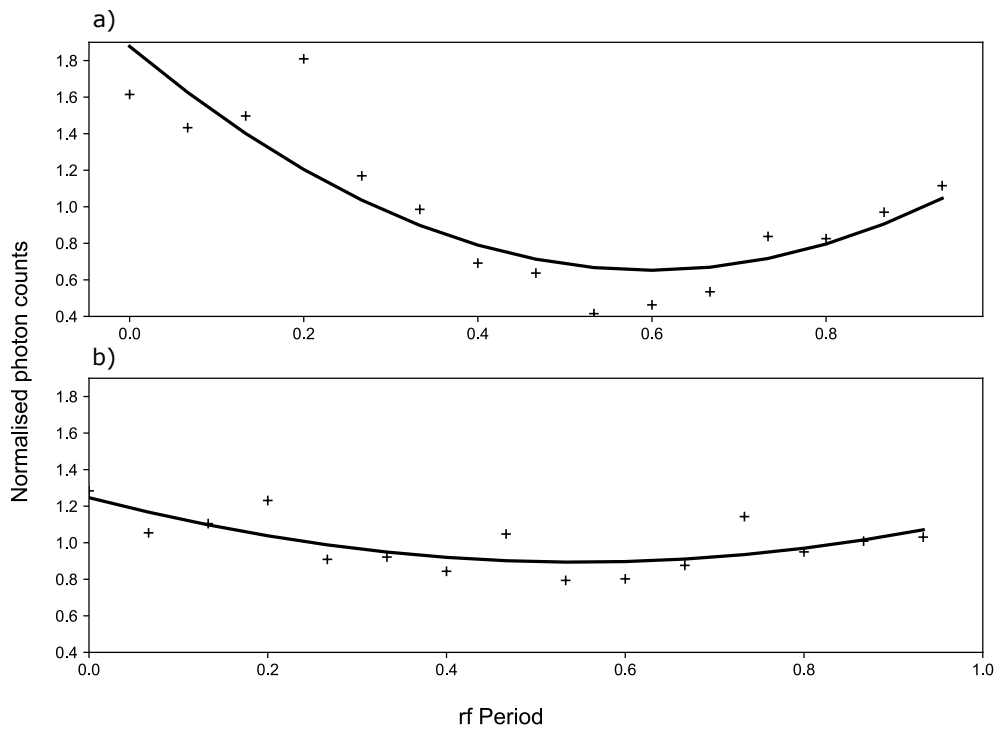
Figure 5.11: rf-correlation signal whose amplitude corresponds to the amplitude of micromotion when micromotion is compensated (a) poorly and (b) correctly.
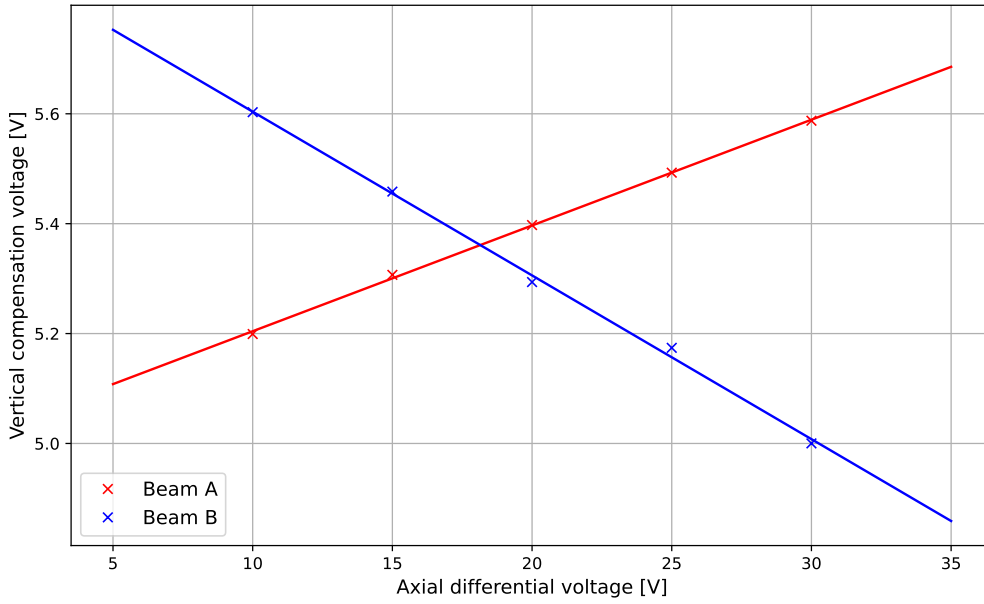
Figure 5.12: Vertical compensation voltage at which the amplitude of micromotion be-
comes the minimum for each different axial compensation voltage for two
interrogation directions. We select a set of compensation voltages at which
the two lines (blue and red) intersect. This set corresponds to the case
where micromotion in the two interrogation directions becomes minimised
simultaneously.

moves back and forth, the oscillatory motion induces a Doppler shift, leading to
oscillation of the fluorescence at Ω synchronised with the phase of the driving field,
as can be seen in Fig. 5.11.

Therefore, as we measure the fluorescence synchronised with the driving field, the
amplitude of the oscillation is proportional to the amplitude of the micromotion. We
need to minimise the amplitude of the micromotion. The micromotion is derived from
the mismatch between the null of the static and time-varying fields. As illustrated in
Fig. 2.7, a set of additional electrodes (C_x and C_y) near the trap electrodes allow
us to systematically move the null of the static field by applying static voltages to
corresponding compensation electrodes. Next, we need to find the appropriate set
of voltages that make the null of the static field coincide with the minimum of the
time-varying field. We measure the amplitude of the micromotion with a different
set of compensation voltages and find the set of compensation voltages that leads to
minimum of micromotion amplitude along the two direction simultaneously, which
corresponds to the intersection of two lines in Fig. 5.12
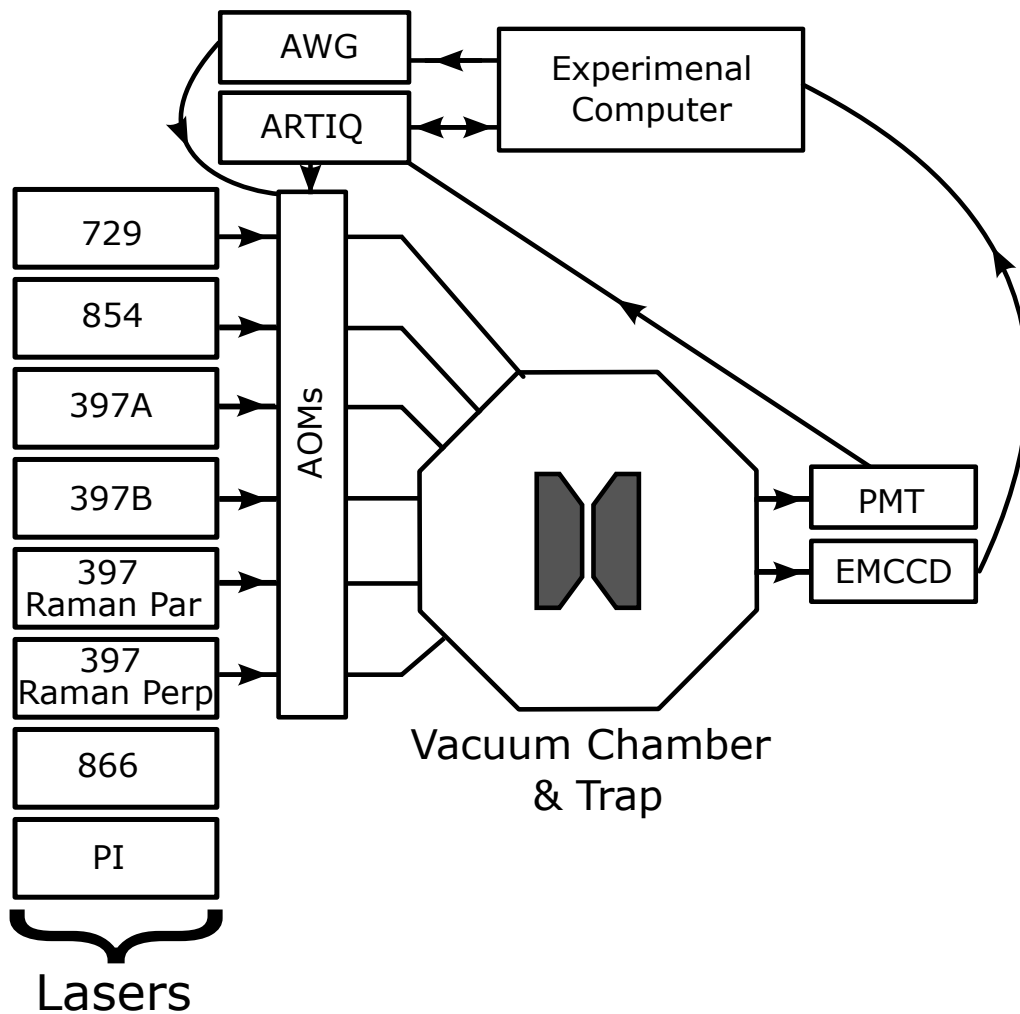
Figure 5.13: Overview of the control system. rf signals from ARTIQ and the arbitrary waveform generator (AWG) are sent to AOM modulators. Laser beams shown are indicative only.

5.6 Experimental Control

5.6.1 ARTIQ

We previously used a lab-built control system coded in visual C (details of the previous control system can be found in Ref. [60, 76]). However, as that control system limited the extension of pulse sequences to more complex ones, in the transition to the new trap, we adopted Advanced Real-Time Infrastructure for Quantum physics (ARTIQ) that is developed by M-Labs and the Ion Storage Group at NIST as a new control system.

ARTIQ runs on Python, a high-level programming language that makes it easy to describe complex experiments in a more intuitive way. The Python code is compiled and executed on dedicated hardware, including customised field-programmable gate arrays (FPGAs) and DDSs, with nanosecond timing resolution and sub-microsecond latency. ARTIQ also features a graphical user interface (GUI) that allows users to parametrise and schedule experiments. As ARTIQ is an open-source project, there is a large user community where we can easily get support[8].

5.6.2 Arbitrary Waveform Generator (AWG)

The realisation of quantum computation involves a sequence of laser pulses. A laser pulse with controllable pulse length and frequency is generated by sending a corresponding rf signal to an AOM that manipulates the power and frequency of the laser. The simplest form of the pulse used in our experiment is a square pulse with fixed frequency and amplitude. The square pulse can be generated by the DDS. However, as more complicated operations are required to give greater degrees of freedom in control of the qubit (i.e. pulse-shaping and multi-tone rf signal), it is necessary to generate a pulse with a more complicated pulse profile, which the DDS cannot generate. Hence, we adopt an AWG that, in principle, can be programmed by a user to generate such complicated pulse shapes and sequences.

5.6.3 Line Trigger

The ambient magnetic field fluctuates as much electrical equipment around the building, including air conditioners, experimental apparatus and lifts, produces a magnetic field uncontrollably. The main power lines dominate the other sources. To quantify the magnetic field variation due to the mains, we measure the carrier frequency of $S_{1/2,1/2} \leftrightarrow D_{1/2,1/2}$ in the standard Ramsey-type scan, but we put a delay with a variable length between the state-preparation and the spectroscopic

---

[8]ARTIQ user community in github
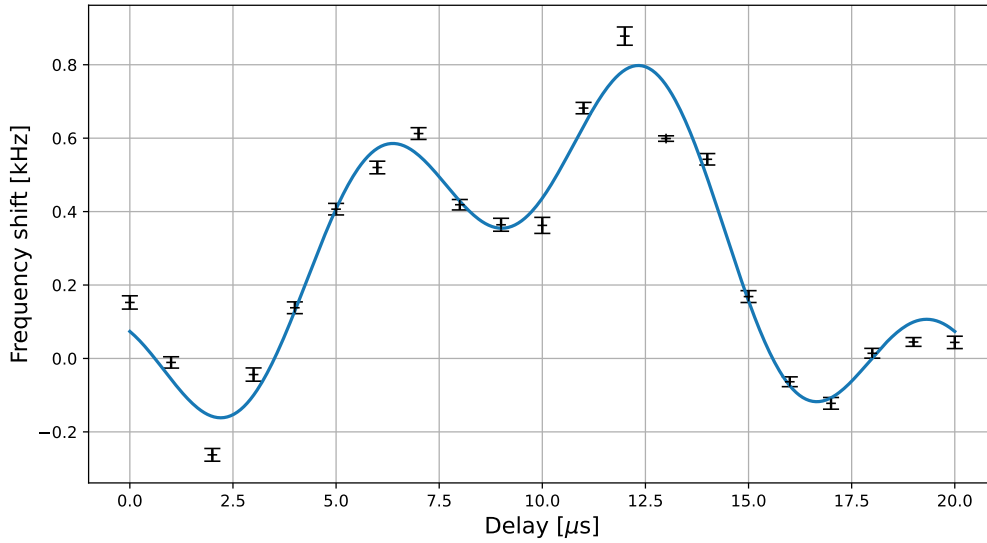
Figure 5.14: Carrier resonance frequency shift with the different line trigger delays. The fit (solid line), modelled as a sum of sinusoidal functions at 50, 100, and 150 kHz, suggests the amplitude of each frequency: 0.99, 0.14 and 0.6 μG

pulses. The carrier frequency is estimated by Bayesian inference because Bayesian inference allows for a much faster estimation of the carrier frequency (see Chapter 8 for a more detailed methodology of Bayesian inference). Fig. 5.14 illustrates how the carrier frequency varies with the length of the delay. We fit the measurements to a sum of oscillations at 50, 100, and 150 Hz. The fitting suggests the dominant components are 50 and 150 Hz, which are odd harmonics of 50 Hz. This variation is small enough that it is not strictly necessary to compensate for it, but it would be nice to be able to.

Magnetic field fluctuation leads to fluctuation of the resonance frequency of the qubit, resulting in faster dephasing between the qubit states. Therefore, we synchronise each shot of the experiment to the mains cycle at 50 Hz to ensure each shot starts at the same position of the mains cycle and minimise the magnetic field variation between shots. We use a line trigger that[9], produces a TTL signal synchronised to the main line: the line trigger generates a high TTL signal when the mains voltage is above zero and a low TTL signal otherwise. At the end of each shot of the experiment, the subsequent shot does not immediately begin but waits until the TTL signal is in the rising phase.

The line trigger limits the rate at which each experiment shot can be repeated to the maximum of 50 Hz; ideally the experiment should not need the line trigger. We added an additional pair of coils[10] that is aligned along the axis of the primary

---

[9]Ollie Corfield constructed an electrical circuit for the line trigger. The circuit diagram, available in his thesis[56]

[10]Two BSc students, Zeling Xiong and Zanxu Wang, built the compensation coils

coils to generate a magnetic field that counteracts magnetic field variation due to the mains. We use an Arduino microcontroller to generate the sinusoidal signal that is out of phase with the reference to the measured phase of the magnetic field variation at 50, 100, and 150 Hz in Fig. 5.14 so that the additional field can compensate for the laboratory magnetic field. We have observed the effect of the additional coils, but this magnetic field compensation does not entirely cancel the field. Lack of time prevented proper calibration of the compensation coils and testing of the Arduino, which generates compensating signal, as we implemented the coils and the system one month before I left the laboratory.

Chapter 6

729 nm Laser

Our experiment employs several lasers at different wavelengths for different purposes. Among the lasers used in our experiment, a laser at 729 nm has the most stringent frequency and power stability requirements because this laser drives a narrow-linewidth quadrupole transition $S_{1/2} \leftrightarrow D_{5/2}$ for a coherent operation on the ion.

In preparing the experimental apparatus for the new trap, I was primarily responsible for the initialisation of a new 729 nm diode laser that replaced the original lab-made one. During the first year of my PhD, I upgraded the 729 nm laser system, including the diode laser, the electronics-associated proportional-integral-derivative (PID) controller for frequency stabilisation, and a tapered amplifier (TA): I replaced the original lab-made 729 nm diode laser, PID electronics and TA with commercial devices. Those upgrades provided a much more stable 729 nm laser beam with more optical power available at the trap.

6.1 Pound—Drever—Hall (PDH) Locking

The lasers (at 397, 423, 854 and 866 nm) that drive dipole transitions for photoionisation, Doppler cooling and re-pumping are locked to a wavemeter, and this method results in roughly 1 MHz laser frequency stability. This 1 MHz frequency stability is sufficiently low to controllably drive those dipole transitions, whose linewidth is typically tens of MHz. However, the main spectroscopic laser at 729 nm requires a sub-kHz linewidth as the atomic state and associated motional states of the ion are coherently manipulated via the narrow-linewidth quadrupole transition. Hence, we adopt Pound—Drever—Hall (PDH) techniques to stabilise the frequency of the laser with the use of a high finesse cavity with $\mathcal{F} \approx 60000$[1] to the sub-kHz level[86, 87].

---

[1] The finesse of the cavity was measured almost ten years ago. The raw data are available in Ref.[85]

63
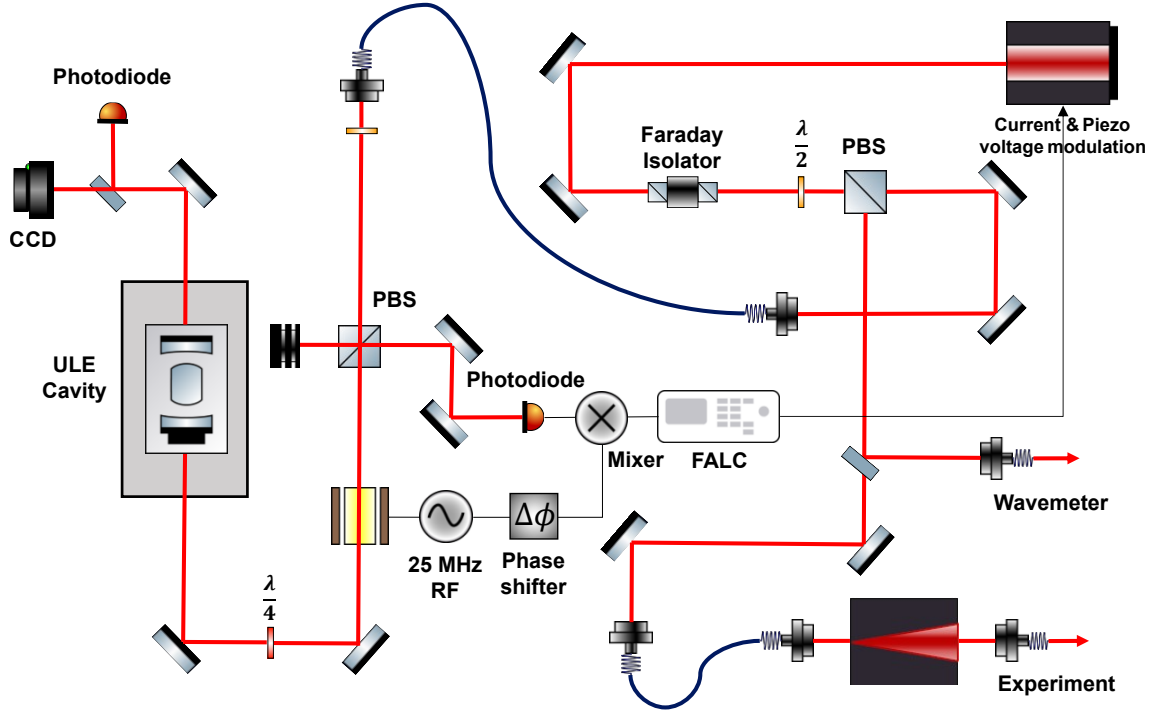
Figure 6.1: Overview of a 729 nm laser system, including the PDH locking comprising optical and electrical elements and TA, which amplifies the power of the laser. The red solid line represents the beam path of the 729 nm laser, whereas the black line shows flow of the electrical signal.

6.1.1 Theory
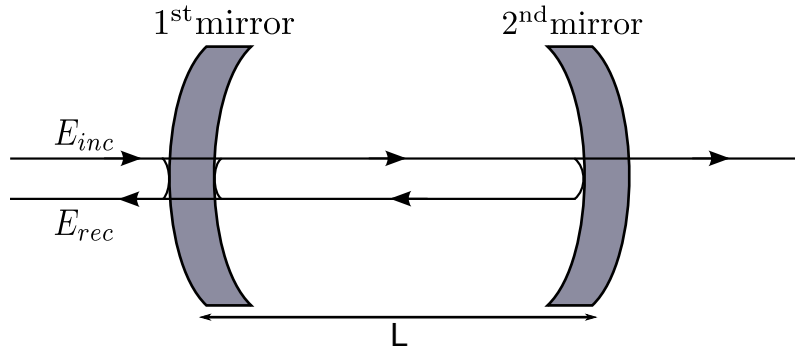
Figure 6.2: Schematic diagram of the Fabry–Perot cavity. The total reflected beam is the coherent sum of two beams: the beam promptly reflected by the first mirror and the other beam leaking from the cavity after bouncing back and forth within the cavity.

We start with the properties of a Fabry–Perot cavity, which is simply formed by a pair of symmetric mirrors with high reflectivity r. We here consider monochromatic light, whose electric field can be expressed as

$$E_{inc}(t) = E_0 e^{i\omega t}. \tag{6.1}$$

As illustrated in Fig. 6.2, when the light is launched into the Fabry–Perot cavity, a

fraction of the light is reflected from the mirror the light is first incident on, but some of the light is transmitted through the first mirror, reflected back and forth between the two mirrors and eventually leaks through the first and second mirrors (i.e. out of the cavity). The beam promptly reflected by the first mirror has a phase shift of π, and the leakage beams acquire an integer multiple of the phase accumulation of the light in one round trip inside the cavity $2\omega L/c$. The total reflected light is a sum of all reflected beams from the mirrors and the cavity:

$$
\begin{aligned}
E_{ref} &= E_0 \left[re^{i(\omega t+\pi)} + trte^{i(\omega t-2\omega L/c)} + tr^3te^{i(\omega t-4\omega L/c)} + \cdots \right] \\
&= E_0 \left[re^{i(\omega t+\pi)} + \sum_{n=1}^{\infty} t^2 r^{2n-1} e^{i(\omega t-\frac{\omega}{\Delta_{FSR}})} \right]
\end{aligned}
\tag{6.2}
$$

where $t = \sqrt{1-r^2}$ is the transmissivity of the mirrors, and $\Delta_{FSR} = c/2L$ is the free spectral range of the cavity, which is the frequency spacing between the resonances. The terms in the summation in Eqn. 6.2 represent a geometric series, so the infinite sum can be simplified. We can obtain a reflection coefficient F, which is the ratio of the amplitude of the reflected light to that of the incident light, in the following form:

$$
F(\omega) = \frac{E_{ref}}{E_{inc}} = \frac{r(e^{i\omega/\Delta_{FSR}} - 1)}{1 - r^2 e^{i\omega/\Delta_{FSR}}}.
\tag{6.3}
$$

Fig. 6.3 shows a resonant dip, indicating no light is reflected on resonance, and $F(\omega)$ varies depending on the frequency of the beam. The spectral shape of $F(\omega)$ is symmetric around the resonance, so the reflected light from the cavity cannot be used as an error signal for the feedback loop because $F(\omega)$ cannot tell which side the of the resonance the frequency of the light currently lies on.

We modulate the phase of the light described in Eqn. 6.1 by $\beta\sin(\omega t)$ where β and ω_m are modulation depth and frequency, respectively[2]:

$$
E_{inc}(t) = E_{inc}e^{i(\omega t+\beta\sin\Omega t)}.
\tag{6.4}
$$

Eqn. 6.4 is re-written using a Bessel function of the first kind $J_n(\beta)$:

$$
E_{inc}(t) = E_{inc}e^{i\omega t} \sum_{n=-\infty}^{\infty} J_n(\beta)e^{in\omega t}
\tag{6.5}
$$

where the resulting electric field contains multiple frequency components (the carrier and the sidebands), and the strength of each component is given by $J_n(\beta)$. If $\beta < 2$,

---

[2]In our experiment, phase modulation is achieved by an electro-optic modulator (EOM). An EOM has a crystal that rapidly changes its refractive index in response to the electrical signal applied to it, and it works much like a variable waveplate.
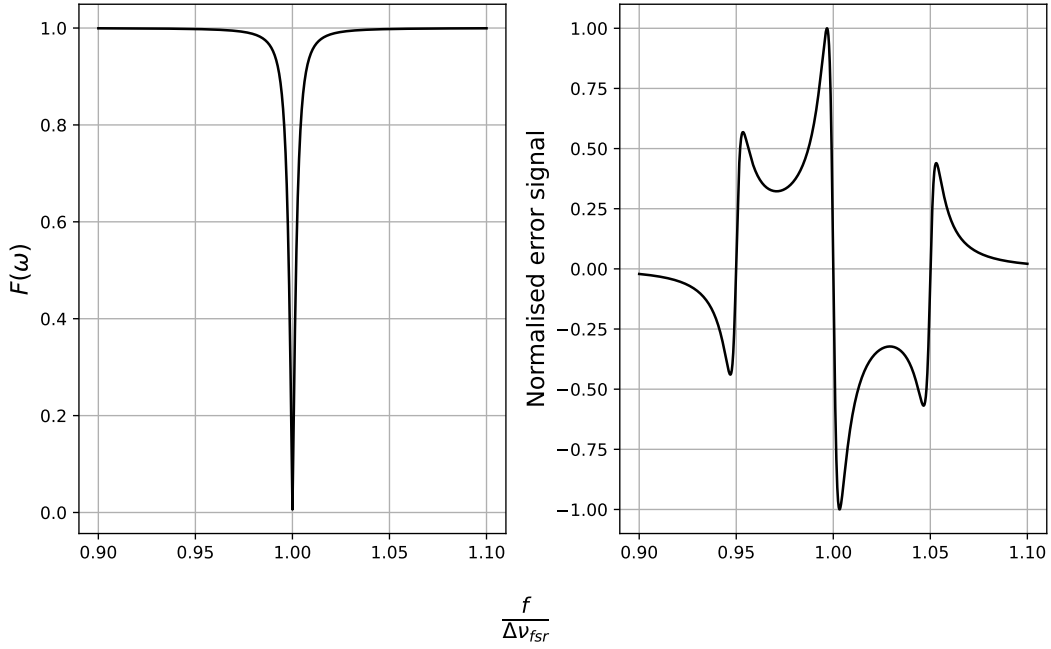
Figure 6.3: Left: Reflectivity coefficient $F(\omega)$ of the Fabry–Perot cavity. Right: the PDH error signal

then the carrier and the first-order sideband dominate:

$$E_{inc}(r,t) \approx E_{inc}(r)[J_0(\beta)e^{i\omega t} + J_1\beta e^{i(\omega+\Omega)t} - J_1(\beta)e^{i(\omega-\Omega)t}] \tag{6.6}$$

Plugging Eqn. 6.6 into Eqn. 6.3 yields

$$E_{ref}(t) \approx E_{inc}(r)[F(\omega)J_0 e^{i\omega t} + F(\omega+\Omega)J_1 e^{i(\omega+\Omega)t} - F(\omega-\Omega)J_1 e^{i(\omega-\Omega)t}]. \tag{6.7}$$

A photodiode cannot directly measure the amplitude of electric field, but the intensity of the light $P_{ref} = |E_{ref}|^2$; the generated photo-current is proportional to the intensity. After doing some algebra using Euler's formula, the photo-current of the reflected light is obtained:

$$
\begin{aligned}
P_{ref} =& P_c|F(\omega)|^2 + P_s\{|F(\omega+\Omega)|^2 + |F(\omega-\Omega)|^2\} \\
&+ 2\sqrt{P_c P_s}\{\mathrm{Re}[F(\omega)F^*(\omega+\Omega) - F^*(\omega)F(\omega-\Omega)]\cos\Omega t \\
&+ \mathrm{Im}[F(\omega)F^*(\omega+\Omega) - F^*(\omega)F(\omega-\Omega)]\sin\Omega t\} \\
&+ 2\Omega \text{ terms}
\end{aligned}
\tag{6.8}
$$

where P_c and P_s are the power of the carrier and the first-order sidebands, respectively. The reflected power includes several oscillating terms at three different frequencies: a DC power from the carrier, two components at the modulation frequency Ω, and

66

lastly, higher-order components derived from the inference between the sidebands. We pull out the term in front of $\sin(\Omega t)$, which contains the phase information, by mixing the P_{ref} with the modulation signal followed by the low pass filter, which filters out any oscillatory signal. The error signal is given as

$$\epsilon = 2\sqrt{P_c Ps}\,\text{Im}[F(\omega)F^*(\omega + \Omega) - F^*(\omega)F(\omega - \Omega)] \tag{6.9}$$

The right panel of Fig. 6.3 shows an example of the error signal. In contrast to the spectral shape $F(\Omega)$ of the Fabry–Perot cavity (see left panel of Fig. 6.3), the error signal is asymmetric near the resonance. If the modulation frequency is sufficiently big, then the sideband is far from the resonance. The sidebands will be totally reflected (i.e. $F(\omega \pm \Omega) = -1$), and the error signal become proportional to $\text{Im}[F(\omega)]$. If the laser is close to the resonance, the reflection coefficient $F(\omega)$ can be approximated to [88]

$$\text{Im}[F(\omega)] \approx \frac{1}{\pi}\frac{\delta\omega}{\delta\mu}, \tag{6.10}$$

where $\delta\omega$ is detuning from the resonance, and $\delta\mu$ is the cavity linewidth. The error signal ϵ in Eqn. 6.9 can be re-written as

$$\epsilon \approx \frac{4}{\pi}\sqrt{P_c P_s}\frac{\delta\omega}{\delta\mu} = D\delta f \tag{6.11}$$

where $D = \frac{8\sqrt{P_c P_s}}{\delta\mu}$ is proportionality. The error signal near resonance becomes a linear function, and the proportionality D can be maximised when $P_c = P_s$.

6.1.2   High-finesse Cavity

The optical cavity serves as a frequency standard and is used to produce the error signal for the PID feedback loop; the achievable minimum laser linewidth through the PDH technique is strongly dependent on the finesse of the cavity. Our cavity was constructed almost ten years ago, and thermal and optical properties were measured previously. The relevant measurement results can be found in Ref. [60]. It is essential to characterise our cavity. The high finesse cavity was constructed before I joined the group, and the characterisation had been done, and the detailed experimental results can be found in Ref. [60]. I replaced the old lab-made diode laser with a commercial diode laser and modified the layout of optical elements for mode-matching. Thus, here I will give a summary of what I have done.

Mode-matching

As we replaced the original lab-made 729 nm diode with the new commercial one, we modified the optical layout to more efficiently use the space of the optical table.
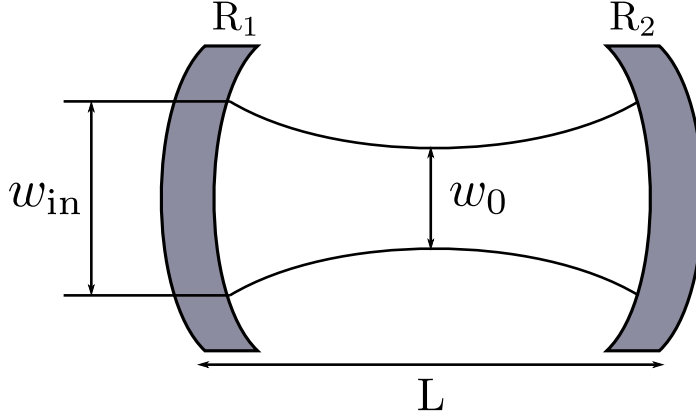
Figure 6.4: Gaussian beam in an optical cavity. If the mode-matching condition is met, the beam traces itself while it is reflected back and forth by the mirrors.

We also reoptimised the coupling of the laser to the cavity such that the spatial distribution of the input Gaussian beam matches the spatial mode of the cavity, which is known as mode-matching. Mode-matching is important as a poorly matched beam causes a loss of the beam power in the cavity, and the reflected beam contains many different modes, which results in instability of the PDH locking.

The physical dimensions of the cavity and properties of the mirrors (curvature of mirrors R and cavity length L) are available in Ref. [60]; we can calculate the required beam waist of the incident beam onto the cavity. Our cavity is symmetric (i.e. $R_1 = R_2 = R$), so the waist should be positioned at the midway of the cavity. The waist of the fundamental mode of the cavity w_0 is given as

$$w_0^2 = \frac{L\lambda}{\pi} \sqrt{\frac{g_2}{g_1(1 - g_1 g_2)}}, \tag{6.12}$$

where

$$g_1 = 1 - L/R_1 \text{ and } g_2 = 1 - L/R_2. \tag{6.13}$$

A goal of optical system design is to make the collimated beam from the optical fibre focus at the midway of the cavity with the beam waist equal to w_0 of the cavity, which is calculated above.

Mode Consideration

The fundamental mode of the cavity TEM_{00} (see Fig. 6.5) is preferable because higher-order modes actually contain two or more modes with approximately the same frequency, and this degeneracy is not shown in the fundamental mode. Therefore, coupling to the fundamental mode results in the strongest locking signal, and the locking is stable because there are no other modes nearby. However, we previously used the TEM_{03} mode of the cavity when we operated the Penning trap. TEM_{03} is
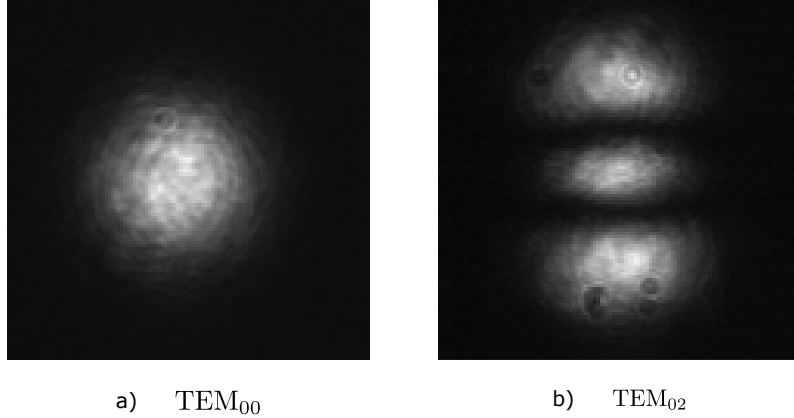
a)   TEM$_{00}$ b)   TEM$_{02}$

Figure 6.5: Images of different spatial modes of Gaussian beam taken by a camera behind the cavity. a) TEM$_{00}$. b) TEM$_{03}$.

the only mode whose frequency was close enough to the atomic resonance frequency of the S$_{1/2}$ ↔ D$_{5/2}$ transition of ^{40}Ca$^+$ within an adjustable frequency range of the AOM (200 MHz). The atomic resonance frequency is significantly reduced in the new trap because a Paul trap does not require as strong a magnetic field as a Penning trap. There exists a fundamental mode whose frequency is only roughly 193 MHz different from the atomic resonance, which is within the range of the AOM bandwidth; thus, we use the fundamental mode.

Thermal Properties

Eqn. 6.3 suggests the cavity resonance frequency to which the laser is locked is determined by the spacing between the two mirrors in the cavity. The cavity spacing drifts over time due to the thermal expansion of the mirrors, leading to the drift of the cavity resonance frequency. Hence, the mirrors of our cavity are made of low-expansion material to minimise the thermal effect on the resonance [60]. However, we have still observed that the resonance frequency drifts in the short term (see Fig. 6.6 for the drift during the day) and in the long term (see Fig. 6.7 for day-to-day drift).

The short-term drift is more problematic because some experiments last a few 10s of minutes, and the time scale of the drift can be comparable to that of the experiment; the frequency of the laser may significantly drift during a single experiment. This drift during the day is due to residual thermal expansion of the cavity because the cavity temperature is not close enough to the point at which the expansion coefficient is zero. We remeasured the zero-crossing temperature T_{zc} of the cavity, and the fit in Fig. 6.6 gives $T_{zc} = 12.6\,°C$, which is inconsistent with the previous measurement of $17.4\,°C$ from Ref.[60]. As we set the temperature of the cavity to the newly measured T_{zc}, the rate of short-term drift is significantly reduced. The long-term drift, however, is considered to be a result of the ageing of the cavity [60]. This long-term drift
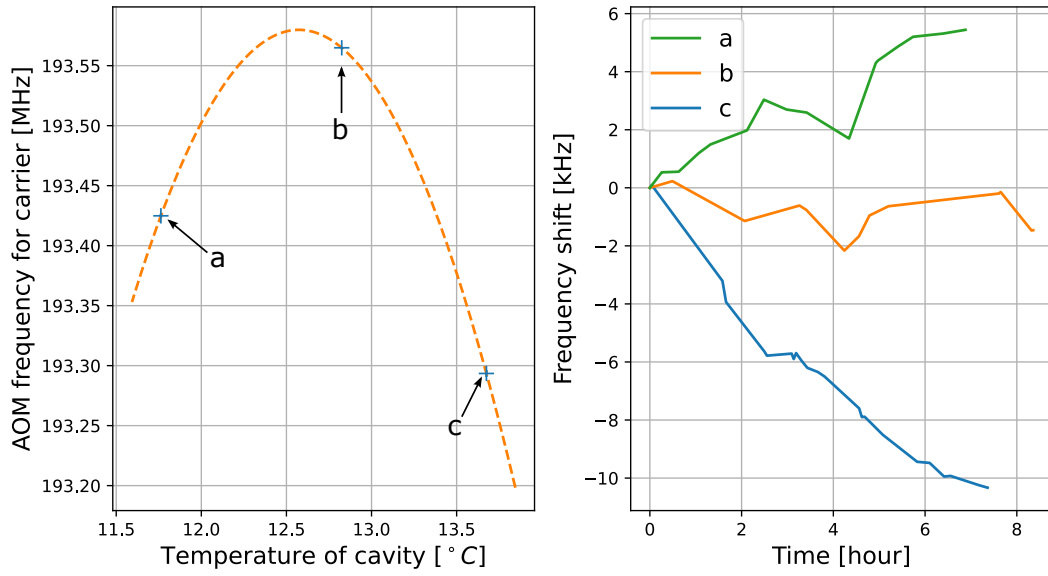
Figure 6.6: Left: the measured carrier frequency as a function of the temperature of the cavity. The temperature of the cavity is estimated by a set voltage to a thermistor to which the temperature stabiliser is locked. The conversion factor between the set voltage and the temperature was measured previously [60]. The fit suggests the zero-crossing temperature $T_{zc} = 12.6\,°\mathrm{C}$, at which the thermal expansion of the cavity becomes zero. Right: the drift of the carrier frequency with the cavity temperature is locked to different target temperatures shown in the figure on the left.
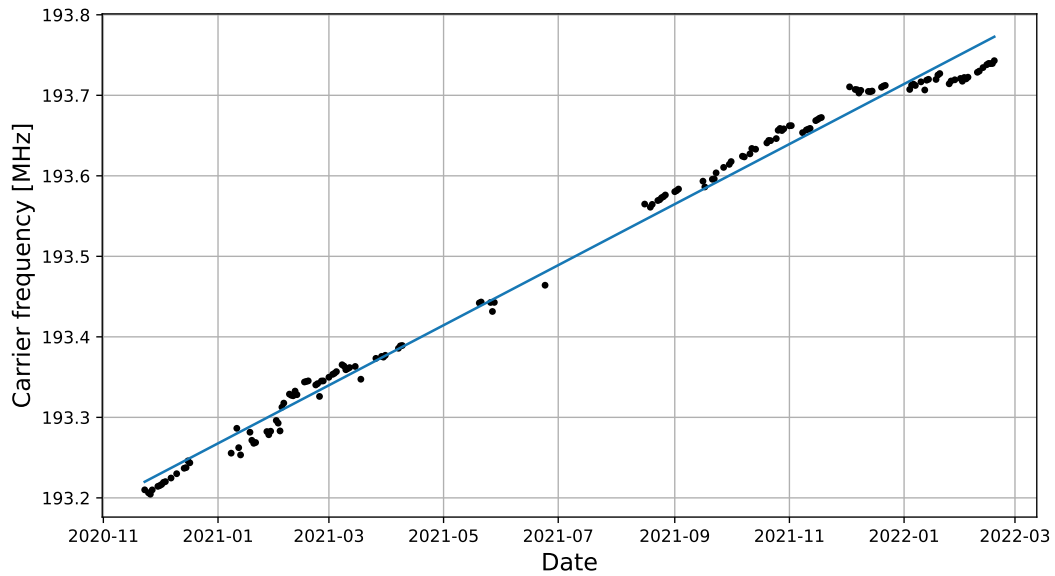
Figure 6.7: Daily drift of the carrier frequency. The carrier frequency drifts at the rate of $1.2(2)\,\mathrm{kHz/day}$. This rate is comparable to the rate previously measured in the Penning trap $(1.45\,\mathrm{kHz/day})$ [75].

70

also has been observed since the first use of the cavity, and the day-to-day drift rate measured in Fig. 6.7 agrees with the value previously measured.

Leakage in the cavity
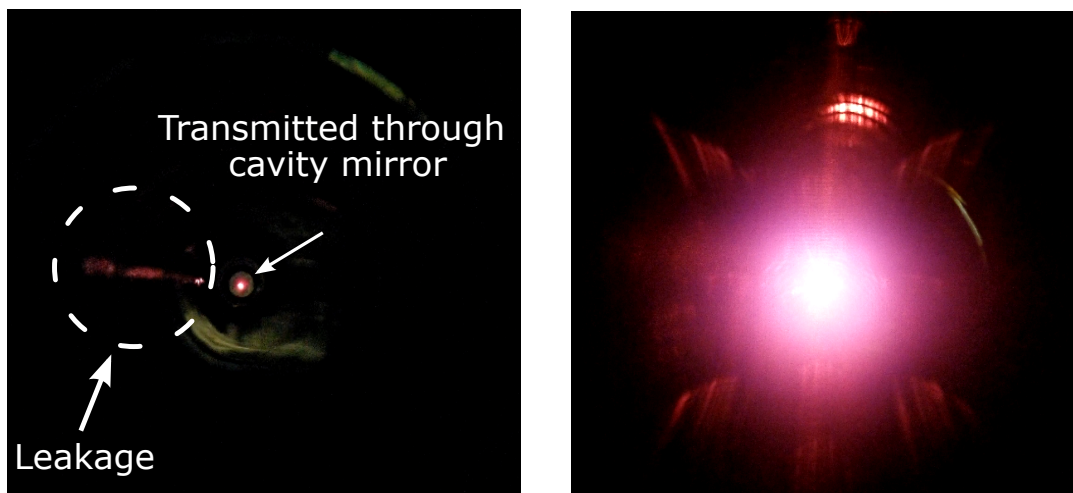
Figure 6.8: Images of the beam behind the cavity. Left: the bright dot in the middle shows the beam going through the mirrors. Right: Image taken by moving the camera to the left and focusing on the leakage beam. The leakage beam looks much brighter than the beam through the mirrors.

We have observed power leakage from the cavity (see Fig. 6.8). The cause of the leakage is still unknown. This may account for the relatively low power of the reflected beam compared with the power of the incident beam: in principle, all of the beam's power should be reflected on the resonance. Fortunately, we do not see any distortion of the error signal generated by the reflected beam or evidence that the leakage affects the performance of the PDH locking. However, the leakage increases the minimum required amount of light sent to the cavity. This might be problematic if we do not have enough power sent to the TA. We split the beam using the PBS: one of the beams is sent to the cavity, and the other goes to the TA. If you have to send much more power to the cavity, then the power of the beam to the TA has to be reduced. However, the power of input to the TA has to be at least 10 mw, as low power may cause permanent damage to the TA due to amplified spontaneous emission.

6.1.3 Servo Bump

Although the control system is meant to suppress the noise injected into the system, if the phase delay of the feedback signal is greater than π, then the control system acts as a source of positive feedback (i.e. the control system amplifies the noise instead of suppressing it). There are two ways to measure the servo bump: (i) measure the error
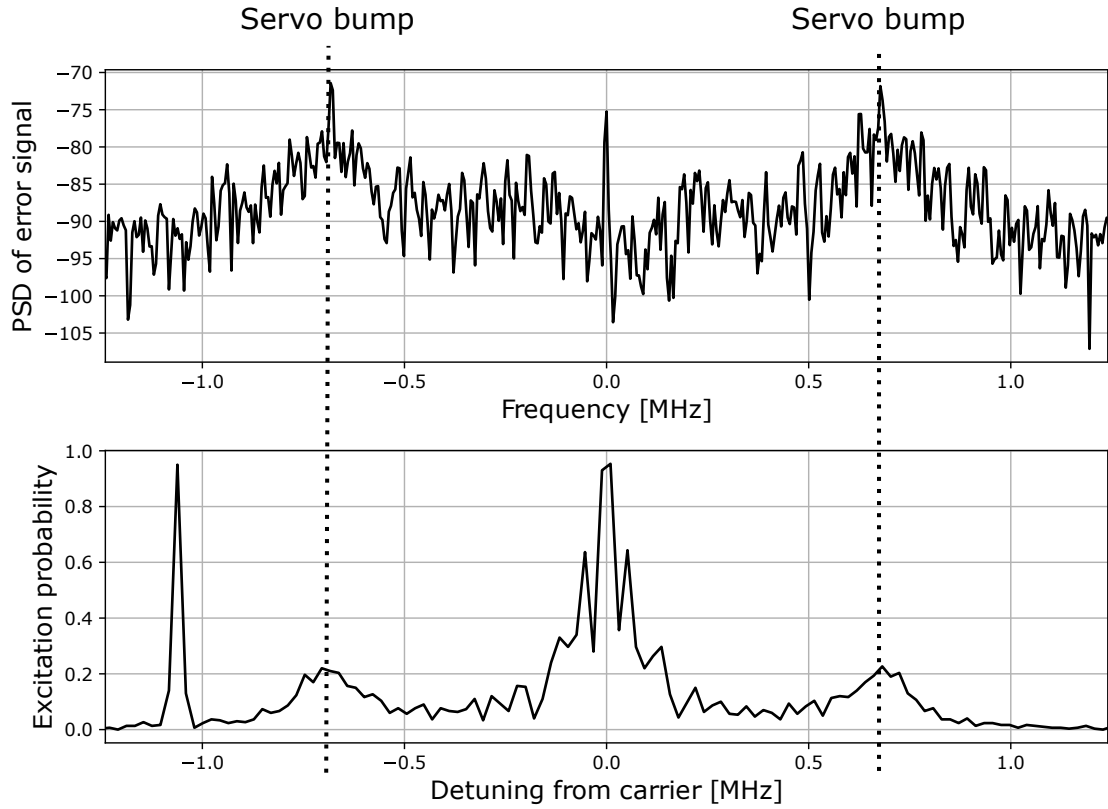
Figure 6.9: Measurement of the servo bump. Top: power spectrum of the error signal, Bottom: carrier and sideband spectrum with the sideband cooled ion. The spectrum shows two peaks in addition to the strong carrier and blue sideband resonance peaks, and these additional peaks are results of the servo bump. The servo bump peaks indicated in the two figures are aligned because both are attributed to the servo bump.
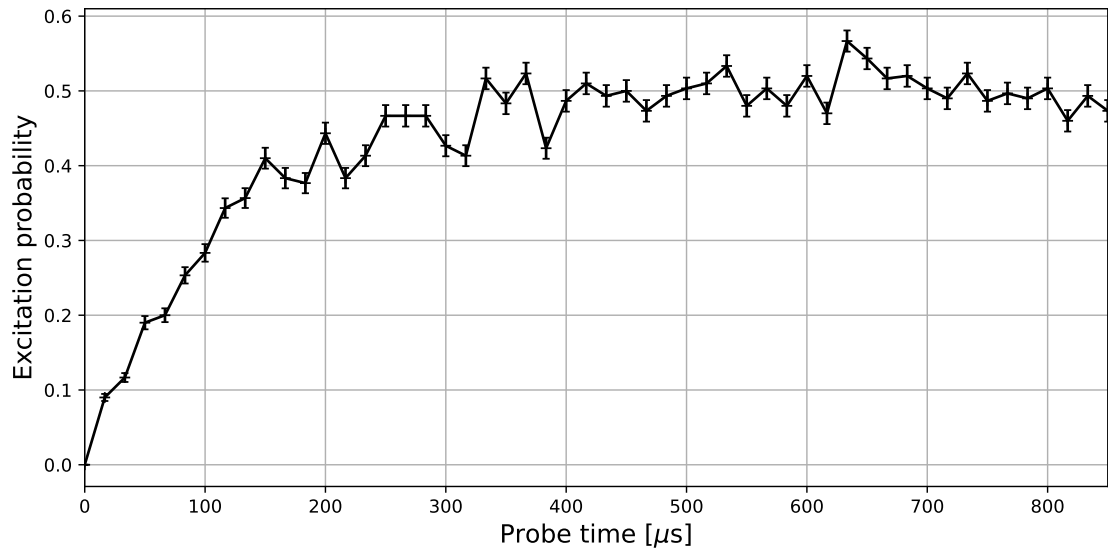
Figure 6.10: Time evolution of the ion initially prepared in $|g, 0\rangle$ while the ion is interrogated by the laser tuned near to the frequency of the servo bump. The population is rapidly equalised, indicating the laser incoherently interacts with the ion and causes rapid decoherence.
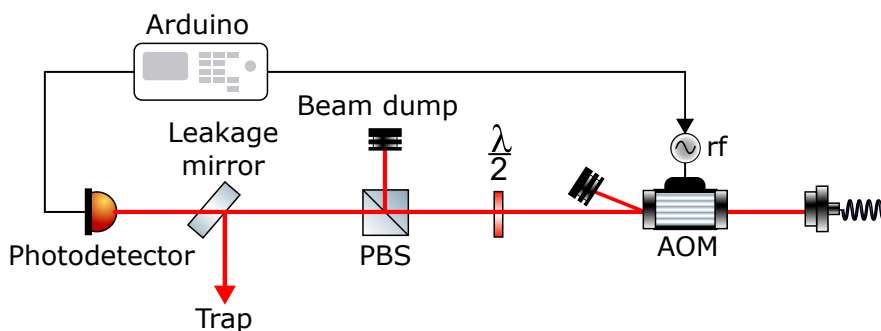
Figure 6.11: Schematic diagram of the optical setups and the associated electronics for the noise eater. A photodetector measures the power of the 729 nm laser transmitted through the AOM (0th order) and sends the resulting signal to the Arduino. Then, the Arduino reads the measurement and calculates the control signal that modulates the rf amplitude to the AOM to control the power of the transmitted beam by the AOM (0th order).

signal and (ii) measure the atomic spectrum. The top of Fig. 6.9 shows the power spectrum of the error signal with servo peaks at $\approx \pm 675$ kHz from the modulation frequency (25 MHz). The position and the height of the servo bump, which quantify the strength of the servo bump, vary depending on the PID feedback parameters, which are set by the FALC, a loop filter from Toptica; the aim of optimising the control system is to minimise the strength of the servo bump and move its frequency as far from the spectral frequencies of $^{40}\text{Ca}^+$ (carrier and sideband) as possible so that the servo bump frequency does not overlap with the frequency of any sidebands or carrier transitions. The servo bump causes phase modulation of the laser field, leading to a sideband at the servo bump frequency. However, the sideband of the laser due to the servo bump does not have a definite frequency but is an incoherent mixture of many different frequencies around the servo bump frequency. As shown in Fig. 6.10, the excitation probability quickly converges to one half because the sideband of the laser at the servo bump frequency drives the ion incoherently. Thus, if the servo bump frequency is close to the motional frequency, then it can drive the sideband transitions incoherently, causing decoherence. Fig. 6.10 illustrates the sideband by the servo bump driving the transition incoherently: the figure shows no oscillatory signal but quickly converges to 0.5.

6.2 Noise Eater

If the laser is freely running, its power drifts over time due to the thermal drift of the laser diode and the polarisation fluctuation of the laser, which affects the coupling efficiency of the laser to the optical fibre. The drift makes the Rabi frequency time-dependent and hinders coherent operations on a trapped ion. Therefore, we devise a
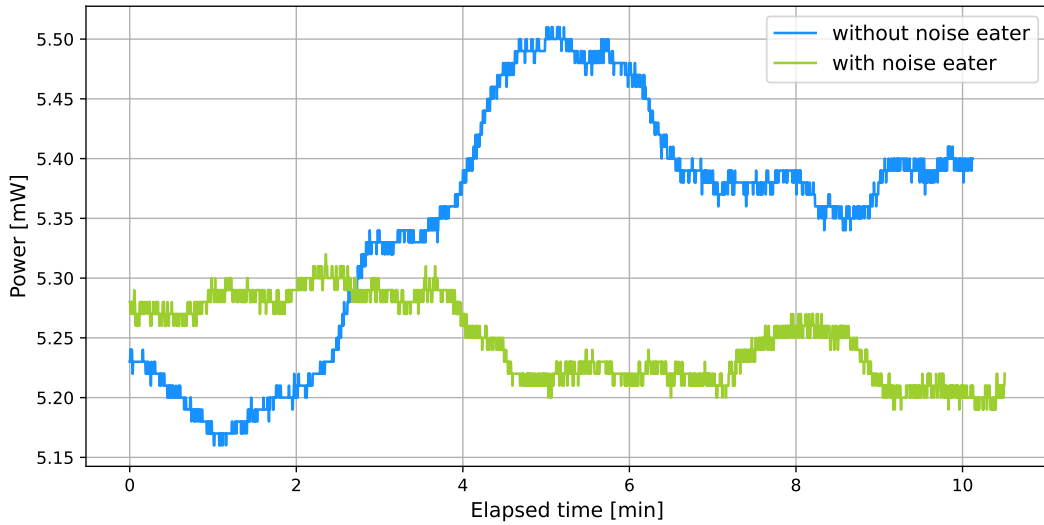
Figure 6.12: Power drift of a 729 nm laser beam over 10 minutes with and without the noise eater. The noise eater helps the power of the laser fluctuate less.

noise eater that stabilises the power of the laser using a PID feedback control. Fig. 6.11 illustrates the schematic of the optical setup for the noise eater. The laser first goes through the AOM crystal, a fraction of the transmitted beam goes through the leakage mirror, and most of the beam is reflected. A photodiode behind that mirror measures the power of the transmitted beam whose fluctuation is correlated to the power of the reflected beam, which is sent to the trap. An electric signal produced by the photodiode, which is proportional to the power of the transmitted beam, is an indirect measure of laser power to the trap. The signal from the photodiode is sent to the Arduino microcontroller, and the Arduino calculates an error signal $V_{\mathrm{err}} = V_{\mathrm{measured}} - V_{\mathrm{target}}$. The Arduino is programmed to generate a feedback signal following a standard PID algorithm, and the feedback signal is sent to a voltage modulator for the AOM. The PID controller modulates the power of the beam going into the zeroth order of the diffraction. This transmitted beam is directed onto the secondary AOM, which manipulates the frequency of the beam, and sent to the trap.

One advantage of using the Arduino is that PID parameters are easily tuned by reprogramming the controller. Different PID parameters have been tested and optimised such that the controller's response time is as short as 1 ms, and the averaged deviation of the power during 20 min is less than 1% of the total input power.

To see the effect of the noise eater, we track the power of the beam after the last fibre coupler, which is immediately before the trap, for 10 minutes. Fig. 6.12 shows the comparison of the power drift with and without the noise eater, and the figure suggests the noise eater can reduce the power fluctuation from 1.9 % to 0.5 %. This is not a significant improvement tough.

74

6.3 Tapered Amplifier

The primary spectroscopic laser at 729 nm is located next to the room where all the other lasers and the vacuum chamber are located because the 729 nm laser is placed on a separate optical table for better acoustic isolation. There was no room for the cavity and PDH electronics on the main optical table, on which the trap is located, when I set up the new 729 nm laser[3]. Therefore, the 729 nm laser is delivered to the trap through the 5 m of room-to-room optical fibre. The optical power of the laser is significantly reduced because the laser is coupled to and transmitted through the long room-to-room optical fibre and the many optical elements on the beam path. To keep the power of the beam at the trap centre as high as is required for the experiment, we must amplify the power of the beam and use a TA for power amplification.

We previously used a lab-made TA[4]. However, the amplification of the TA has gradually reduced as the TA ages, and the output power of the TA significantly drifts during the day due to the thermal effect, making the Rabi frequency of the laser time-dependent. We decided to buy a new commercial TA and replaced the old TA with the commercial one[5].

---

[3]As we no longer operate the Penning trap, we can remove some optical elements for the Penning trap. Because there is now space for the 729 nm laser, we plan to transport the 729 nm laser onto the main optical table. This move would eliminate the need for 5 m of optical fibre, through which noise can be injected.

[4]The original TA was designed and constructed by Joseph Goodwin, a previous PhD student. The physical dimension and details of associated electronics, such as a temperature stabiliser and safety circuit, can be found in his PhD thesis [60]

[5]MOGlabs MOAL-002

Chapter 7

Coherent Control of a Single Ion

Suppose we wish to use a trapped ion as a qubit and utilize this qubit for quantum computation and quantum simulation. We must first be able to control the quantum state of the ion coherently. The quantum system realised by a trapped ion comprises an atomic state defined by the atomic structure of the ion and a motional state driven by the trapping potentials. Complete control of the trapped ion involves the coherent manipulation of the motional states and the atomic state of the ion, and those two degrees of freedom can be coupled and coherently manipulated through the carrier and sideband transitions [89, 90].

Deterministically engineering an arbitrary quantum state is a long-lasting goal in quantum information science [91]. In theory, we can prepare any states we want from any well-defined initial state, which is typically $|g, n = 0\rangle$ in our experiment, using a combination of the carrier and sideband transitions [92, 93, 94]. However, there are many aspects where the dynamics we can drive in practice differ from the theoretically available interactions. For example, if we consider the perfect two-level system, then we can ignore off-resonant interactions. However, the atomic energy structure of the ion involves many other levels, and the motional states of the ion consist of an infinite set of discrete levels. In many cases, we ignore those interactions with the use of approximations (e.g. rotating wave approximation). However, the off-resonant coupling of the light field to those additional levels, which we wish to ignore, results in unwanted effects, hampering the coherent control of the trapped-ion qubit [95, 30]. We must consider those off-resonant effects when realising single and two-qubit gates with high fidelity.

This chapter aims to address off-resonant effects: off-resonant excitation and AC Stark shift. We numerically study the effect of off-resonant excitation and discuss how this excitation can be significantly suppressed by shaping the driving pulse. We measure the AC Stark shift due to off-resonant coupling to the carrier when we drive the first-order sideband and attempt to compensate for the frequency shift by applying a compensation pulse, which is simply an additional pulse that produces

another AC Stark shift to balance the shift by the off-resonant carrier. We prepare the superposition of multiple motional Fock state $|n\rangle$ using only the carrier and the first-order sideband transitions with AC Stark shift compensation applied. With the prepared motional superposition state, we perform Ramsey interferometry to infer the quantum coherence stored in the motional states by observing the inference pattern the state exhibits.

7.1 Off-resonant Coupling

When we drive the carrier or sideband transitions, it is impossible to address exclusively carrier or sideband transitions; for instance, when we address the first-order red sideband, we simultaneously drive the carrier and blue sideband transitions off-resonantly. There are two possible effects due to the off-resonant coupling: off-resonant excitation and AC Stark shift. In this section, we attempt to evaluate the errors caused by the undesirable off-resonant effects and present the methods used to counteract them.

We expect the magnitude of the off-resonant effect to scale as Ω^2/δ^2, where δ is the detuning with respect to the resonance of the transition under consideration, and Ω is the Rabi frequency of the driving field. Assuming that the ion is in the Lamb-Dicke regime, the Rabi frequency of the sideband is much weaker than that of the carrier. Thus, when we drive the carrier transition, the off-resonant coupling to each sideband does not significantly affect the dynamics induced by the carrier; the off-resonant coupling is ignored. However, when we drive the sideband transition, the off-resonant carrier is relatively strong, and we cannot ignore it – we mainly focus on the adverse effects of the off-resonant carrier when driving the sideband transition .

7.1.1 Off-resonant Excitation

If the detuning δ of the off-resonant interaction is sufficiently large compared to the Rabi frequency, $\delta \gg \Omega$, then the off-resonant coupling does not induce any significant population transfer between the states, but in certain circumstances, the dynamics due to unwanted off-resonant coupling cannot be completely neglected. Fig. 7.1 shows a numerical simulation of Rabi oscillation on the blue sideband with the off-resonant coupling excluded and included in solving the relevant optical Bloch equations. If we completely neglect the off-resonant interaction, the pulse induces a complete π rotation, transferring $|g\rangle$ to $|e\rangle$. However, if the off-resonant interaction is present, the fast oscillation at approximately the trap frequency ω_z occurs in addition to the smooth transition from $|g\rangle$ to $|e\rangle$. If the pulse time is an integer multiple of the off-resonant carrier period $\approx \frac{2\pi}{\omega_z}$, then the off-resonant excitation results in no
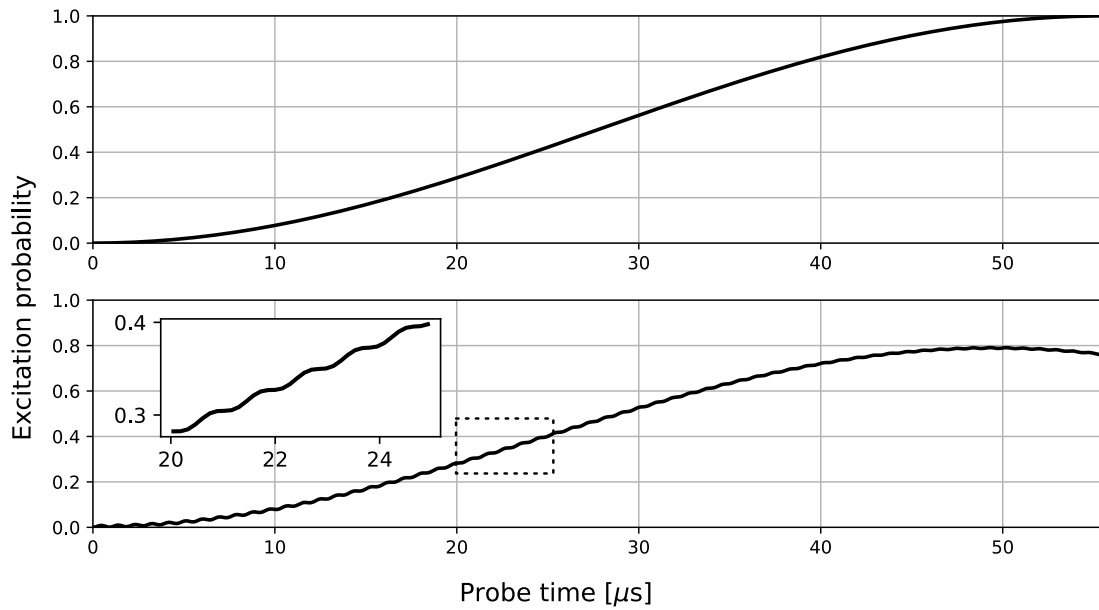
Figure 7.1: Time evolution of initially prepared $|g, 0\rangle$ state while the blue sideband is driven. Corresponding carrier Rabi frequency Ω_C is $80\,\text{kHz}$, and the trap frequency is $1\,\text{MHz}$. Laser parameters are the same for both cases. Top: the off-resonant carrier is not included. The pulse leads to π rotation. Bottom: the off-resonant carrier is included with the inset showing the zoom-in of the boxed area in the main figure. The pulse does not cause π rotation because the pulse is no longer resonant to the transition due to the AC Stark shift. The fast oscillation shown in the inset figure is attributed to the off-resonant carrier.

perturbation. However, in general, satisfying this condition is not always possible. If the process involves several pulses, then even the small modification propagates throughout the entire process, leading to a substantial decrease in the fidelity of operation induced by the sequence of the pulses.

The off-resonant excitation can be suppressed by shaping the driving pulse such that the pulse is smoothly turned on and off [96, 97]. Fig. 7.3 visualises the dynamics of the two-level system using the Bloch sphere representation. The ion is initially in $|g\rangle$, which is represented by a state vector $\vec{R} = (0, 0, 1)$, and the state vector rotates around the axis on the Bloch sphere corresponding to the dressed-state eigenvectors, which are given as

$$
\begin{aligned}
|d\rangle &= \cos{(\theta/2)}\,|g\rangle + e^{i\phi}\sin{(\theta/2)}\,|e\rangle \\
|u\rangle &= \sin{(\theta/2)}\,|g\rangle - e^{i\phi}\cos{(\theta/2)}\,|e\rangle
\end{aligned}
\tag{7.1}
$$

where θ and ϕ are polar and azimuthal angles in the Bloch sphere. If the Rabi frequency is zero, the dressed-state eigenvectors are equal to the bare states, $|g\rangle$ and $|e\rangle$, leading to $\theta = \phi = 0$. If the off-resonant field is applied instantaneously (i.e. square pulse), the state vector rotates the axis on the Bloch sphere at angles θ and ϕ, which is indicated by $\vec{W}$ in Fig. 7.3(a). On the other hand, if the Rabi frequency is ramped up sufficiently slowly, satisfying the adiabatic condition $\tau \gg \pi/\delta$ where τ is a pulse shaping time and δ is a detuning frequency, then the rotation axis slowly moves from $\vec{W}_1$, which corresponds to $\theta = \phi = 0$, to $\vec{W}_2$ in Fig. 7.3(b), and the state vector adiabatically follows it. If the Rabi frequency is ramped down back to zero, the process returns all populations back to $|g\rangle$ (see Fig. 7.2(b)). If the driving field is on resonance, the adiabatic condition indicates that the shaping time τ has to be infinitely long, and consequently, a shaped pulse induces the same dynamics as a square pulse (see Fig. 7.2(c)). The pulse shaping can significantly reduce an error due to off-resonant excitation.

The precise shape of the pulse is not crucial as long as the adiabatic condition is satisfied; in our experiment, the amplitude of our pulse follows a squared-sine envelope:

$$
\Omega(t) = \begin{cases}
\Omega_{\text{peak}}\sin^2\!\left(\frac{\pi t}{2\tau}\right) & 0 \le t < \tau \\
\Omega_{\text{peak}} & \tau \le t < t_{\text{pulse}} \\
\Omega_{\text{peak}}\sin^2\!\left(\frac{\pi(t+\tau-t_{\text{pulse}})}{2\tau}\right) & t_{\text{pulse}} \le t < t_{\text{pulse}} + \tau
\end{cases}
\tag{7.2}
$$

where the area under the curve, which corresponds to the amount of rotation by the driving field, is preserved (i.e. $t_{\text{total}} = t_{\text{pulse}}$ where t_{pulse} is the pulse length of the square pulse) whether we use the square-pulse or amplitude-modulated one.
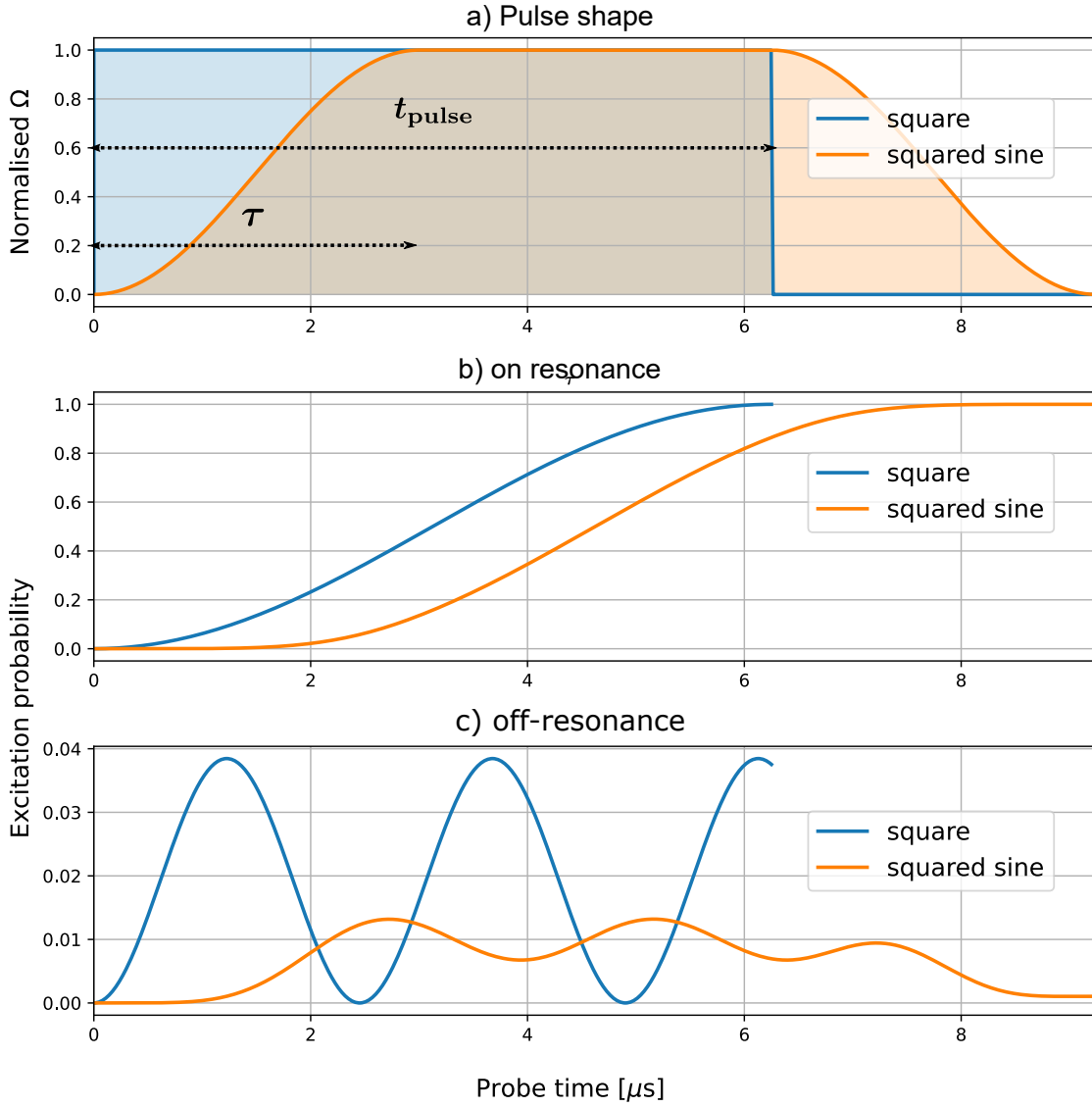
Figure 7.2: Effect of amplitude modulation of the driving pulse (a): amplitude of the driving pulse. We select τ such that it meets the adiabatic condition. Time evolution of initially prepared $|g,0\rangle$ while the carrier is driven (b) on resonance and (c) off-resonantly with $\delta = 500\,kHz$(b). The carrier Rabi frequency is $80\,\text{kHz}$ and pulse shaping time τ is $3\,\mu\text{s}$. The interaction time is set to be the π time ($6.25\,\mu\text{s}$). The interaction completely inverts the initially prepared $|g\rangle$ to $|e\rangle$, and the complete inversion is achieved whether the pulse is square or shaped when the carrier is driven on resonance. However, if the carrier is driven off-resonantly, the square pulse leads to the oscillation, whereas the shaped pulse initially excites $|g\rangle$ but brings it back to $|g\rangle$, leaving no population in $|e\rangle$.
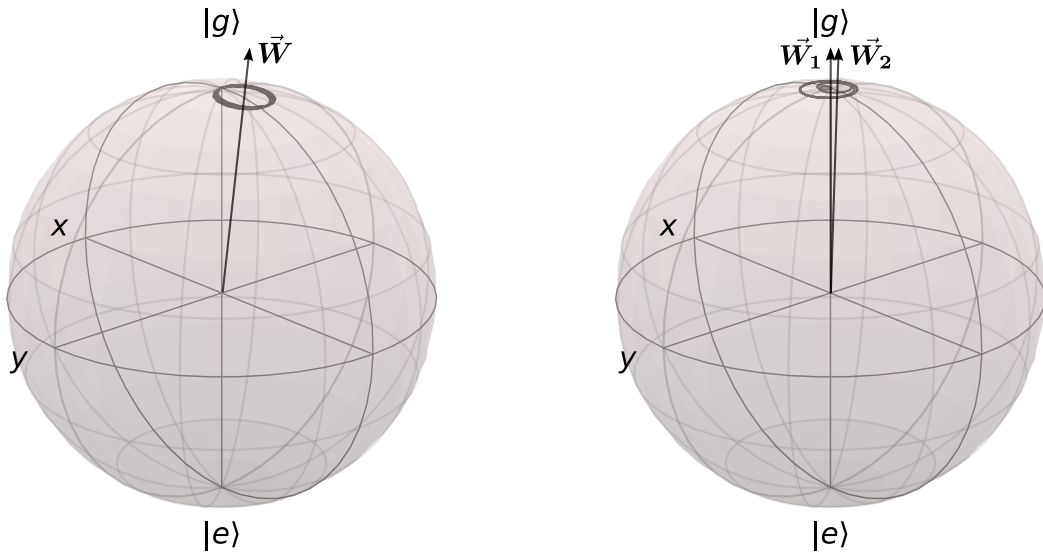
Figure 7.3: Dynamics of state vector driven by off-resonant field (laser parameters are the same as in Fig. 7.2(c). $\Omega_0 = 80\,\text{kHz}$ and $\delta = 500\,\text{kHz}$). Left: square pulse. The state vector rotates around a vector $\vec{W}$, which is represented by the dressed-state eigenvector when the system is driven by a square-shaped off-resonant field. Right: shaped pulse following Eqn. 7.2 with $\tau = 3\mu\,\text{s}$. The dressed-state eigenvector is initially aligned along $\vec{W}_1$, which is (0,0,1) in the sphere, and slowly moves to $\vec{W}_2$ as the Rabi frequency Ω is ramped up, and the eigenvector moves back to $\vec{W}_1$ as Ω slowly decreases to zero. The state vector follows the trajectory of the eigenvector; the population of $|g\rangle$ is partially excited and returned to $|g\rangle$.
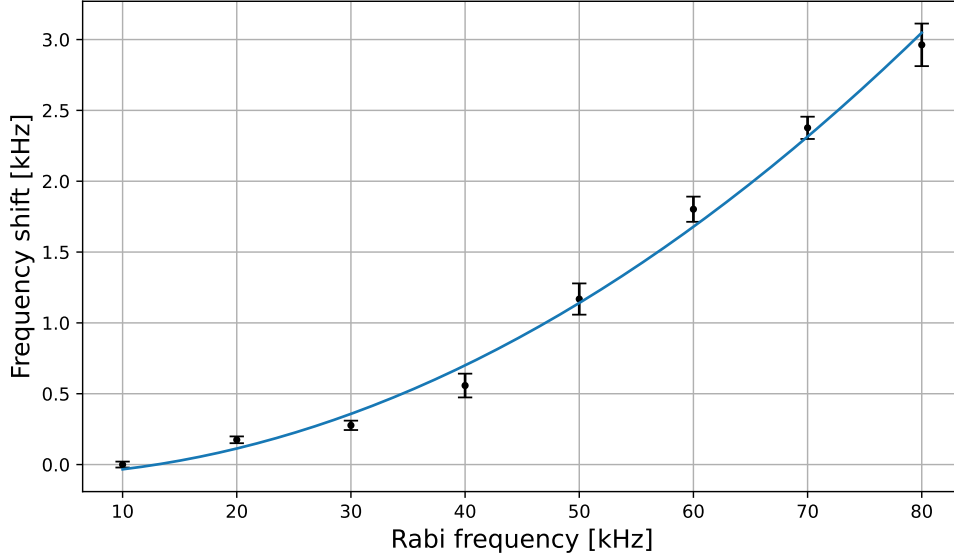
Figure 7.4: Frequency shift of the first-order blue sideband transition with reference to the first-order blue sideband resonance frequency measured at low power ($\Omega_{\mathrm{carrier}}/2\pi = 5\,\mathrm{kHz}$). The fit curve is modelled by Eqn. 7.3, showing that the measurements are consistent with the theory.

7.1.2 AC Stark Shift Compensation

Apart from off-resonant excitation, the off-resonant coupling produces an AC Stark shift. The shift introduces unwanted phase evolution while the interaction is driven, and consequently, the dynamics diverge from the one we desire. Typically, the trap frequency is much higher than the Rabi frequency ($\delta \gg \Omega$), and in this limit, the amount of AC Stark shift is approximated to the following:

$$\Delta_{SS} = \frac{\hbar\Omega^2}{2\delta} \tag{7.3}$$

where Ω and δ are Rabi frequency and detuning, respectively.

We can compensate for the shift by applying an additional pulse that produces the same amount of the shift in the opposite direction so that those two shifts can cancel each other [30]. Fig. 7.5 illustrates the method for the case in which we drive the first-order blue sideband. If the detuning of the additional pulse lies midway between the second- and third-order red sidebands (i.e. $\delta = -2.5 \cdot \omega_z$), then the detuning is sufficiently far away from the resonance of any transitions nearby; therefore, the additional pulse does not strongly drive any transitions, and we can ignore off-resonant excitation due to the additional pulse. If the Rabi frequency of the additional pulse is set such that the pulse gives a carrier Rabi frequency of $\sqrt{2.5} \cdot \Omega$ where Ω is the carrier Rabi frequency of the blue sideband, then the AC Stark shift by the additional pulse can cancel the AC Stark shift due to the first-order
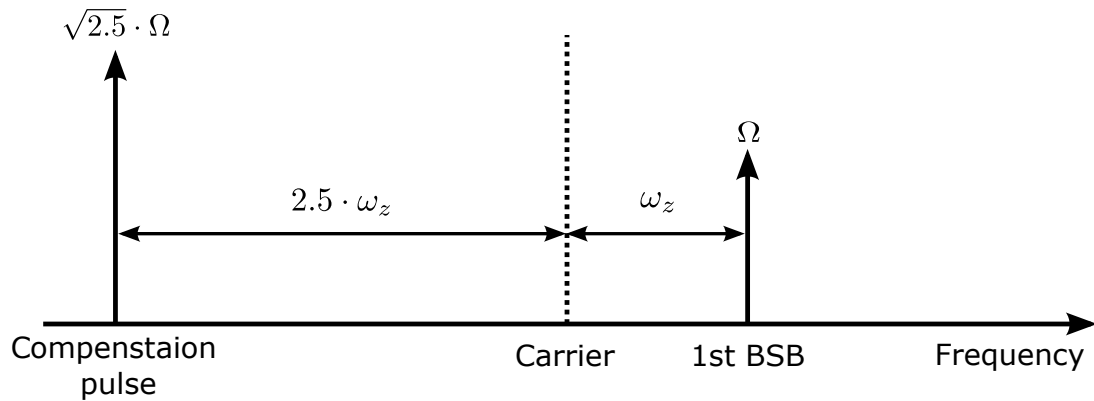
Figure 7.5: Frequency and Rabi frequency (power) of the first-order blue sideband and corresponding compensation pulse. Rabi frequency ($\sqrt{2.5}\omega_z$) and detuning ($-2.5\Omega_z$) of the compensation pulse are set such that the AC Stark shifts induced by the compensation pulse and the driving BSB pulse have the same magnitude but in opposite directions.

blue sideband:

$$\Delta_{SS,tot} = \frac{\hbar(\sqrt{2.5}\Omega)^2}{-2.5 \cdot 2\omega_z} + \frac{\hbar\Omega^2}{2\omega_z} = 0 \tag{7.4}$$

However, in practice, it is almost impossible to precisely set the Rabi frequency for each pulse. Therefore, we measure the net AC Stark shift using the standard Ramsey method where the two resonant $\pi/2$ pulses are applied, and the pulses are separated by delay τ. The second $\pi/2$ pulse has a variable phase ϕ relative to the phase of the first pulse. We measure the internal state of the ion at the end of the sequence as we vary the phase ϕ, giving an oscillatory signal (see. Fig. 7.6(a)).

When driving the first-order sideband transition, the resonance frequency of the transition is shifted by the off-resonant carrier, but when we turn off the laser and allow the system to freely evolve for τ, the resonance frequency returns to the unshifted frequency. This frequency difference due to the AC Stark shift gives the states a phase $e^{\pm\phi}$ where $\phi = \Delta_{SS,net}\tau$, giving a phase offset in Ramsey fringes $\Delta_{SS,net}\tau$. To find an appropriate Rabi frequency of the compensation pulse with the given detuning $\delta = \pm 2.5\omega_z$, we perform the Ramsey experiment with a different compensation pulse optical power by modulating the RF power to the corresponding AOM. As shown in Fig. 7.6(b), the measured phase offset varies with the RF power to the AOM, and we can obtain the right compensation amplitude by fitting the measurement to a linear function. However, the phase offset also becomes zero if this phase offset turns out to be an integer multiple of 2π. Therefore, we perform another Ramsey with the compensation parameters we obtained from the previous measurement, but with a different amount of delay to ensure that the phase offset is

a)

b)
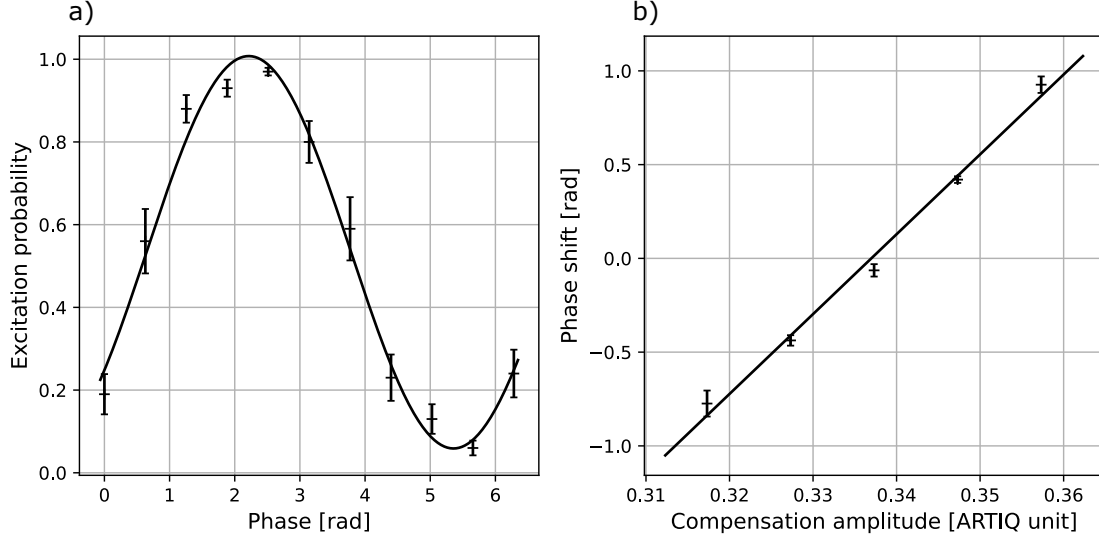
Figure 7.6: Ramsey phase scan for AC Stark shift compensation. Left: Ramsey phase scan. The phase offset in the oscillation corresponds to the phase shift due to the net AC Stark shift, $\Delta_{SS,drive} + \Delta_{SS,comp}$. Right: Measurement of phase offset as we vary the Rabi frequency of the compensation pulse, which is quantified in ARTIQ units because we cannot directly measure the optical power of the compensation pulse. We select the ARTIQ amplitude such that the phase offset becomes zero.

zero, not an integer multiple of 2π.

7.2 Motional Ramsey Interferometry

The motional degree of freedom of the ion is another source of quantum coherence in addition to its atomic states, which typically define a qubit, and here, we want to study multilevel coherence associated with the ion's motional state. The motional superposition state that consists of more than two basis states manifests multilevel coherence; the level of coherence is determined by the choice of basis states. The straightforward choice of basis states in the harmonic oscillator, which occurs in the case of a trapped ion, are the Fock states of motion $|n\rangle$. A state $|\psi\rangle = \sum_n a_n |n\rangle$ where a_n is a state amplitude associated to each Fock state $|n\rangle$ can be defined as a k-coherence state if it has k non-zero state amplitudes a_n [98, 99].

However, it is not straightforward to infer the quantum coherence associated with the motional state because this state is not directly measurable. To circumvent this issue, we use a mapping operation that maps our state into the measurement basis. These creation and mapping operations require coherent control of the ion, and we use the techniques explained in the previous section to realise those operations with high fidelity.
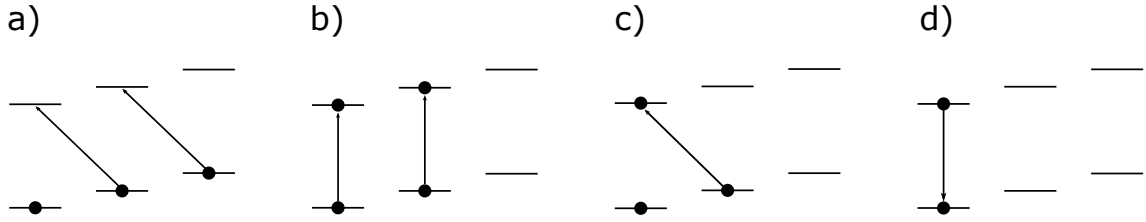
Figure 7.7: Synthesis of pulse sequence that creates $(|0\rangle + |1\rangle + |2\rangle)/\sqrt{3}$. (a): Synthesis procedure begins with the desired state, and the highest motional state $|2\rangle$ is transferred to $|1\rangle$ by the red sideband transition (b): all of the population of the highest motional state, now $|1\rangle$, is moved to $|g\rangle$ by the drive on the carrier. (c) and (d): The same procedure is repeated until the state arrives in the motional ground state.

7.2.1 Creation of Motional Superposition States

To study the quantum coherence associated with the motional degree of freedom, we first have to create a superposition of motional Fock states. An arbitrary motional superposition state can be created using a combination of the carrier and sideband transitions [92, 94]. Fig. 7.7 illustrates the procedure by which we can construct the pulse sequence to prepare the $(|0\rangle + |1\rangle + |2\rangle)/\sqrt{3}$ state from $|g, 0\rangle$, which is the typical initial state after the ground state cooling in our experiment. The procedure shown in Fig. 7.7 begins with the target state and transfers all of the population of the highest occupied motional state $|2\rangle$ to $|1\rangle$ by applying a resonant π pulse on the red sideband. In the new highest occupied motional state $|1\rangle$, the associated qubit state is a superposition of $|e\rangle$ and $|g\rangle$, and we bring it all to $|g\rangle$ with the carrier. We iterate the same process until the state finally arrives in $|g, 0\rangle$. We take the adjoint of the sequence that generates forward operation to create the required superposition from $|g, 0\rangle$.

After creating the motional superposition state, we measure the motional distribution of the state by driving the state on the resonant blue sideband. Using Eqn. 3.17, the excitation probability can be computed as follows:

$$P_e = \sum_{n=0} p_n \sin^2 \left(\frac{\Omega_{n,n+1}}{2}t\right) \tag{7.5}$$

Fig. 7.8 gives the measured Rabi oscillations on the blue sideband after different superposition states are created and the theoretical predictions, showing the created states by the creation operations are consistent with the desired superposition states.

7.2.2 Projective Mapping Operation

To infer the quantum coherence associated with the motional state of the ion, we must be able to measure the full motional state of the ion, not just the state amplitudes. In the ion trap, however, only the internal state of the ion is accessible via state-
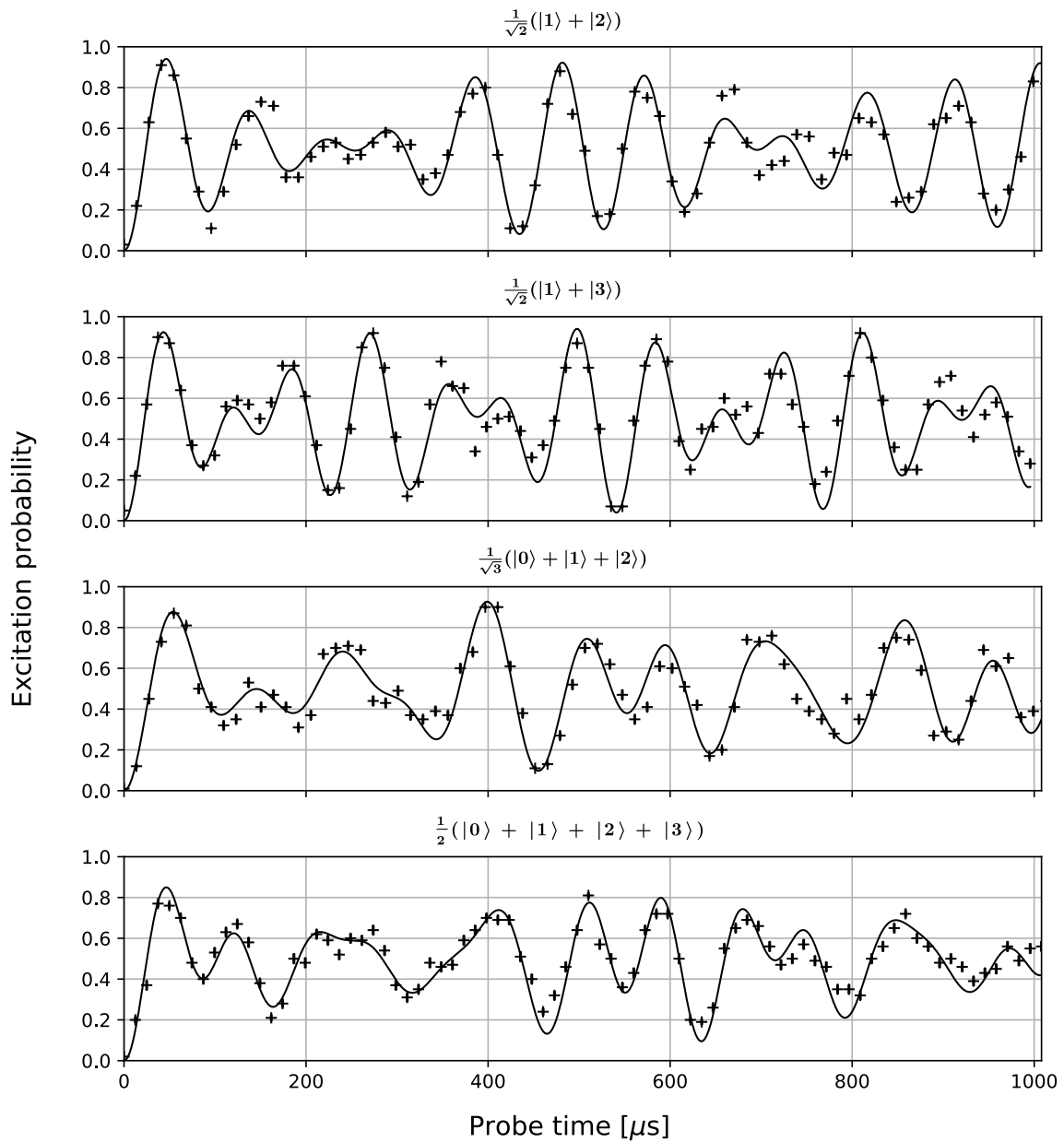
Figure 7.8: Time evolution of each state indicated while the blue sideband transition is driven. The expected oscillation for each state (solid) is highly consistent with the measurement results, suggesting that the state creation operation performs with high fidelity.
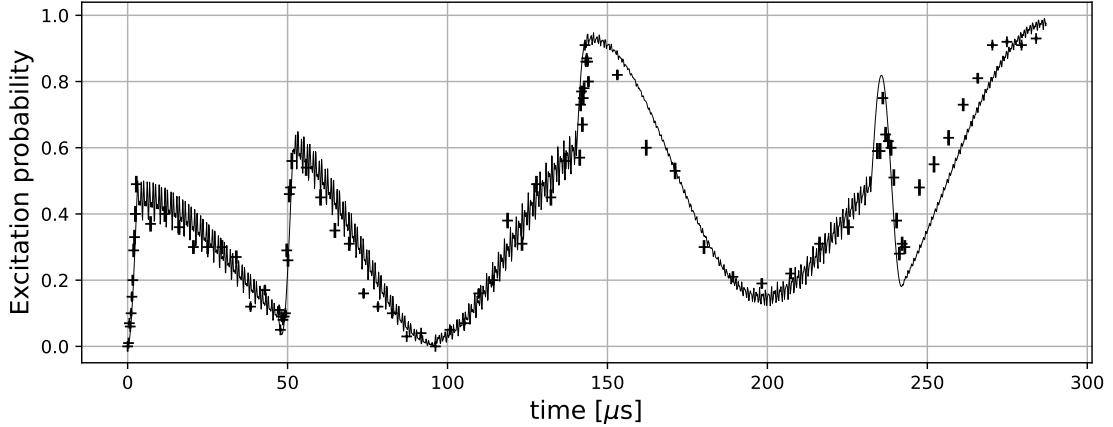
Figure 7.9: Time evolution of the $|g, 0\rangle$ state during the creation of $(|0\rangle + |1\rangle + |2\rangle)/\sqrt{3}$ and measurement mapping that bring the state to the excited state. There is a fast oscillation while the sideband transitions are driven, resulting from the off-resonant carrier.

dependent fluorescence, and the motional state is not directly measurable. Therefore, we map the target state and any states orthogonal to the target states to the different internal states, and this mapping operation enables measurement on the target state by measurement on internal state of the ion:

$$
\begin{aligned}
P_e &= \langle e | \, \mathcal{U}_m \, \rho \, \mathcal{U}_m^\dagger \, | e \rangle \\
&= \langle \psi_{\text{target}} | \, \rho \, | \psi_{\text{target}} \rangle = |\langle \psi_{\text{target}} | \psi \rangle|^2
\end{aligned}
\tag{7.6}
$$

where $\mathcal{U}_m$ is the unitary operator associated with the mapping operation, and ρ is the density matrix of the state.

If the target state consists of two motional Fock states, the required mapping protocol can be achieved by simply reversing the pulse sequence for the creation of the target state – this mapping protocol is exemplified by the second $\pi/2$ pulse in two-level standard Ramsey interferometry. However, in general, this argument is invalid as the adjoint of the creation sequence does not necessarily result in mapping any states orthogonal to the target state to the other atomic state. For instance, the measurement mapping protocol for $(|0\rangle + |1\rangle + |2\rangle)/\sqrt{3}$ can be be given as

$$
\begin{aligned}
\mathcal{U}_m(|g, 0\rangle + |g, 1\rangle + |g, 2\rangle) &\propto |e, \lambda_1\rangle \\
\mathcal{U}_m(|g, 0\rangle - 2\,|g, 1\rangle + |g, 2\rangle) &\propto |g, \lambda_2\rangle \\
\mathcal{U}_m(|g, 0\rangle - |g, 2\rangle) &\propto |g, \lambda_3\rangle
\end{aligned}
\tag{7.7}
$$

where $|g, 0\rangle - 2\,|g, 1\rangle + |g, 2\rangle$ and $|g, 0\rangle - |g, 2\rangle$ are one of examples of basis states
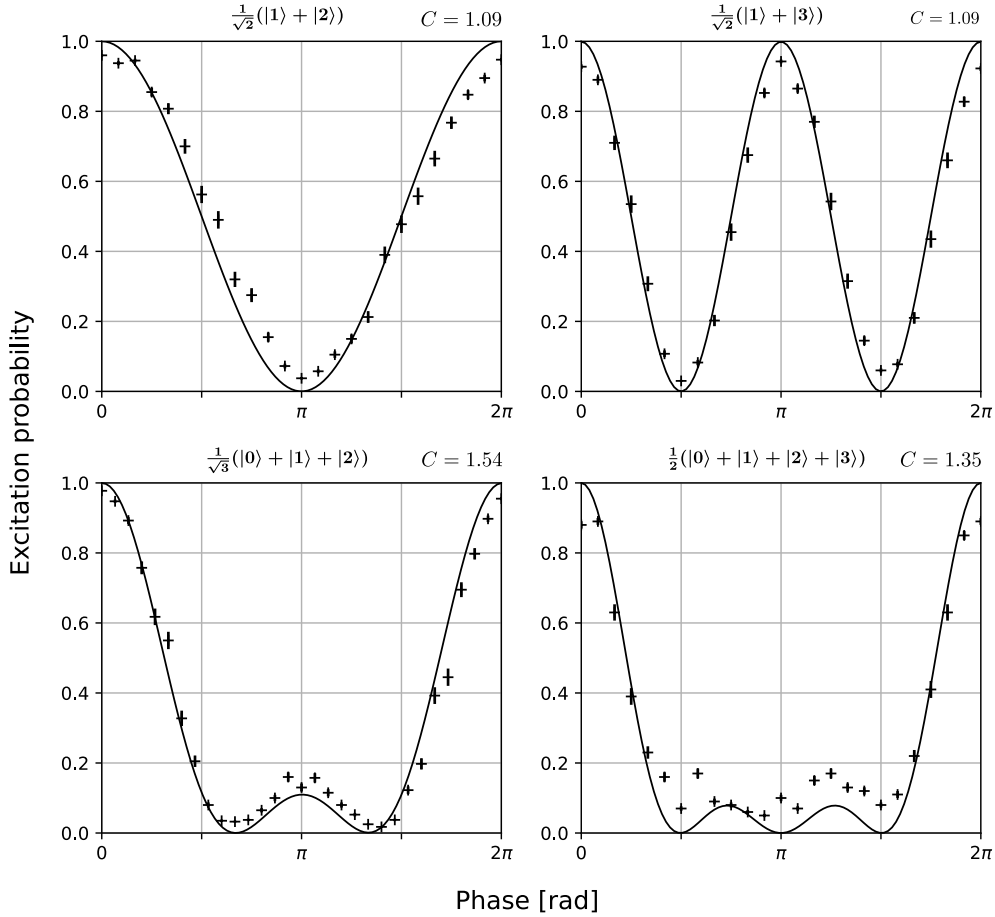
Figure 7.10: Interference patterns of the motional superposition states indicated on the figure. With the use of the certifier defined in Eqn. 7.9, the oscillatory interference patterns can suggest the order of coherence associated with the states to be tested.

orthogonal to the each other and the target state, and λ_i can be an arbitrary state since the state detection on atomic states will effectively trace out the motional degree of freedom. There must be an infinite set of sequences that generate the required mapping operation. When we select our protocol among the many candidates, our criterion is that the sequence involves the least number of pulses, and the entire sequence takes the shortest pulse time for each pulse to minimise errors due to non-zero detuning and power drift [100] (the actual values for the creation and mapping sequence are available in Ref. [56])

7.2.3 Interference Pattern

Using a qubit, which is a two-level system, we can observe an interference pattern by performing the simple two-level Ramsey experiment, which is analogous to a double-slit experiment in optics. Here, we wish to extend the Ramsey method to a

multilevel system (e.g. harmonic motion of a trapped ion), allowing for certifying higher-order coherence.

We now have all of the ingredients for measuring interference patterns with which the motional coherence can be inferred. For the state consisting of two motional Fock states (e.g. $(|0\rangle + |1\rangle)/\sqrt{2}$), the interference pattern can be obtained using standard two-level Ramsey interferometry where the measurement mapping operation can be achieved simply by reversing the creation sequence. Here, we wish to extend the method to higher-order level coherence.

Once the target state is created, the state ρ freely evolves under the system Hamiltonian with a single controllable parameter $\mathcal{U}_f(\phi)$ where ϕ is phase acquired during the free-evolution and is determined by the free-evolution time, and the mapping operation followed by the projective measurement on the qubit state, which effectively performs a measurement on the target state, giving an interference pattern as a result of interference between the motional states:

$$P_\phi = \langle e| \mathcal{U}_m \mathcal{U}_f(\phi)\, \rho\, \mathcal{U}_f^\dagger(\phi) \mathcal{U}_m^\dagger |e\rangle \tag{7.8}$$

In our experiment, instead of inserting a delay between creation and mapping operations, which allows for free-evolution, we add a phase offset to the applied laser field that drives the interaction as the phase acquired during the free-evolution can be interpreted as a phase offset with respect to the phase of the laser field – the phase offset is controlled by shifting the phase of the laser by $-\phi$, $+\phi$, 0 for the red, blue and carrier pulses of the mapping protocol.

Fig. 7.10 illustrates the interference patterns of different motional superposition states. Then, the oscillatory feature of the patterns resulting from interference between the motional state can be used to determine the order of the input state, using the certifier in the following from [101]:

$$C = \frac{M_3}{M_1^2}, \text{ where } M_n = \frac{1}{2\pi} \int_0^{2\pi} P(\phi)^n d\phi \tag{7.9}$$

where M_n is an nth order statistical moment.

There is a threshold for each order of coherence, and the C value of the pattern of k-coherence must exceed the threshold value associated with the k-coherent state. Thus, we can certify the order of the superposition state by measuring the value of C associated with the interference pattern derived from the state and compare the value of C with the threshold for the order we want to certify. We measure the C value for each pattern we obtained, and the value of C for each state agrees with this argument. For example, the 3-coherent state $((|0\rangle + |1\rangle + |2\rangle)/\sqrt{3})$ gives C of 1.54,

which is well above the threshold of 3-coherence (1.25) but well below 4-coherence (1.86). When we applied the certifier to 4-coherent state, the value of C for the state was measured to be 1.35. This is even below the threshold for 3-coherence. Hence, in this case, the certifier fails to verify the order of the state, but this result proves the certifier does not overestimate the order of coherence. That is, the certifier does not produce false positives.

Chapter 8

Bayesian Estimator

The coherent manipulation of trapped ions requires the accurate calibration of experimental parameters such as the frequency and power of a driving laser. Most logic operations assume that those parameters are stationary. In practice, however, it is inevitable for the parameters to drift over time; therefore, it is critical to frequently and accurately calibrate them to ensure that the dynamics we are driving are the ones we desire. In our experiment, the resonance frequency of the reference cavity, which is used for frequency stabilisation of the spectroscopic laser at 729 nm, drifts at a rate of 1 kHz/hour due to thermal fluctuations during the day. Furthermore, its power noticeably drifts in the long term, leading to different Rabi frequencies after a few hours, although the power of the 729 nm laser does not significantly drift during the single experiment, which takes several minutes. Hence, we must calibrate the laser from time to time during the day.

The typical method used to measure the frequency and power of the laser, which is related to the Rabi frequency, is to measure the excitation probability and fit it to a model that relates this probability to the parameters that must be estimated and control parameters that we can precisely vary in the experiment, such as interaction time. This is known as the frequentist approach because the method requires the preparation of identical copies to statistically estimate the excitation probability with a sufficient number of samples due to the probabilistic nature of quantum measurement. To estimate an experimental parameter, we vary the control parameters to measure how the excitation probability changes by taking multiple points, and each point is repeated to reduce statistical uncertainty. Consequently, this method is too slow to perform calibration before every experiment, and we might argue that it is inefficient because we obtain a piece of information, which is an excitation probability at a point, by repeating the same procedure more than a hundred times.

The alternative is the Bayesian approach, where the statistical properties of a quantum system are directly used rather than estimating the excitation probability

for each control parameter. In the Bayesian approach, we treat the model parameters as random variables and produce a hypothesis that the model parameters that we wish to estimate are a set of particular values $\mathcal{X}$, and the Bayesian inference tests whether the hypothesis is correct, providing a probability distribution of the model parameters that specifies the likelihood of these parameters being correct. This approach, therefore, makes it unnecessary to repeat the same experiment and consequently requires substantially fewer measurements to achieve the same accuracy and can be performed much faster. Quantum theory is inherently based on statistical theory: we cannot deterministically know the state of the quantum system, but we only know the probability of finding the system in a certain state through the projective measurement. Therefore, it is plausible that we can characterise our quantum system more efficiently using Bayesian inference, which is derived from statistical theory.

In this chapter, the general principle of Bayesian inference is presented, as well as how such inference can be applied to the estimation of the resonance and Rabi frequencies of the driving field, which parameterise the quantum dynamics of a trapped ion. Bayesian inference also allows for the simultaneous estimation of those two parameters by performing a single experiment, which will significantly shorten the time taken for the calibration routines.

8.1 Bayesian Inference

Suppose we have a system that is characterised by a set of unknown parameters $\mathcal{X} = \{x_1, x_2, \ldots, x_i\}$, so-called model parameters. We perform an experiment that is parameterised by a set of control parameters $\mathcal{C} = \{c_1, c_2, \ldots, c_j\}$, which are known and controllable. As we perform the experiment with k different sets of control parameters, we obtain a series of measurements $\mathcal{D} = \{d_1, d_2, \ldots, d_k\}$ where each datum is given for each set of control parameters. The goal of Bayesian inference is to infer the probability distribution of those unknown parameters $\mathcal{X}$ based on the measurements $\mathcal{D}$ we have obtained.

8.1.1 Bayes' Theorem

We begin with a prior distribution $P(\mathcal{X})$ that encodes any prior knowledge of the system. If we receive a new datum d and have a physical model or a likelihood function $P(d|\mathcal{X}; \mathcal{C})$ that specifies the probability of measurement outcome d conditional to the given model parameters $\mathcal{X}$ and control parameters $\mathcal{C}$, then we can update the probability distribution of unknown model parameters, taking the new measurement d into account using Bayes' theorem [102] :

$$P(\mathcal{X}|\mathcal{D};\mathcal{C}) = \frac{P(\mathcal{D}|\mathcal{X};\mathcal{C})P(\mathcal{X})}{P(\mathcal{D}|\mathcal{C})} \tag{8.1}$$

$P(\mathcal{D}|\mathcal{C})$ is the marginal probability distribution. This distribution is independent of the model parameters $\mathcal{X}$ and can, therefore, be simply considered as a normalisation factor for the posterior distribution, $P(\mathcal{X}|\mathcal{D};\mathcal{C})$, and can be computed as follows:

$$P(\mathcal{D}|\mathcal{C}) = \int P(\mathcal{D}|\mathcal{X};\mathcal{C})d\mathcal{X}. \tag{8.2}$$

The posterior distribution we have obtained can be used as the prior distribution for the following update procedure, and we update the probability distribution of the unknown model parameter by applying Bayes' theorem again. In other words, we can iteratively update the probability distribution of unknown parameters as new measurements arrive by repeatedly applying Eqn. 8.1. The probability distribution of $\mathcal{X}$ with the given series of measurements $\mathcal{D}$ up to a normalisation factor is given as

$$P(\mathcal{X}|\{d_1,\ldots,d_k\}) \propto \prod_{n=0}^{j} P(\mathcal{X}|d_n). \tag{8.3}$$

8.1.2 Parameter Estimation

At the end of the inference, we can estimate the unknown parameters by taking a mean value of the posterior distribution:

$$\langle \mathcal{X} \rangle \approx \int \mathcal{X} P(\mathcal{X}|\mathcal{D};\mathcal{C})d\mathcal{X}. \tag{8.4}$$

Bayesian inference also allows us to compute the uncertainty of the estimator, and this uncertainty is given as the covariance of the posterior distribution:

$$\begin{aligned} \mathrm{Var}(\mathcal{X}) &= \langle (\mathcal{X} - \bar{\mathcal{X}})^2 \rangle \\ &= \int (\mathcal{X} - \bar{\mathcal{X}})^2 P(\mathcal{X}|\mathcal{D};\mathcal{C})d\mathcal{X} \end{aligned} \tag{8.5}$$

where $\langle \cdots \rangle$ indicates the mean value of a quantity in the bracket.

8.1.3 Sequential Monte Carlo (SMC)

Updating the probability distribution through Bayes' rule requires evaluation of high-dimensional integration over the parameter space in Eqn 8.1. This process is, in general, analytically intractable or computationally expensive if we use the deterministic numerical integration method. To remedy these issues, we adopt the

sequential Monte Carlo (SMC) method, one of the Monte Carlo variants[1]. In SMC, the probability density function is approximated to a weighted sum of delta functions [104, 105, 106]

$$\sum_k \omega_k \delta(x - x_k) \tag{8.6}$$

where each delta function is centred at x_k, and w_k is its associated weight. Each delta function is also referred to as a particle; therefore, SMC is also known as a particle filter. The distribution of particles is not meant to directly approximate the probability distribution itself due to the fact that the particles support only finite discrete values in parameter space, but we can approximate the mean of the true distribution by taking the weighted averaged sum of all particles:

$$\int f(x) Pr(x) dx \approx \sum_k w_k f(x_k) \tag{8.7}$$

In SMC, the Bayes rule can be applied to update the particles' weights, and we consequently obtain the updated posterior distribution up to a normalisation factor when new observations become available:

$$w'_k \propto w_k P(\mathcal{D}|x_k) \tag{8.8}$$

The normalisation factor $\mathcal{N}$ can explicitly be computed by the sum of all updated weights of the particles

$$\mathcal{N} = \sum_j w_j P(\mathcal{D}|x_j) \tag{8.9}$$

Algorithm 1 shows the explicit algorithm of Bayes' Update to update the probability distribution of unknown parameters by applying Bayes' theorem.

---

[1]In the implementation of the SMC method, we adopt a Python package called Qinfer [103]. This package provides many pre-written functions, such as Bayes' update and the Lie-West re-sampler, which are necessary for performing Bayesian inference.

Algorithm 1: Bayes' update

Result: Posterior distribution $P(\mathcal{X}|\mathcal{D})$

Input: Particle weights $\omega_i, i \in \{1, 2, ..., n\}$

Input: Particle locations $x_i, i \in \{1, 2, ..., n\}$

Input: Control parameters $\mathcal{C}$

Input: New measurements $\mathcal{D}$

for $i = 1$ **to** n **do**

    $\tilde{\omega}_i = P(\mathcal{X}|\mathcal{D}; \mathcal{C}) \times \omega_i$; `// update weights for each particle using`
    `Bayes rule`

end for

$\tilde{\omega}_j \leftarrow \tilde{\omega}_j \sum_{i=1}^{n} / \tilde{\omega}_i$;   `// normalise posterior distribution`

return $\{\tilde{\omega}_j\}$

Re-sampling

As we proceed with the update of particle weights in SMC, the weights of most particles converge to zero because the true posterior should be a narrow distribution centred at the actual parameter values. Hence, most of the particles barely contribute to the estimates, and we are wasting the majority of the computational resources to track those particles with low weights. Furthermore, under-sampling of the distribution at high probabilities limits the precision of the estimator. Thus, we have to periodically re-sample the particles' locations. To decide when to re-sample the particles, we define the effective sample size [107]:

$$n_{ess} = 1 / \sum_i \omega_i^2, \tag{8.10}$$

and use it as diagnostic criteria. When the effective sample size is below the pre-set threshold, which is typically 10 in our implementation, we call the re-sampler. The re-sampling process is performed, following the Liu-West algorithm [108]. Algorithm 2 provides the complete algorithm of the Liu-West re-sampler.

Algorithm 2: SMC re-sampling algorithm

Result: Re-located particles with uniform weights

Input: Particle weights $\omega_i, i \in \{1, 2, ..., n\}$

Input: Particle locations $x_i, i \in \{1, 2, ..., n\}$

Input: Re-sampling parameters $a \in [0, 1]$

$h \leftarrow \sqrt{1 - a^2}$

$\mu \leftarrow \sum_{i=1}^{n} \omega_i x_i$;   `// mean of distribution`

$\sigma \leftarrow h^2 \sum_i^n \omega_i x_i x_i^{\mathrm{T}} - \mu\mu^{\mathrm{T}}$

for $i = 1$ **to** n **do**

    $\mu'_j \leftarrow ax_j + (1 - a)\mu$;   `// new mean for new particle location`

    draw x'_j from $N(\mu'_j, \sigma)$ distribution

    $\omega'_i \leftarrow 1/n$;   `// reset the weights to uniform`

end for

8.2 Implementation

We now wish to use Bayesian inference to estimate the unknown parameters of a quantum system in practice. We first have to derive an appropriate likelihood, or model function, that describes the probability of measurements that is available to us and is dependent on the parameters of interest as well as the control parameters. According to the Born rule in quantum mechanics, quantum measurements are inherently probabilistic, and the likelihood of finding a quantum system in a particular state $|d\rangle$ through the measurement is determined by the wavefunction overlap $\langle d| M |\psi\rangle$ where M is a measurement operator. Therefore, this wavefunction overlap $\langle d| M |\psi\rangle$ can be used as a likelihood function in the application of Bayesian inference to the quantum system.

In an ion trap, an available projective measurement involves determining the atomic state of the ion based on the state-dependent fluorescence. An outcome of the measurement is mapped to either $|g\rangle$ or $|e\rangle$, and the probability of finding the ion in $|g\rangle$ ($|e\rangle$) is given as $|\langle g|\psi\rangle|^2$ ($|\langle e|\psi\rangle|^2$) where $|\psi\rangle$ is a quantum state of the ion. When we use Bayesian inference to characterise the qubit represented by a trapped ion, we utilise the interaction of the ion with the resonant field, and the problem is equivalent to finding unknown parameters associated with the unitary time evolution generated by the atom-light interaction (see Chapter 3 for a more rigorous mathematical description of the interaction). Assuming the ion is a simple two-level system, when the ion interacts with the coherent light field, the atom–light interaction induces a unitary transformation in the form of

$$\mathcal{U}(\boldsymbol{\theta}) = \exp\{-\frac{i}{2}\boldsymbol{\theta} \cdot \boldsymbol{\sigma}\} \tag{8.11}$$

where $\boldsymbol{\sigma} = \{\sigma_x, \sigma_y, \sigma_z\}$ is a vector of Pauli operators, and $\boldsymbol{\theta}$ describe the transformation of the state associated with each Pauli operator. The interaction parameters $\boldsymbol{\theta}$ in the unitary transformation can be parameterised by laser parameters, such as the Rabi frequency Ω and detuning frequency δ :

$$\mathcal{U}(t) = \mathcal{U}(\Omega, \delta, t). \tag{8.12}$$

Using this unitary time evolution operator, a likelihood function associated with the measurement $|d_i\rangle$ where $|d_i\rangle \in \{|g\rangle, |e\rangle\}$ can be given as

$$P(d_i|\Omega, \delta; t) = \langle d_i|\mathcal{U}(\Omega, \delta; t)|i\rangle \tag{8.13}$$

where $|i\rangle$ is an initial state of the ion, which is typically $|g\rangle$ in our experiment. The likelihood function $P(d_i|\Omega, \delta; t)$ can be used in Bayesian inference to estimate Ω and δ.
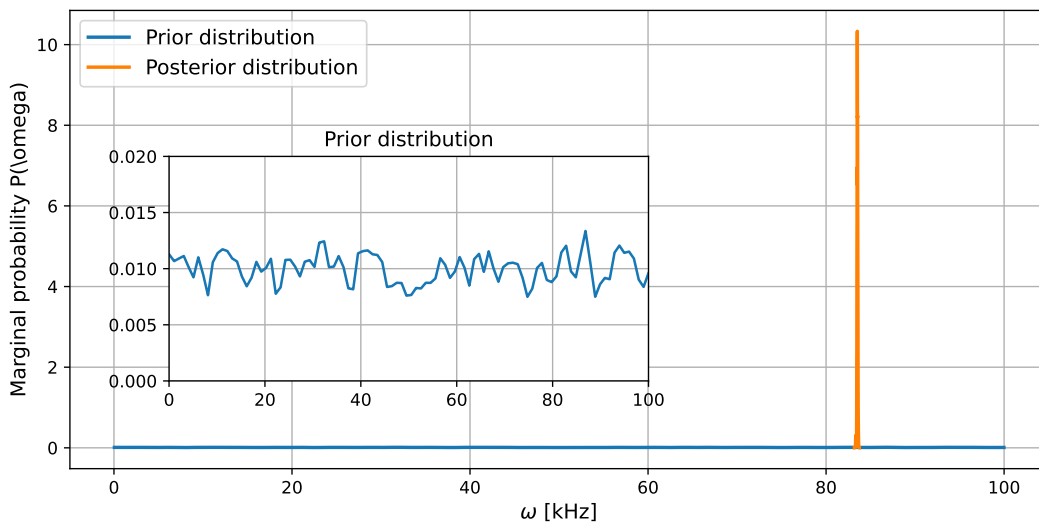
Figure 8.1: Prior (blue) and Posterior (orange) distribution represented by 3000 particles in SMC. The inset figure shows the initial prior distribution. The particle filter begins with uniform distribution, and the distribution is eventually transformed into a narrow peak (in principle a delta function centred at the true frequency) as the distribution is updated using the Bayes rule in SMC.
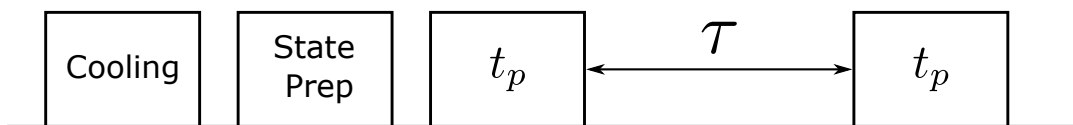
Figure 8.2: Experimental procedure for Ramsey method. The sequence includes cooling, state preparation and Ramsey interferometry with variable pulse time t_p and delay time τ.

The experiment begins with preparing the ion in the ground state $|g\rangle$. Then, we apply a sequence of laser pulses, which are parameterised by Rabi frequency Ω and detuning frequency δ, and we measure the state of the single trapped ion in σ_z basis, which is $\{|g\rangle, |e\rangle\}$. As we obtain a sequence of measurements $\mathcal{D}$, we update our prior distribution using Bayes' theorem. At the end of Bayesian inference, we estimate the parameters of interest and their statistical uncertainties by taking the averaged sum and covariance of the final posterior distribution obtained through SMC, respectively.

8.3 Ramsey Interferometry

The Rabi and detuning frequencies are the primary parameters that describe the quantum dynamics of a trapped ion. If we wish to estimate those parameters using Bayesian inference, we must design an experiment that involves a time evolution unitary transformation that depends on those parameters and control parameters that we can accurately know and precisely control. Ramsey interferometry is an excellent choice because it satisfies these criteria.

In Ramsey interferometry, we apply two resonant pulses, which are separated by a delay, and we simultaneously vary the length of the pulses and delay time. For the sake of simplicity, we set the pulse time for the first and second pulses to be the same, which is denoted as t_p. We use the pulse time t_p and delay time τ as the control parameters and measure the ion's internal state at the end of the experimental sequence.

Next, we derive the unitary transformation generated by the sequence of pulses. The typical initial state is the atomic ground state, and we must compute the excitation probability as a function of unknown parameters (Ω and δ) and control parameters (t_p and τ). By solving the relevant optical Bloch equation, we obtain the unitary time evolution propagator that describes the dynamics by a pulse with t, Ω and δ:

$$\mathcal{U}_{int}(t; \Omega, \delta) = \begin{bmatrix} e^{-\frac{it\delta}{2}}(\cos\frac{\Omega t}{2} + \frac{i\delta \sin\frac{\Omega t}{2}}{\Omega}) & -\frac{\Omega_0}{\Omega}ie^{-i(\frac{\delta t}{2}+\phi)}\sin\frac{t\Omega}{2} \\ -\frac{\Omega_0}{\Omega}ie^{i(\frac{\delta t}{2}+\phi)}\sin\frac{\Omega t}{2} & e^{\frac{it\delta}{2}}(\cos\frac{\Omega t}{2} - \frac{i\delta \sin\frac{\Omega t}{2}}{\Omega}) \end{bmatrix} \qquad (8.14)$$

where Ω_0 is the Rabi frequency on the resonance, $\Omega = \sqrt{\Omega^2 + \delta^2}$ is the generalised Rabi frequency, and δ is the detuning frequency. Using Eqn. 8.14, the probability of the ion being in $|g\rangle$ and $|e\rangle$ at the end of the Ramsey scan described in Fig. 8.2 can be computed as

$$\begin{bmatrix} P_g(t) \\ P_e(t) \end{bmatrix} = \mathcal{U}_{int}(t; \Omega, \delta)\, \mathcal{U}_{free}(\tau)\, \mathcal{U}_{int}(t; \Omega, \delta) \begin{bmatrix} 1 \\ 0 \end{bmatrix} \qquad (8.15)$$

Typically, the Rabi frequency is much greater than the detuning frequency $\Omega \gg \delta$, and in this limit, $\Omega \approx \Omega_0$ and the excitation probability with given Rabi and detuning frequencies can be approximated to

$$P(g|\Omega, \delta; t_p, \tau) = 1 - 2\sin^2\left(\frac{\Omega t}{2}\right)\cos^2\left(\frac{\Omega t}{2}\right)(1 + \cos(\delta\tau))$$

$$P(e|\Omega, \delta; t_p, \tau) = 1 - P(g|\Omega, \delta; t)$$

$$(8.16)$$

Eqn. 8.16 clearly shows the probability of finding the ion either in $|g\rangle$ or $|e\rangle$ is dependent on the Rabi and detuning frequencies; therefore, we can use the Ramsey scan to estimate those two parameters.

8.3.1 Rabi Frequency

The Rabi frequency Ω quantifies the coupling strength between the ion and applied light field, and it is critical to determine the precise value of Ω to create a particular superposition state; for instance, π time for complete population inversion and $\pi/2$ for equal superposition. In the Ramsey-like experiment described in 8.2, we vary only the pulse time t_p while delay τ is fixed to zero. This experiment is equivalent to the standard Rabi-type time scan, in which the interaction time becomes $t = 2t_p$. Assuming the laser is on resonance $\delta = 0$, by using Equ. 8.16, the excitation probability is given as

$$P(g|\Omega; t) = \cos^2\left(\frac{\Omega t}{2}\right)$$

$$P(e|\Omega; t) = 1 - P(g|\Omega; t)$$

$$(8.17)$$

where t is interaction time, and Ω is the Rabi frequency, which is the parameter to estimate. The excitation probability P_e oscillates at the Rabi frequency Ω. In a Bayesian inference for estimation of the Rabi frequency Ω, we use Eqn 8.17 as a likelihood function, and the interaction time t is the control parameter.

8.3.2 Detuning Frequency

One of the important values to determine for coherent operation on the ion is the detuning frequency of the laser from the resonance of the atomic transition. We can use the Ramsey experiment to estimate the detuning frequency. The Ramsey experiment in 8.2 is modified: assuming we already know the Rabi frequency at the power of the laser we are using, we set the pulse time t_p to the $\pi/2$ time (i.e. $t_p = \pi/(2\Omega)$), which creates the equal superposition state that is most sensitive to

the phase accumulated due to the detuning $\phi = \delta\tau$ during the free-evolution. We vary the delay time τ and use it as a control parameter in Bayesian inference. The likelihood functions are given by

$$P(g|\delta;\tau) = \sin^2\left(\frac{\delta\tau}{2}\right) \tag{8.18}$$

$$P(e|\delta;\tau) = 1 - P(g|\delta;\tau) \tag{8.19}$$

where δ is detuning with respect to the resonance frequency. The excitation probability oscillates at the detuning frequency. Thus, essentially, the Bayesian estimator for the detuning frequency is equivalent to the Rabi frequency estimation. We estimate the oscillation frequency, which is now equal to the detuning frequency.

8.3.3   Rabi Frequency and Detuning Frequency

In the Ramsey experiment we have discussed above, the Rabi frequency Ω and detuning frequency δ, which are parameters that must be estimated, are interconnected: the individual estimation of one is based on the assumption that we correctly know the other. For instance, if we obtain the Rabi frequency of the laser incorrectly, we cannot then accurately estimate the detuning frequency. Hence, it is beneficial to estimate the Rabi and detuning frequencies simultaneously without such an assumption.

Now, we scan both pulse time t_p and delay time τ, and Eqn. 8.16 guarantees that we can simultaneously estimate both parameters. In this case, the likelihood functions are given by Eqn. 8.16.

8.4   Experimental Results

We experimentally run the Ramsey experiment described in 8.2, and we estimate the Rabi and detuning frequencies using Bayesian inference. We evaluate the performance of the Bayesian estimator by comparing the result of the estimator with that of the fitting method. We perform the experiment first with the pre-determined sets of control parameters, and Bayesian inference is performed off-line afterwards[2].
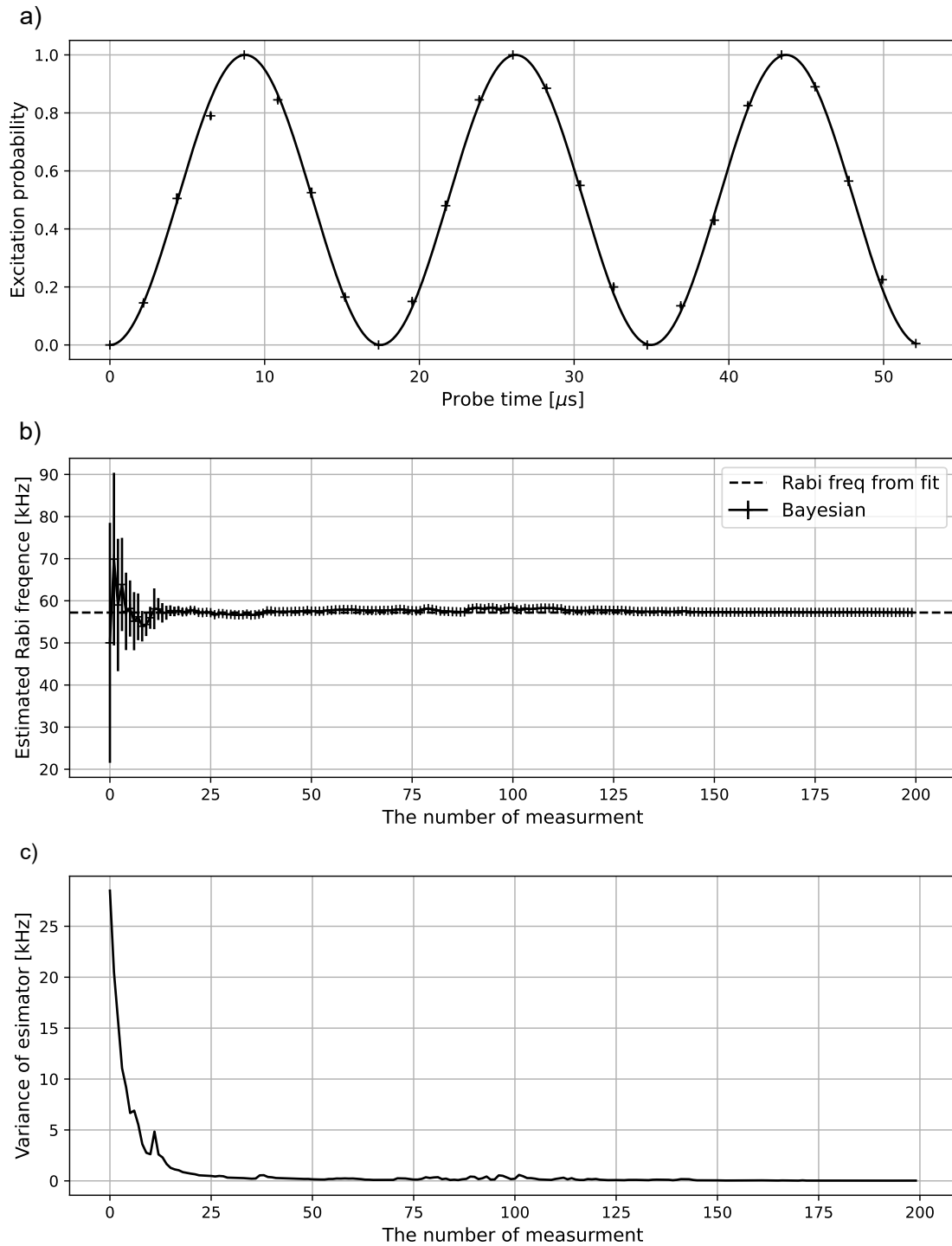
Figure 8.3: Measurement of Rabi frequency (a) Rabi oscillation on the carrier of $S_{1/2} \leftrightarrow D_{5/2}$, each data point is obtained by repeating the experiment at each interaction time 300 times. (b) the mean value of posterior distribution as a function of the number of measurement results taken to the estimator (c) variance of posterior distribution as more measurement results are fed to the Bayesian estimator

8.4.1 Rabi Frequency

Fig. 8.3 shows a typical Rabi oscillation where each data point is obtained by repeating the measurement for each pulse time 200 times. Then, we compare the estimated Rabi frequency from the fit and the estimation by Bayesian inference. Those two scans are subsequently performed without significant delay, ensuring that no significant drift in Rabi frequency between the scans occurs. Fig. 8.3 illustrates that the estimated value of the Rabi frequency by the Bayesian estimator rapidly converges to the value of the Rabi frequency obtained from the fit in Rabi oscillation as more and more measurements are provided to the Bayesian estimator. After the estimator receives approximately 25 measurements, the estimator already yields the uncertain of below 1 kHz, indicating that the Bayesian estimator can estimate the Rabi frequency more efficiently than the standard fitting method. The Bayesian approach requires substantially fewer measurements to achieve the same precision accomplished by the fitting method, in which more than a thousand measurements are taken.

8.4.2 Resonance Frequency

Typically, the required resolution for detuning estimation is much smaller than the Rabi estimation ($\approx 100\,\mathrm{Hz}$). A frequency spectrum is commonly used to measure the resonance frequency of transitions. This resolution of this method is limited by the Rabi frequency used because of the power broadening on spectral shape: measuring the resonance frequency with a small frequency resolution (e.g. 100 Hz) requires the Rabi frequency of the laser to be below the desired frequency resolution. Therefore, rather than directly comparing the results from the Bayesian estimator and the fitting method, we estimate the detuning frequency as we vary the frequency of the driving field, which can be precisely controlled with the use of AOM. Fig. 8.4 shows the estimated detuning frequency as we scan the frequency offset from -1 KHz to 1 kHz. The figure suggests that the estimated detuning frequency increases with the frequency offset applied, and the linear fit indicates that the estimated detuning frequency is strongly correlated with the applied frequency offset, giving a root-mean-square devitaion (RMSD) of the measurement to the fit of 48 Hz.
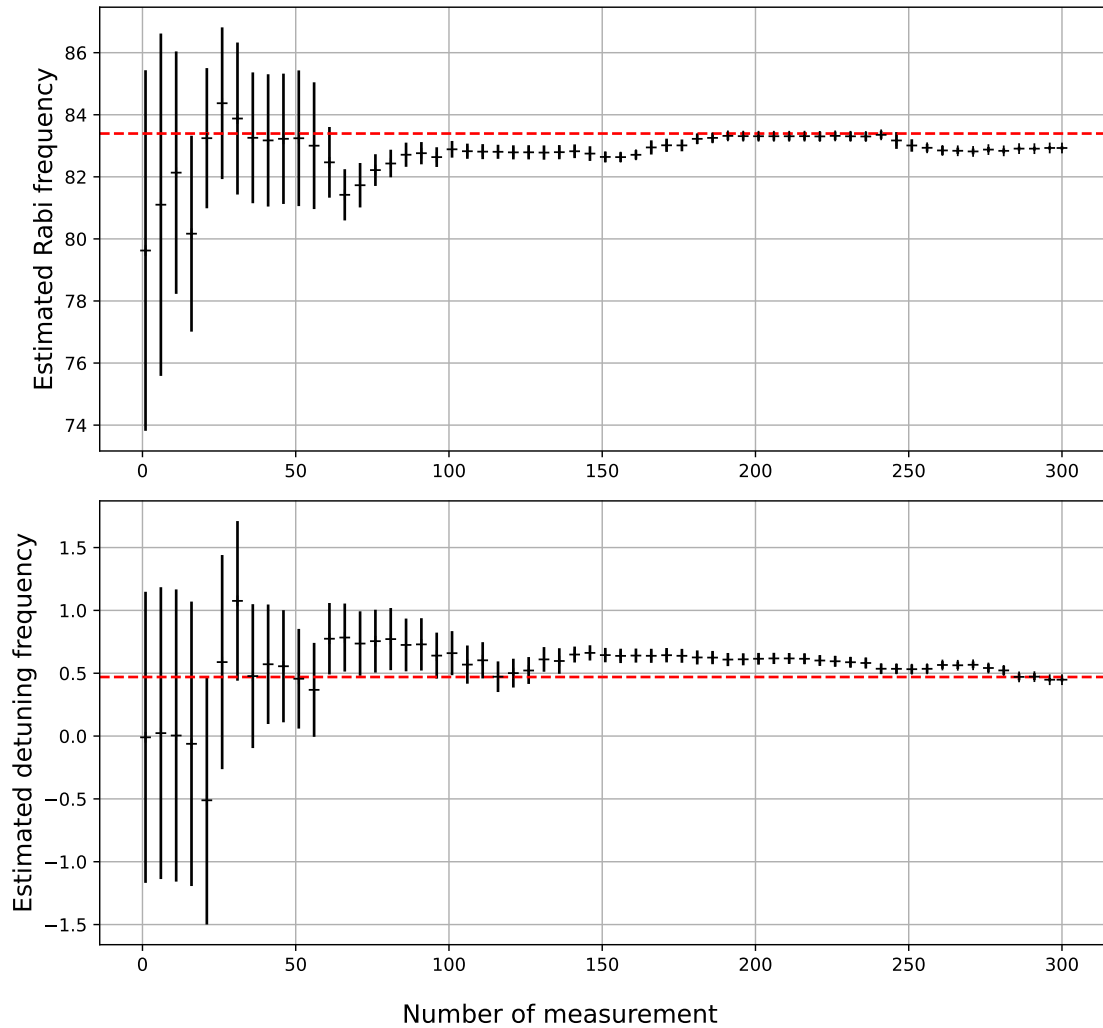
Figure 8.4: Estimated detuning frequency as a result of Bayesian estimator with different frequency offset is added. Root-mean-square deviation (RMSD) of the measurements to the linear fit is $48\,\mathrm{Hz}$.

8.4.3 Rabi and Resonance Frequency

We extend the estimator to the simultaneous estimation of the Rabi frequency and detuning. We perform the same Ramsey experiment, but this time, we vary both pulse t_p and delay times τ. In principle, the pulse and delay times can be chosen independently, but to simplify the scan procedure, we set the start and end value for each parameter and linearly scan those control parameters between the start and end value. To testify whether the estimator can give the same results with the same precision when it attempts to estimate two parameters simultaneously compared to the case where each parameter is estimated individually, we perform three scans:

---

[2]We do not carry out Bayesian inference parallel with taking measurements because, in our control system framework ARTIQ, retrieving the measurement results before the scan is completed takes a few seconds, and the process significantly prolongs the experiment if we perform them in parallel.
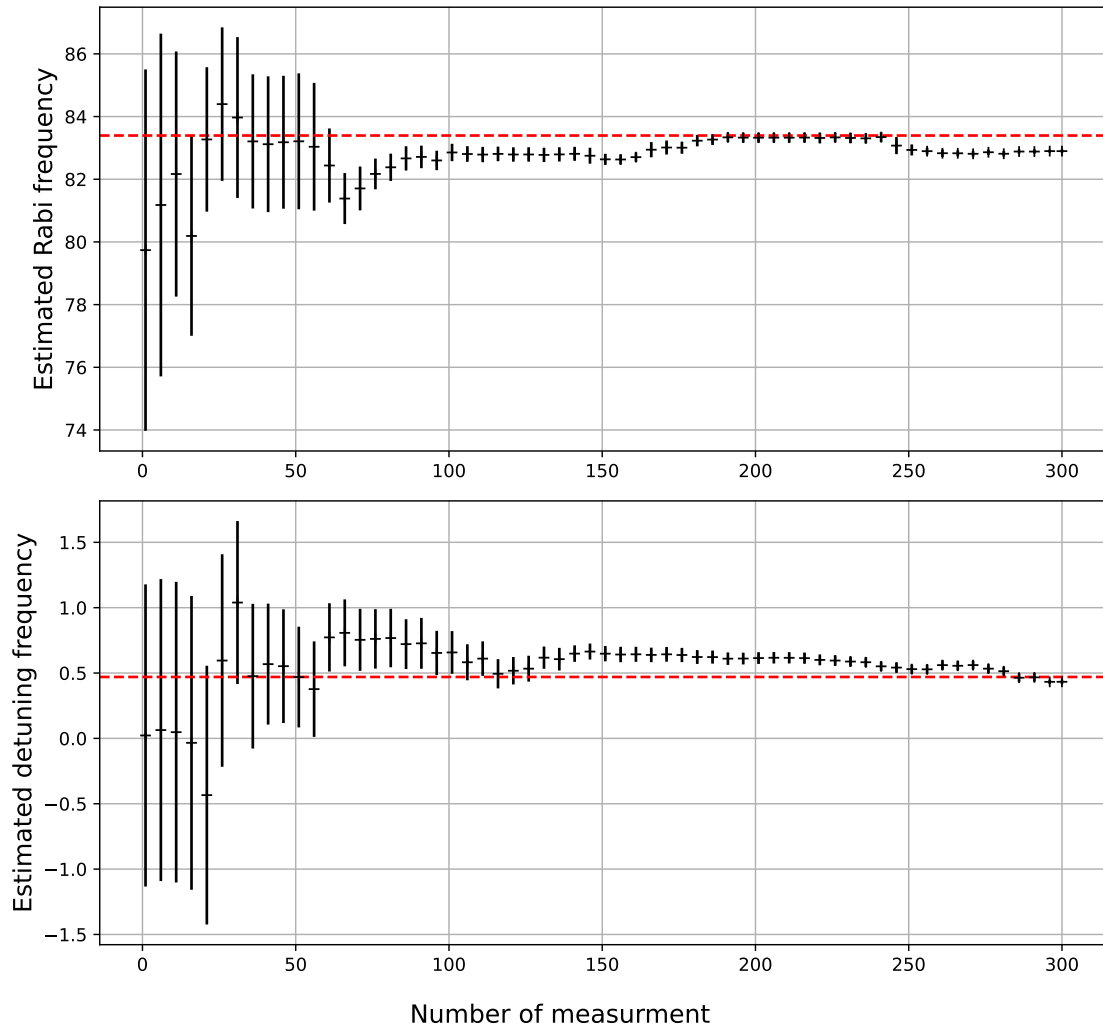
Figure 8.5: Simultaneous estimation of Rabi (Up) and detuning frequency (Down). The dashed lines indicate the Rabi and detuning frequencies that are independently measured from Rabi oscillation and Ramsey interferometry.

Rabi, detuning and Rabi & detuning. We perform one scan immediately after another to ensure that the laser parameters do not significantly drift between the scans. Fig. 8.5 compares the results of simultaneous estimation with individually estimated values and suggests that we can simultaneously estimate the two laser parameters without any significant loss of accuracy. However, the simultaneous estimation seems to require a higher number of measurements to reduce the uncertainty of the estimator to the same level.

8.4.4 Interleaved Scan

When we subsequently run the Bayesian estimator for the detuning frequency several times with a short delay $\approx 6\,s$ between scans, the result of the estimator varies from scan to scan. We can consider two possible scenarios: i) the estimator itself gives
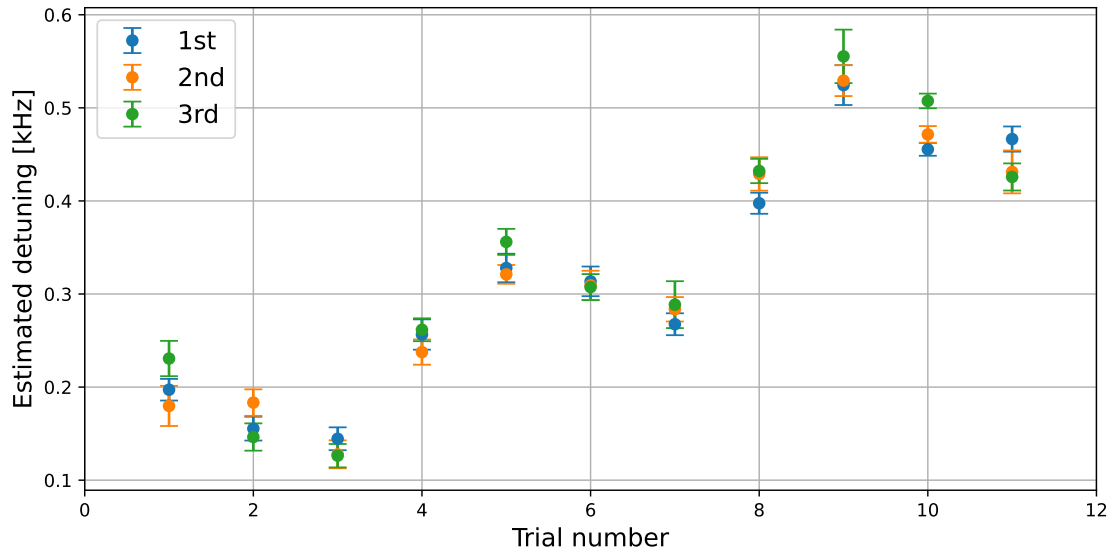
Figure 8.6: Comparison of the estimated detuning frequency from three inter-leaved scans. In each trial, three Ramsey experiments are inter-leaved. The detuning frequency drifted from trial to trial. However, three inter-leaved scans result in approximately the same detuning frequency within the error of Bayesian estimator.

a false result; ii) the actual detuning frequency drifts. In the former case, it is a matter of the estimator's reliability. To determine which is the case, we interleave three different scans: the sequence of detunings is $\{\tau_0, \tau_0, \tau_0, \cdots, \tau_N, \tau_N, \tau_N\}$ where τ_n is n^{th} delay time. Fig. 8.6 shows that there is no significant discrepancy between three estimated detuning frequencies obtained by the interleaved scan.

8.5 Sources of Error

8.5.1 Time-dependent Parameters

The likelihood function used in the Bayesian inference assumes that the parameters to be estimated are static. However, in a realistic scenario, the parameters of interest, such as the drive field's Rabi and detuning frequencies, always drift. Hence, if the parameters significantly drift during the experiment, our likelihood function cannot accurately describe our quantum system's dynamics, and consequently, the Bayesian estimator cannot accurately characterise the system.

8.5.2 Imperfect State Detection

Bayesian inference assumes that the outcome of measurement is entirely based on the probability that is determined by the model and control parameters. However, a detection error breaks this assumption. As explained in Sec. 2.3.2, the state-detection

based on state-dependent fluorescence may fail to detect the ion's internal state. The false detection can propagate false information throughout the process while the prior distribution is sequentially updated, following Bayes' theorem and results in the posterior distribution providing the wrong answer. For example, if the state detection gives the outcome of $|g\rangle$ although the ion is meant to be in the excited state with 100% probability with the given true model parameters (i.e. $P(e|\mathcal{X};\mathcal{C}) = 1$), Bayes' theorem (Eqn. 8.1) must then conclude that the probability of the parameters being true values becomes zero because $P(g|\mathcal{X};\mathcal{C}) = 0$.

8.5.3 Decoherence

The quantum system experiences a loss of its quantumness. This is so-called decoherence, which stops the Bayesian estimator from estimating the unknown parameters of interest, which is typically related to quantum coherence. To use Bayesian inference to estimate the unknown model parameter, the excitation probability, which is the only measurable quantity in an ion trap, has to be dependent on the model parameters and the control parameters. The parameters of interest are typically associated with the quantum system's quantum characteristics. As the system evolves toward the classical system, it loses its quantum coherence: the probability of the measurement is no longer dependent on the model parameters. Therefore, Bayesian inference becomes invalid. For example, Rabi oscillation gradually decays due to decoherence, and eventually, populations of $|g\rangle$ and $|g\rangle$ are equalised (i.e. the excitation probability is no longer dependent on the interaction time, which is the control parameter). Consequently, Bayesian inference is no longer available.

Chapter 9

Measurement-based Cooling

Cooling a quantum system down to its motional ground state is essential for many applications of quantum systems [109, 110, 111, 112]. In particular, for an ion trap in the context of quantum computation, cooling the ion to its motional ground state is crucial to the realisation of a qubit gate with high fidelity. The coupling strength of the ion to the light field varies depending on its populated motional state, and a thermally excited ion can occupy many different motional states, collectively referred to as a mixed state. If the ion is in such a thermal state, the Rabi oscillation, simply a single qubit gate, becomes an incoherent sum of oscillations at many different frequencies, leading to dephasing between the motional states and a rapid decrease in the visibility of Rabi flops. Although the Mølmer-Sørensen (MS) gate, which is a typical two-qubit gate scheme in an ion trap, is meant to be independent of the temperature of the ions, it still requires them to be sufficiently cool to bring them into the LD regime [78].

Over the last decades, several different means of achieving the motional ground state in an ion trap have been proposed and developed [113, 114, 115]. Among these
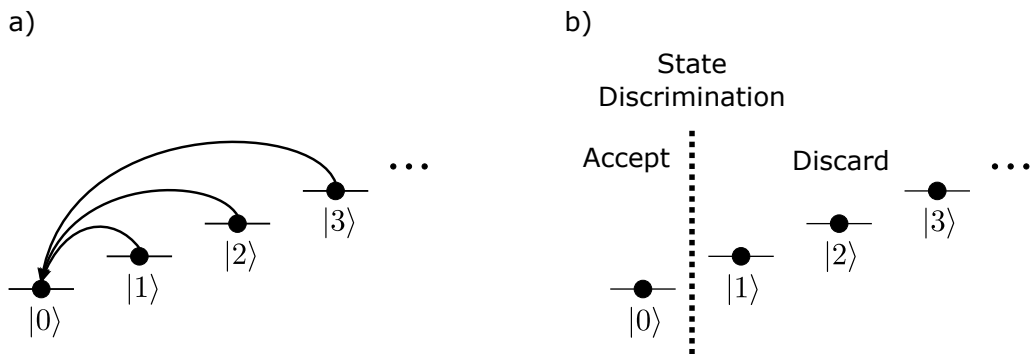
Figure 9.1: Comparison between (a) deterministic and (b) probabilistic cooling methods. The deterministic method aims to transfer the population of motional excited states $|n\rangle$ with $n \neq 0$ to the motional ground state $|0\rangle$, whereas the probabilistic method attempts to distinguish the motional ground state from the remaining motional states, selecting the occasions where the ion is in $|n = 0\rangle$.

methods, laser cooling techniques, including Doppler and resolved sideband cooling, have proved successful and are now routinely used in many ion trap experiments for ground-state cooling. In simple terms, these cooling methods aim to reduce the kinetic energy of the ion and eventually freeze it to the zero-point motion. In a quantum mechanical picture, an ion in thermal equilibrium at a non-zero temperature exists in a thermal state, in which different motional states are statistically mixed. For instance, if an ion is in a thermal state with an average photon number of $\bar{n} = 30$, then the probability that the ion is in the motional ground state is only 3%, indicating that it is more likely to exist in the motional excited state. In principle, the cooling techniques attempt to transfer the entire population of statistical ensembles of motional states $|n\rangle$ to the single motional ground state, which is a pure state (see Fig. 9.1(a)):

$$|n\rangle \rightarrow |0\rangle \text{ for all } n. \tag{9.1}$$

Thus, by the conclusion of the cooling process, all populations are transferred down to the motional ground state. This corresponds to the deterministic preparation of the motional ground state.

In our experiment, we initially cool the ion to the Doppler temperature, typically a few mK, and subsequently apply sideband cooling to transfer the ion into its motional ground state. After the Doppler cooling is applied, the ion is initialised to a thermal state, which is a statistical mixture of many different motional states. The subsequent resolved sideband cooling aims to transfer all populations of statistically mixed motional states to the pure motional ground state by coherently driving the red sideband transition $|n\rangle \leftrightarrow |n-1\rangle$. Hence, this cooling method deterministically prepares the ion in the motional ground state $|0\rangle$; this cooling scheme is therefore known as a deterministic cooling method.

Recently, an alternative cooling method that statistically selects the motional ground state from the statistical ensemble of motional states has been proposed [116, 117, 118, 119] and experimentally demonstrated in a mechanical resonator [120, 121]. Unlike deterministic cooling methods, such as resolved sideband cooling, this approach does not aim to prepare the ion in the pure motional ground state $|n = 0\rangle$, but rather aims to extract the subset of the statistical ensemble of motional states that is in the motional ground state (see Fig. 9.1(b)).
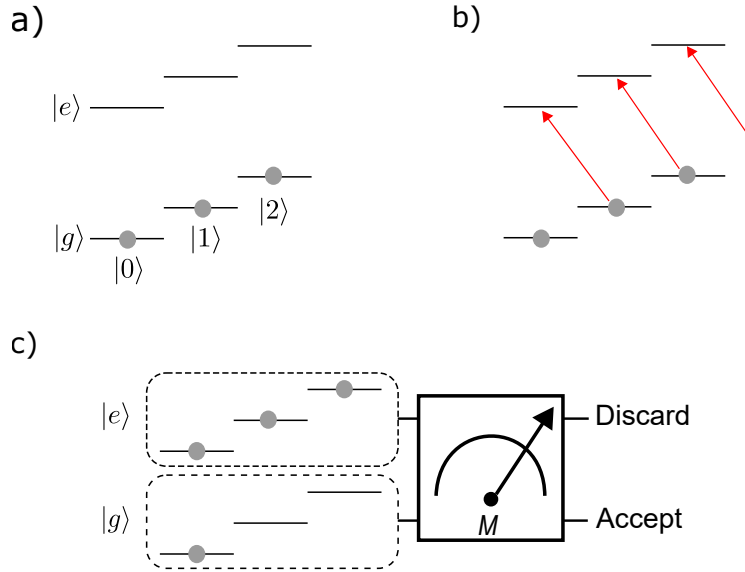
Figure 9.2: Principles of measurement-based cooling. (a) Initial state of the ion. (b) State-dependent mapping operation. It selectively excites the qubit state of the system if and only if the motional state is in $|n\rangle$ with $n \neq 0$. (c) Selection process. Only $|g\rangle$ carries the motional ground state $|n = 0\rangle$, so the motional ground state can be selected from the ensemble of motional states by accepting the state if and only if the outcome of projective measurement is $|g\rangle$.

9.1 General Principle of Measurement-based Cooling

This section begins by discussing the general principles underpinning measurement-based cooling, before shifting to a discussion of the implementation of this cooling method in an ion trap. The underlying approach of measurement-based cooling is to probabilistically select the motional ground state from an initial thermal distribution in which the motional ground and excited states are statically mixed.

If the motional state were accessible, measurement of the motional basis would enable discrimination of the motional ground state from the remainder of the motional states, and we could thus select the motional ground state from statistical ensembles of motional states via this measurement. However, motional states are typically not directly measurable. Therefore, we here consider a composite system that consists of an oscillator and an auxiliary state with discrete levels, which are measurable:

$$|\psi\rangle = |\psi_{motion}\rangle \otimes |\psi_{aux}\rangle. \tag{9.2}$$

Without loss of generality, we restrict the auxiliary state to a two-level system, referring to this state as a qubit. The coupling between the qubit and motional states can be established via the Jaynes-Cummings interaction:

$$H(t) = \frac{\hbar\Omega(t)}{2}\left(a\sigma_+ e^{i\delta(t)t} + a^\dagger\sigma_- e^{-i\delta(t)t}\right). \tag{9.3}$$

In addition, the projective measurement in the qubit basis must be available, and at least one of the qubit states must not be influenced by back-action of the measurement.

Fig. 9.2 illustrates the principle underpinning measurement-based cooling. First, we prepare the qubit state of the system in $|g\rangle$, with the motional degree of freedom in the thermal state:

$$\rho_{initial} = |g\rangle\langle g| \otimes \rho_{th}. \tag{9.4}$$

We then apply a state-dependent mapping operation that selectively excites the qubit state if and only if the ion is in the motional excited states $|n\rangle$ for $n \neq 0$; otherwise, the qubit state remains in $|g\rangle$:

$$|g\rangle|0\rangle \to |g\rangle|0\rangle$$
$$|g\rangle|n \neq 0\rangle \to |e\rangle|n-1\rangle. \tag{9.5}$$

As can be seen in Fig. 9.2(b), this operation leaves the qubit ground state $|g\rangle$ populated only by the motional ground state $|0\rangle$, correlating the qubit state to the populated motional states:

$$\rho = p_0|g\rangle\langle g| \otimes |0\rangle\langle 0| + \sum_{n=1} p_n|e\rangle\langle e| \otimes |n-1\rangle\langle n-1| \tag{9.6}$$

where $p_n = \bar{n}^n/(\bar{n}+1)^{\bar{n}+1}$ is the population of each motional state from the original thermal distribution. The projective measurement is

$$\hat{\mathcal{M}} = |g\rangle\langle g| \otimes \mathbb{1}. \tag{9.7}$$

If the projective measurement on $|g\rangle$ does not affect the oscillator's motional states, then the projective measurement operator effectively filters out any motional excitation associated with $|e\rangle$ from the ensemble of motional states, as it discards any instances in which the ion is projected onto the state $|e\rangle$; this is equivalent to cooling. That is, a measurement of the ion in $|g\rangle$ indicates that the ion's motion lies in the motional ground state; we henceforth say that this measurement 'heralds' the motional ground state.

We now consider the case where the state-dependent logic operation in Eqn. 9.5 is not ideal, with a non-zero transfer failure probability ϵ quantifying the fraction

of the population that is not inverted by the operation. This imperfect mapping operation degrades the fidelity of preparation of the motional ground state via the filtering operation, as incomplete population inversion for each n leaves the residual motional excitation populated in the qubit ground state, in which only the motional ground state should be populated. For the following quantitative analysis, we assume the transfer failure probability ϵ is independent of the motional quantum number n for simplicity. Subsequently, the state-dependent mapping operation in Eqn. 9.5 is modified to account for the non-zero ϵ as follows:

$$
\begin{aligned}
|g\rangle |0\rangle &\rightarrow |g\rangle |0\rangle \\
|g\rangle |n \neq 0\rangle &\rightarrow \epsilon |g\rangle |n\rangle + (1 - \epsilon) |e\rangle |n - 1\rangle .
\end{aligned}
\tag{9.8}
$$

where the first term in the summation indicates the residual motional excitation due to incomplete population inversion. As expected, this equation recovers Eqn. 9.5 when $\epsilon = 0$.

The probability of the motional ground state given that the ion is measured to be in $|g\rangle$, $P(n = 0|g)$, is given as

$$
P(n = 0|g) = \frac{1}{1 + \epsilon \bar{n}} .
\tag{9.9}
$$

If $P(0|g)$, which quantifies the efficiency of the cooling method, is lower than required, the state-dependent mapping and heralding measurement can be repeated. If this block of operations is repeated m times, then $P(0|g)$ is modified as follows:

$$
P(n = 0| \, m \times g) = \frac{1}{1 + \epsilon^m \bar{n}} .
\tag{9.10}
$$

This equation implies that $P(0|g)$ approaches unity as we repeat the cooling cycles, comprised of the state-dependent mapping followed by the heralding measurement, even if $\epsilon \neq 0$.

9.2   Implementation in $^{40}\text{Ca}^+$

In our implementation of the measurement-based cooling scheme in $^{40}\text{Ca}^+$, the auxiliary state, or qubit state, is defined by $\text{S}_{1/2,1/2}$ and $\text{D}_{5/2,1/2}$, denoted as $|g\rangle$ and $|e\rangle$, respectively. The coupling between the qubit and the motional states occurs via sideband transitions. As discussed in Sec. 2.3.2, the qubit state can be measured via state-dependent fluorescence: $|g\rangle$ and $|e\rangle$ can be distinguished by whether the ion scatters the photons or not. An ion in the ground state experiences a force due to its photon scattering, so the measurement itself affects the ion's motion. Therefore,

the heralding measurement must be performed on the basis of $|e\rangle$, rather than that of $|g\rangle$. This requires the ion's qubit state to be initialised to $|e\rangle$ before performing the state-dependent mapping operation. To meet this requirement, we apply rapid adiabatic passage (RAP) to the carrier transition to excite the qubit state of the ion without disturbing its motional state (a deeper discussion of RAP will be provided in the next section).

The next task is to determine how we can realise the state-dependent logic operation in our system. The logic operation cannot be realised by the standard resonant π pulse because Rabi frequencies vary with the motional phonon number n; consequently, there is no single interaction time that leads to a complete population inversion (π rotation) for all n. Therefore, we instead perform the RAP operation on the blue sideband transition as RAP can render complete population inversion less sensitive to experimental parameters, such as pulse area. Furthermore, when the ion is in $|e\rangle$, the blue sideband transition transfers the population from $|e, n\rangle$ to $|g, n-1\rangle$ for $n \neq 0$, whereas it is decoupled from $|e, 0\rangle$ since there is no lower motional state than $|0\rangle$. Hence, $|e, 0\rangle$ is effectively invisible to the transition, and the application of RAP to the blue sideband can therefore generate the required state-dependent mapping operation for the implementation of measurement-based cooling.

9.3   Rapid Adiabatic Passage

The RAP technique, a method of inverting a population from one state to another, was first proposed and experimentally demonstrated in nuclear magnetic resonance [122, 123]. Essentially, RAP is equivalent to the resonant π pulse in that both techniques completely invert the population of one state to another. However, RAP offers the advantage of inducing a complete population inversion that is more robust to experimental parameters such as coupling strength and pulse area. This robustness facilitates the population inversion in our case of interest, which involves many different motional states, each with a different coupling strength; we therefore use RAP to generate the state-dependent mapping operation required for measurement-based cooling.

9.3.1   Theory

RAP involves a frequency-chirped pulse with amplitude modulation:
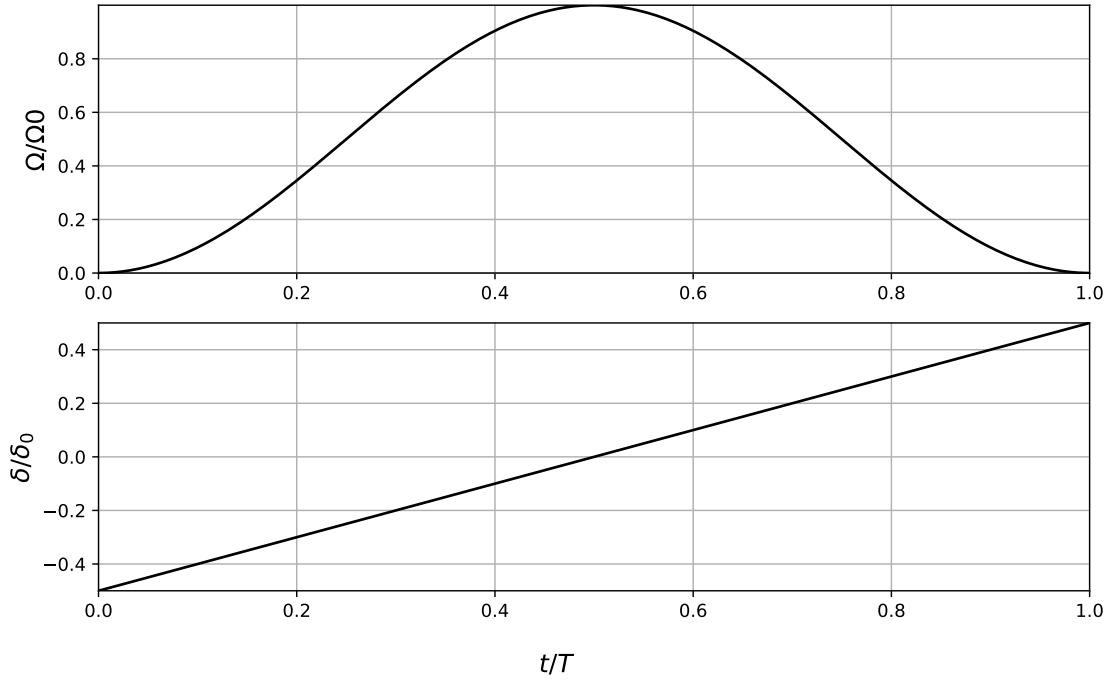
Figure 9.3: Time-dependent Rabi frequency $\Omega(t)$ (top panel) and frequency chirping $\delta(t)$ (bottom panel). The time derivative of $\Omega(t)$ at the start and end of the pulse is zero to ensure the adiabatic condition is satisfied when we switch the beam on (start) and off (end). In addition, the frequency of the laser is linearly swept from $-\delta_0/2$ to $\delta_0/2$.

$$\delta(t) = \frac{\delta_0}{T}\left(t - \frac{T}{2}\right),$$

$$\Omega(t) = \Omega_0 \sin^2\left(\frac{\pi t}{T}\right), \quad 0 \leq t \leq T \tag{9.11}$$

where δ_0 is a frequency scan range, and Ω_0 is a peak Rabi frequency. The time-dependent pulse profile is illustrated in Fig. 9.3. RAP can be understood more straightforwardly in a Bloch sphere representation. In a two-level system, the ground state and excited state can be represented by a vector pointing to the north pole $(0, 0, 1)$ and the south pole $(0, 0, -1)$ of the sphere, respectively. The time evolution of the Bloch vector is governed by the optical Bloch equation, and the dynamics can be visualised as the rotation of the Bloch vector $\boldsymbol{R}$, which is a unit vector, by a torque vector $\boldsymbol{W}$:

$$\frac{d\boldsymbol{R}}{dt} = \boldsymbol{W} \times \boldsymbol{R}. \tag{9.12}$$

The torque vector, $\boldsymbol{W}(t)$, is determined by the instantaneous laser parameter

$$\boldsymbol{W}(t) = (\Omega(t), 0, \Delta(t)). \tag{9.13}$$

113
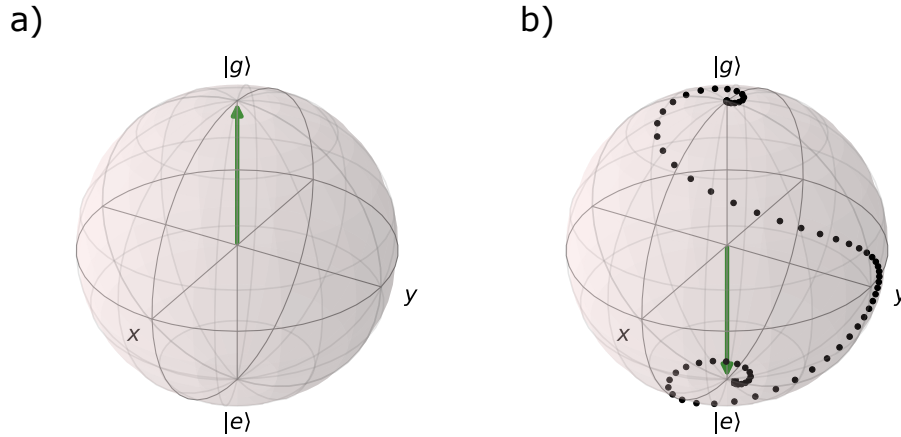
Figure 9.4: Bloch sphere representation describing rapid adiabatic passage. (a) Bloch vector aligned along $\hat{z} = (0, 0, 1)$ shows the system is initially prepared in the $|g\rangle$ state. (b) Time evolution of Bloch vector as we modulate the frequency and power of the driving field, finishing with alignment along $-\hat{z} = (0, 0, -1)$.

If the system is initially prepared in $|g\rangle$, the Bloch vector is aligned along the north pole of the sphere (see. Fig. 9.4(a)), and if the laser is sufficiently detuned below the resonance, the torque vector $\boldsymbol{W}$ is almost aligned along the state vector for $|g\rangle$. As we slowly increase the frequency as well as the Rabi frequency of the driving field, the torque vector slowly moves in response, passing the equator when the driving field is on resonance and eventually ending aligned along the south pole, which corresponds to the state $|e\rangle$. If the torque vector changes sufficiently slowly, satisfying the following adiabatic condition, [124]

$$\left|\frac{1}{\boldsymbol{W}}\right|\left|\frac{d\boldsymbol{W}}{dt}\right| \ll |\boldsymbol{W}|, \tag{9.14}$$

then the state vector adiabatically follows the torque vector as the state is transferred from $|g\rangle$ to $|e\rangle$. RAP can be extended to a multi-level system, such as a trapped ion. When we apply RAP to the carrier or sideband transition of the trapped ion, these transitions can be restricted to the Hilbert space spanned by $|g, n\rangle$ and $|g, m\rangle$, where n and m are chosen depending on the order of transition, and the same argument remains valid for the multi-level system [125].

9.4 Experimental Results

9.4.1 Rapid Adiabatic Passage

As can be seen in the bottom panel of Fig. 9.5, rapid adiabatic passage can smoothly transfer the population from $|g\rangle$ to $|e\rangle$ even if the ion is only Doppler cooled. However, the complete population inversion cannot be achieved by a resonant pulse.
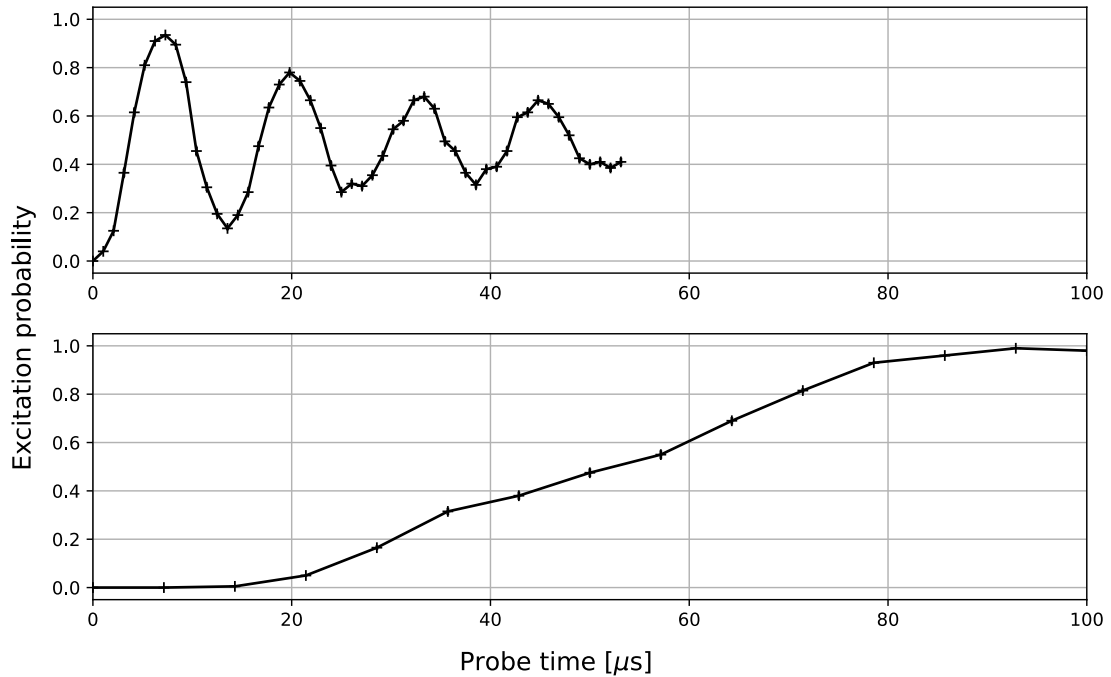
Figure 9.5: Excitation probability $P(e)$ during driving of the resonant carrier transition (Up) and driving of rapid adiabatic passage on the carrier with the amplitude- and frequency-modulated pulse described in Eqn. 9.11.

9.4.2 Transfer Efficiency

The primary component determining the performance of measurement-based cooling is the state-dependent mapping operation that separates the motional ground state from the remaining motional states by associating them with different qubit states. The success of this operation is quantified by a transfer efficiency of the RAP process, denoted η. We must first find appropriate laser pulse parameters for RAP, such as the total pulse length T and frequency chirping range δ_0, to ensure the RAP results in a transfer efficiency approaching unity when the ion is only Doppler cooled.

The ion is initially cooled using Doppler cooling and its qubit state is initialised to $|g\rangle$ via a state preparation pulse, which optically pumps the ion to the desired sublevel of the $S_{1/2}$ manifold. We then apply the frequency-chirped pulse described by Eqn. 9.11 and measure the resultant population of $D_{5/2,1/2}$. We measure the excitation probability, which quantifies the transfer efficiency, as we vary the total pulse length T for a given frequency chirping range δ_0 and peak Rabi frequency Ω_0.

Fig. 9.6 shows that the transfer efficiency η gradually improves and approaches near-unity as the pulse length T increases, as the adiabatic condition in Eqn. 9.14) is more likely to be satisfied by a longer pulse. For our cooling method, we select the shortest T that produces a transfer efficiency greater than 0.98. Although RAP is robust to changes in experimental parameters, we cannot reliably achieve a transfer efficiency of unity, leading to an error in the cooling method.
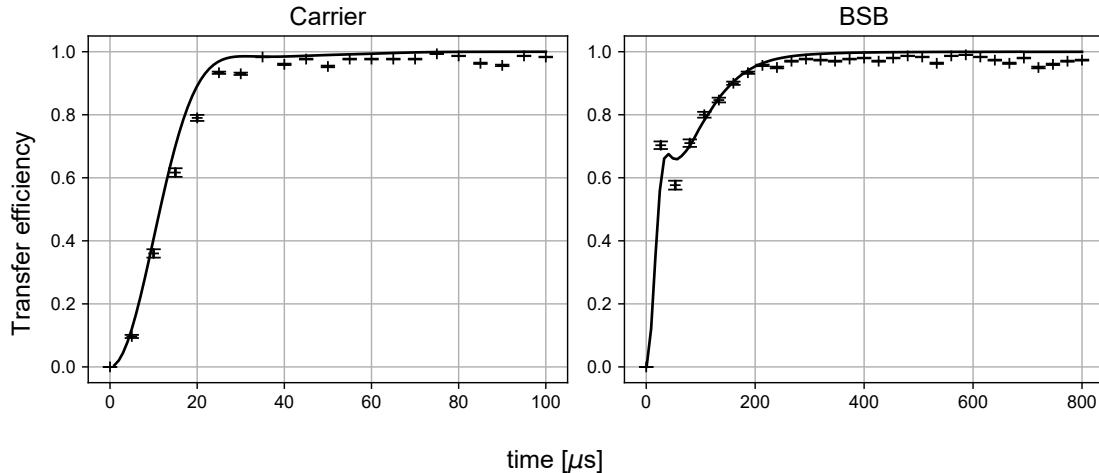
Figure 9.6: Transfer efficiency of RAP operation as a function of total length of the RAP pulse T. The rightmost figure (RAP on BSB) shows a dip in transfer efficiency at $T \approx 50\,\mu$s due to the breakdown of the adiabatic condition.

9.4.3   Cooling Efficiency

We experimentally implement measurement-based cooling using RAP, and measure its cooling efficiency, which is quantified by the probability of the motional ground state conditional upon the measurement outcome of $|e\rangle$, $P(0|e)$. The ion is initially prepared in the internal ground state with a thermal state using Doppler cooling followed by state preparation. We then apply RAP to the carrier transition to initialise the qubit state into $|e\rangle$ without disturbing its motional population. We subsequently apply RAP to the blue sideband, which provides the state-dependent mapping operation, and perform the heralding measurement. The conditional probability, $P(0|e)$, can be extracted from the dataset offline by discarding any results associated with a heralding measurement outcome of $|g\rangle$.

To quantify the cooling efficiency, $P(0|e)$, we must measure the motional population. Although we cannot directly measure the motional distribution, we can use the state-dependent coupling strength: we measure the Rabi oscillation on the carrier or blue sideband, given by

$$P(t) = \sum_{n=0} P(n|e) \sin^2 \left(\frac{\Omega_n t}{2} \right) \tag{9.15}$$

where Ω_n is the Rabi frequency for each motional state $|n\rangle$ ($\omega_n = \Omega_{n,n}$ for the carrier transition, and $\omega_n = \Omega_{n,n+1}$ for the blue sideband transition), and $P(n|e)$ is the conditional probability for each n. When Eqn. 9.15 is applied to a 'Doppler-cooled' case in Fig. 9.7 to measure the motional distribution, $P(n|e)$ becomes equal to the motional population p_n of a thermal state. Fig. 9.7 shows Rabi oscillation on the carrier and blue sideband with and without the application of measurement-based
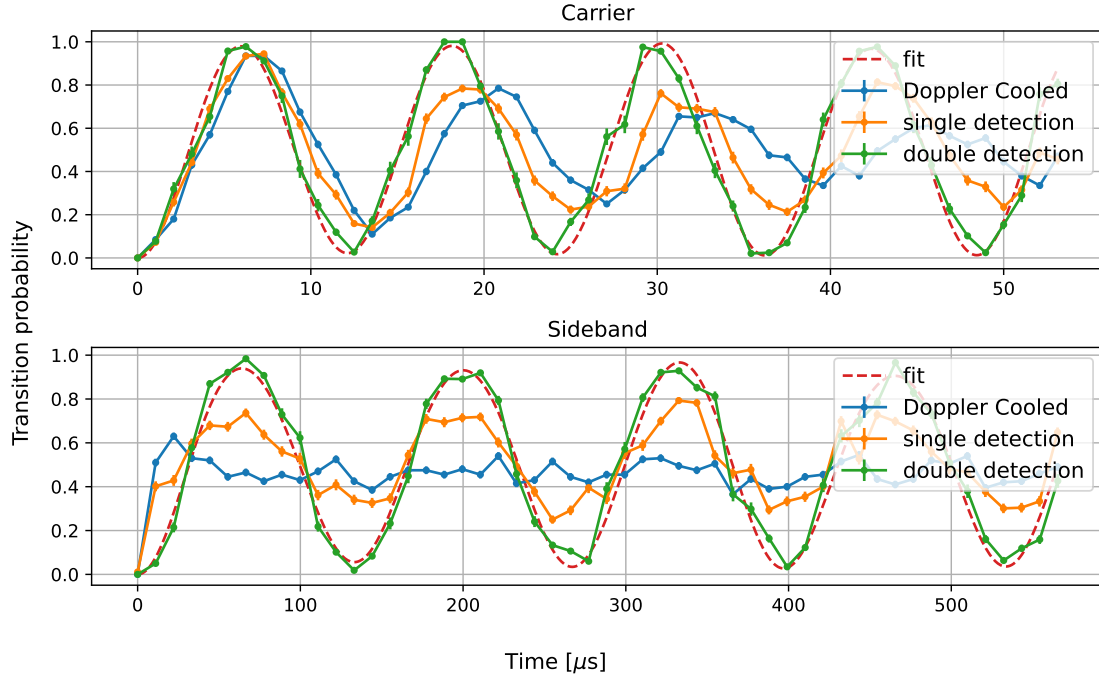
Figure 9.7: Transition probability $P_{i \leftarrow f}$ as a function of interaction time while $S_{1/2,1/2} \leftrightarrow D_{5/2,1/2}$ transition is driven on the carrier and 1st red sideband.

cooling and clearly demonstrates that the visibility of the oscillation is improved when such cooling is applied. Further, by fitting the oscillation to the model provided by Eqn. 9.15, we can measure the motional distribution, $P(n|e)$ or p_n. For the Doppler-cooled case, this motional distribution is characterised by a single parameter $\bar{n}$ (the averaged phonon number), as follows:

$$p_n = \frac{\bar{n}^n}{(\bar{n}+1)^{n+1}}. \tag{9.16}$$

The fit shown in Fig. 9.15 suggests that $\bar{n}$ is approximately 18 after Doppler cooling, which corresponds to $p_0 \approx 0.05$.

Assuming the transfer failure probability ϵ is independent of the phonon number n, as discussed in Sec. 9.1, the motional distribution after measurement-based cooling with non-zero ϵ can be simplified to:

$$
\begin{aligned}
p(0|e) &= \frac{1}{1+\epsilon\bar{n}} \\
p(n|e) &= \frac{\epsilon}{1+\epsilon\bar{n}} \left(\frac{\bar{n}}{1+\bar{n}} \right)^n, \text{ for } n \neq 0
\end{aligned}
\tag{9.17}
$$

After one block of the state-dependent mapping and heralding measurement is applied, $P(0|e)$ is estimated to be approximately 0.49. This suggests the motional ground state population is significantly increased by measurement-based cooling, but

remains substantially below unity. This result agrees with Eqn. 9.9, which yields 0.53 under our experimental conditions, including a transfer efficiency of $\eta = 0.98$ and average phonon number of $\bar{n} = 18$ after Doppler cooling.

The motional ground state population p_0 achieved by Doppler cooling is 0.05, suggesting that the probability of heralded success, which is the fraction of the heralding measurements that yield $|e\rangle$, must also be 0.05; however, this quantity is measured to be 0.08 after the application of one cooling cycle. This observation implies the existence of residual motional excitation due to the imperfect RAP. If we apply another stage of cooling, then $P(0|e)$ is estimated to be 0.96, and the heralded success probability is reduced to approximately 0.05. The high cooling efficiency is also illustrated by the high contrast visible in the Rabi flops in Fig. 9.7.

9.4.4 Motional Heating
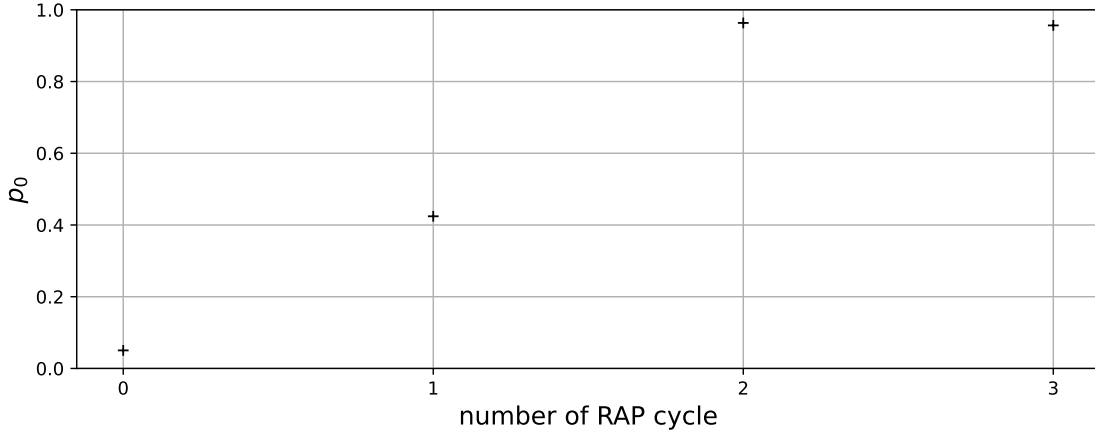
Figure 9.8: Motional ground state population p_0 as we repeat the block of mapping and heralding measurement operations. While p_0 gradually increases, it saturates below unity; repeating the cycle more than three times does not lead to further improvement.

As illustrated in Fig. 9.8, the motional ground state population is significantly improved as we repeat the cooling cycle, comprised of the RAP technique and the heralding measurement. However, further improvement is not achieved if we apply the cooling cycle more than twice. In particular, the motional ground state population $P(0|e)$ appears to saturate at 0.95; this observation prompts us to consider other sources of error.

As discussed in Sec.4.4, the trapped ion is heated by unknown sources, with the heating rate measured to be 36 phonons/s. By comparison, the state detection takes $1.5\,\mathrm{ms}$ to ensure the resulting photon distribution is distinctly separated. Therefore, given this heating rate, we expect $\bar{n}$ to increase by 0.054 during the detection period. This increase in $\bar{n}$ can account for the saturation at $p_0 \approx 0.95$.

Repeating the cooling cycle cannot resolve this heating issue because the cooling schemes always conclude with the state detection. Thus, the heating during the final state-detection period cannot be eliminated, regardless of the number of cooling cycles applied. Hence, the heating rate fundamentally limits the cooling efficiency of the method and is responsible for the saturation of p_0 in Fig. 9.8. We can alleviate this issue by shortening the detection period. However, in our current system, $1.5\,\mathrm{ms}$ is the shortest possible period that ensures the detection efficiency remains above 0.99, limiting the potential improvement to the cooling efficiency.

Chapter 10

Conclusion and Outlook

10.1 Initialisation of New Trap

At the very early stage of my Ph.D, I worked on the Penning trap, which was in use in the group at the time for quantum control experiments on a single trapped ion. I investigated the sudden drop in the optical coherence time of the ion in the trap to less than 1 ms, which the former Ph.D students had reported. However, I failed to identify the cause of the relatively short coherence time, and my attention was then more focused on the new Paul trap as the fabrication of electrodes for the new RF blade trap was completed. During the first year of my PhD, the majority of my work was then devoted to the initialisation of the new Paul trap.

In the initialisation of the new trap, I was mainly responsible for upgrading the primary spectroscopic laser at 729 nm, which is used to address the weak quadrupole transition $S_{1/2} \leftrightarrow D_{5/2}$ for qubit manipulation and resolved sideband cooling. I replaced the old homemade diode laser with the new commercial one, which already provides narrower intrinsic laser linewidth and more stable power stability. I also replaced the PID control electronics with FALC, which is a commercial loop filter from Toptica. We were not able to directly measure the linewidth of the laser, so we cannot directly compare the linewidth of the old and new lasers. However, the wavemeter measurements have clearly indicated the substantial suppression of frequency jitters and drift, and frequency locking seems to be more stable since the locking is kept for a long time (e.g. more extended than a day). The power at the trap is significantly lower than required for the experiment due to the power loss while the light is transported to the trap. Therefore, we need a tapered amplifier (TA) that amplifies the optical power of the laser at the trap. In addition, the newly built noise eater was implemented for power stabilisation. It sufficiently suppresses the long-term drift.

10.2   Coherent Control

When we drive the ion on the sideband transitions, the off-resonant carrier significantly affects the dynamics we expect in two distinct ways: off-resonant excitation and AC Stark shift. In this study, we numerically investigate the effect of off-resonant excitation and observe the off-resonant carrier induces fast oscillation at roughly the trap frequency ω_z if $\omega_z \gg \Omega$ where Ω is the Rabi frequency of the driving field in addition to the coherent population transfer by the targeted sideband transition. The off-resonant excitation is also a coherent process, so the effect becomes nulled if the interaction time is an exact integer of the oscillation period. However, this condition is challenging to be met in practice. We numerically show the pulse shaping by which the laser is slowly ramped up and down at each end of the pulse so that the dynamics occur in an adiabatic regime, and the state adiabatically follows the eigenstate of the dressed atom, suppressing off-resonant excitation.

In addition, we experimentally implement AC Stark shift compensation to counteract adverse AC Stark shift when we attempt to prepare the motional superposition state using the carrier and sideband pulses. We compensate for the shift by applying an additional pulse, which produces the AC Stark shift of the same magnitude but in the opposite direction to cancel the original AC Stark shift. We measure the net AC Stark shift using the Ramsey method and calibrate laser parameters for the compensation pulse so that the compensation results in zero net shift.

With the use of Stark shift compensation, we are able to prepare a motional superposition state. AC Stark shift compensation improves the fidelity. We experimentally demonstrate the coherence certifier proposed in Ref. [101]. The experimental implementation of the certifier on the motional state basis requires creation and the mapping operation, which maps the target state to one of the atomic states and any states orthogonal to the target state to the other atomic state. We successfully prepare motional states that consist of two or three motional Fock states and verify the order of motoinal coherence from the resulting interference pattern as the coherence certifier gives the C values higher than the threshold for respective orders. We apply the method to the 4-coherent state, but the resulting C value is below the threshold for 4-coherence. The observation illustrates the certifier does not overestimate the value of C (i.e. no false positives), although we fail to verify 4-coherence. This work has been published in [100].

10.3   Bayesian Estimator

Calibrating Rabi frequency and detuning frequency of each transition (carrier and sidebands) are essential routines. The calibrations have to be performed before

performing main experiments to ensure our laser parameters are correctly set as we wish. The calibration of those two parameters can be achieved by using the standard fitting method, which requires us to measure the excitation probability by repeating the experiment more than a hundred times for each data point. If we need ten data points to be able to fit the data set, the fitting method already requires a thousand measurements, and consequently the method is too slow. Those two parameters are not calibrated frequently (e.g. every hour) as the fitting method takes a few minutes, and we assume the parameters do not significantly drift.

We experimentally implement a Bayesian estimator that estimates the Rabi frequency and detuning frequency. The critical advantage of the Bayesian estimator over the standard fitting method is its speed. Contrary to the conventional fitting method, the Bayesian estimator does not require repeating the experiments to measure the excitation probability. Therefore, it gives an estimate of unknown parameters with a relatively small number of measurements.

Our results illustrate that estimating the Rabi frequency by Bayesian estimator needs only 25 measurements to give estimation with an uncertainty below $1\,\mathrm{kHz}$, whereas the standard fitting method requires more than a thousand measurements. The Bayesian estimator also allows for rapid estimation of detuning, and the estimator reliably gives the error of estimation below $100\,\mathrm{Hz}$ even with roughly 100 measurements. In addition, the Bayesian estimator can measure the two parameters at the same time. We do not have to measure the parameters individually, and this can save lots of time taken for the calibration routines. With the use of the Bayesian estimator, we can calibrate Rabi frequency and detuning more often.

10.4 Measurement-based cooling

Cooling the trapped ion down to zero-point motion is crucial in quantum applications, such as coherent control of the trapped-ion qubit. In our experiment, the ground state cooling is typically achieved by Doppler cooling and resolved sideband cooling. We experimentally demonstrate measurement-based cooling proposed for a mechanical resonator in Ref. [120] as an alternative cooling method. This cooling scheme is fundamentally different from resolved sideband cooling in that it aims to probabilistically extract the subset of a statistical ensemble of motional states, which is results from Doppler cooling, rather than bring all populations of motional excited states down to the motional ground state.

Contrary to the scheme described in [120], in our implementation of the method, we generate the state-dependent mapping operation, which separately maps the motional ground state and the rest of the motional states to different atomic states, by applying rapid adiabatic passage (RAP) on the sideband. We achieve transfer

efficiency of RAP on carrier and sideband reliably above 0.98, even if the ion is only Doppler cooled, in which the thermal distribution of the ion has $\bar{n}$ approximately 18.

By application of a single cooling cycle, which comprises RAP on the blue sideband and the following heralding measurement, the motional ground state population is improved to 0.49 from 0.05, which is achieved through Doppler cooling. However, this method is limited by imperfect RAP operation. The residual motional excitation populated in atomic excited state $|e\rangle$ due to imperfect RAP can be further removed by additional application of the cooling cycle, and the motional ground state population is further increased to 0.95. However, any further improvement is not achieved despite more cooling cycles applied. This is because of heating during the state detection, which takes 1.5 ms, and this heating issue cannot be resolved by repeatedly applying the cooling cycle. Although the measurement-based cooling does not outperform the pre-available resolved sideband cooling, our study proves the viability of a new cooling method, providing an option we can employ in case resolved sideband cooling is unavailable.

10.5   Outlook

Our long-term goal is to realise single- and two-qubit gates more robustly to experimental parameters and the inevitable environmental noise (e.g. magnetic field fluctuation). The techniques developed in this thesis can help us achieve this long-term goal.

We have already observed that pulse shaping and Stark shift compensation can tackle the adverse effect of off-resonant effects. Those off-resonant effects also hinder the realisation of the quantum gate with high fidelity. We might wish to apply those schemes developed and verified in this thesis to resolve the issue related to off-resonant effects.

As we increase the number of trapped ions, the cooling is more challenging, and resolved sideband cooling alone might take excessively long or be inefficient. In this case, we might use the measurement-based cooling incorporated with the sideband cooling. So far, we restrict the measurement-based cooling method to a single ion, in which we consider a single motional mode along the trap axis. However, in principle, the method can be extended to multiple ions, which generate more than one mode, by sequentially applying the cooling cycle to each mode. Therefore, we can use the measurement-based cooling technique to filter the remaining motional quanta resulting from sideband cooling.

With the high transfer efficiency ($\eta \approx 98$) of RAP we have achieved, we can employ RAP to aid state detection of the Raman qubit, which is defined by two sublevels of $S_{1/2}$. As discussed in Sec. 2.3.2, standard state detection is not applicable

to the Raman qubit. We have to transfer one of the $S_{1/2}$ sublevels to the $D_{5/2}$ state before performing the standard state detection at 397 nm. This process can be achieved by RAP more robustly against motional distribution of the ion, which provides a significant advantage over a resonant π pulse.

Bibliography

[1] T. D. Ladd, F. Jelezko, R. Laflamme, Y. Nakamura, J. L. O'Brien, and C. Monroe. Quantum computers. eng. *Nature (London)*, 464(7285):45–53, 2010. ISSN: 0028-0836. DOI: `10.1038/nature08812`.

[2] R. P. Feynman. Simulating physics with computers. eng. *International Journal of Theoretical Physics*, 21(6-7):467–488, 1982. ISSN: 0020-7748. DOI: `10.1007/BF02650179`.

[3] D. Deutsch. Quantum theory, the Church-Turing principle and the universal quantum computer. eng. *Proceedings of the Royal Society. A, Mathematical, Physical, and Engineering Sciences*, 400(1818):97–, 1985. ISSN: 1364-5021. DOI: `10.1098/rspa.1985.0070`.

[4] D. Deutsch and R. Jozsa. Rapid solution of problems by quantum computation. eng. *Proceedings of the Royal Society. A, Mathematical, Physical, and Engineering Sciences*, 439(1907):553–, 1992. ISSN: 1364-5021. DOI: `0.1098/rspa.1992.0167`.

[5] S. Lloyd. Universal quantum simulators. eng. *Science (American Association for the Advancement of Science)*, 273(5278):1073–1078, 1996. ISSN: 0036-8075. DOI: `10.1126/science.273.5278.1073`.

[6] P. W. Shor. Polynomial-time algorithms for prime factorization and discrete logarithms on a quantum computer. eng. *SIAM journal on computing*, 26(5):1484–1509, 1997. ISSN: 0097-5397. DOI: `10.1137/S0097539795293172`.

[7] F. Arute, K. Arya, R. Babbush, D. Bacon, J. C. Bardin, R. Barends, R. Biswas, S. Boixo, F. G. S. L. Brandao, D. A. Buell, B. Burkett, Y. Chen, Z. Chen, B. Chiaro, R. Collins, W. Courtney, A. Dunsworth, E. Farhi, B. Foxen, A. Fowler, C. Gidney, M. Giustina, R. Graff, K. Guerin, S. Habegger, M. P. Harrigan, M. J. Hartmann, A. Ho, M. Hoffmann, T. Huang, T. S. Humble, S. V. Isakov, E. Jeffrey, Z. Jiang, D. Kafri, K. Kechedzhi, J. Kelly, P. V. Klimov, S. Knysh, A. Korotkov, F. Kostritsa, D. Landhuis, M. Lindmark, E. Lucero, D. Lyakh, S. Mandrà, J. R. McClean, M. McEwen, A. Megrant, X. Mi, K. Michielsen, M. Mohseni, J. Mutus, O. Naaman, M. Neeley, C. Neill, M. Y. Niu, E. Ostby,

A. Petukhov, J. C. Platt, C. Quintana, E. G. Rieffel, P. Roushan, N. C. Rubin, D. Sank, K. J. Satzinger, V. Smelyanskiy, K. J. Sung, M. D. Trevithick, A. Vainsencher, B. Villalonga, T. White, Z. J. Yao, P. Yeh, A. Zalcman, H. Neven, and J. M. Martinis. Quantum supremacy using a programmable superconducting processor. eng. *Nature (London)*, 574(7779):505–510, 2019. ISSN: 0028-0836. DOI: `10.1038/s41586-019-1666-5`.

[8] D. P. DiVincenzo. The physical implementation of quantum computation. eng. *Fortschritte der Physik*, 48(9-11):771–783, 2000. ISSN: 0015-8208. DOI: `10.1002/1521-3978(200009)48:9/11<771::AID-PROP771>3.0.CO;2-`.

[9] Y. Wu, W.-S. Bao, S. Cao, F. Chen, M.-C. Chen, X. Chen, T.-H. Chung, H. Deng, Y. Du, D. Fan, M. Gong, C. Guo, C. Guo, S. Guo, L. Han, L. Hong, H.-L. Huang, Y.-H. Huo, L. Li, N. Li, S. Li, Y. Li, F. Liang, C. Lin, J. Lin, H. Qian, D. Qiao, H. Rong, H. Su, L. Sun, L. Wang, S. Wang, D. Wu, Y. Xu, K. Yan, W. Yang, Y. Yang, Y. Ye, J. Yin, C. Ying, J. Yu, C. Zha, C. Zhang, H. Zhang, K. Zhang, Y. Zhang, H. Zhao, Y. Zhao, L. Zhou, Q. Zhu, C.-Y. Lu, C.-Z. Peng, X. Zhu, and J.-W. Pan. Strong quantum computational advantage using a superconducting quantum processor. *Phys. Rev. Lett.*, 127:180501, 18, Oct. 2021. DOI: `10.1103/PhysRevLett.127.180501`.

[10] D. Vion, A. Aassime, A. Cottet, P. Joyez, H. Pothier, C. Urbina, D. Esteve, and M. H. Deviret. Manipulating the quantum state of an electrical circuit. eng. *Science (American Association for the Advancement of Science)*, 296(5569):886–889, 2002. ISSN: 0036-8075. DOI: `10.1126/science.1069372`.

[11] M. McEwen, D. Kafri, Z. Chen, J. Atalaya, K. J. Satzinger, C. Quintana, P. V. Klimov, D. Sank, C. Gidney, A. G. Fowler, F. Arute, K. Arya, B. Buckley, B. Burkett, N. Bushnell, B. Chiaro, R. Collins, S. Demura, A. Dunsworth, C. Erickson, B. Foxen, M. Giustina, T. Huang, S. Hong, E. Jeffrey, S. Kim, K. Kechedzhi, F. Kostritsa, P. Laptev, A. Megrant, X. Mi, J. Mutus, O. Naaman, M. Neeley, C. Neill, M. Niu, A. Paler, N. Redd, P. Roushan, T. C. White, J. Yao, P. Yeh, A. Zalcman, Y. Chen, V. N. Smelyanskiy, J. M. Martinis, H. Neven, J. Kelly, A. N. Korotkov, A. G. Petukhov, and R. Barends. Removing leakage-induced correlated errors in superconducting quantum error correction. eng. *Nature Communications*, 12(1):1761–1761, 2021. ISSN: 2041-1723. DOI: `10.1038/s41467-021-21982-y`.

[12] J. A. Schreier, A. A. Houck, J. Koch, D. I. Schuster, B. R. Johnson, J. M. Chow, J. M. Gambetta, J. Majer, L. Frunzio, M. H. Devoret, S. M. Girvin, and R. J. Schoelkopf. Suppressing charge noise decoherence in superconducting charge qubits. *Phys. Rev. B*, 77:180502, 18, May 2008. DOI: `10.1103/PhysRevB.77.180502`.

[13] I. Chiorescu, Y. Nakamura, C. J. P. M. Harmans, and J. E. Mooij. Coherent quantum dynamics of a superconducting flux qubit. eng. *Science (American Association for the Advancement of Science)*, 299(5614):1869–1871, 2003. ISSN: 0036-8075. DOI: `10.1126/science.1081045`.

[14] P. Jurcevic, A. Javadi-Abhari, L. S. Bishop, I. Lauer, D. F. Bogorin, M. Brink, L. Capelluto, O. Günlük, T. Itoko, N. Kanazawa, A. Kandala, G. A. Keefe, K. Krsulich, W. Landers, E. P. Lewandowski, D. T. McClure, G. Nannicini, A. Narasgond, H. M. Nayfeh, E. Pritchett, M. B. Rothwell, S. Srinivasan, N. Sundaresan, C. Wang, K. X. Wei, C. J. Wood, J.-B. Yau, E. J. Zhang, O. E. Dial, J. M. Chow, and J. M. Gambetta. Demonstration of quantum volume 64 on a superconducting quantum computing system. eng. *Quantum Science and Technology*, 6(2):25020–, 2021. ISSN: 2058-9565. DOI: `10.1088/2058-9565/abe519`.

[15] C. E. Bradley, J. Randall, M. H. Abobeih, R. C. Berrevoets, M. J. Degen, M. A. Bakker, M. Markham, D. J. Twitchen, and T. H. Taminiau. A ten-qubit solid-state spin register with quantum memory up to one minute. *Phys. Rev. X*, 9:031045, 3, Sept. 2019. DOI: `10.1103/PhysRevX.9.031045`.

[16] H. Kaufmann, T. Ruster, C. T. Schmiegelow, M. A. Luda, V. Kaushal, J. Schulz, D. von Lindenfels, F. Schmidt-Kaler, and U. G. Poschinger. Fast ion swapping for quantum-information processing. *Phys. Rev. A*, 95:052319, 5, May 2017. DOI: `10.1103/PhysRevA.95.052319`.

[17] M. H. Abobeih, J. Randall, C. E. Bradley, H. P. Bartling, M. A. Bakker, M. J. Degen, M. Markham, D. J. Twitchen, and T. H. Taminiau. Atomic-scale imaging of a 27-nuclear-spin cluster using a quantum sensor. eng. *Nature (London)*, 576(7787):411–415, 2019. ISSN: 0028-0836. DOI: `10.1038/s41586-019-1834-7`.

[18] H. Kaufmann, T. Ruster, C. T. Schmiegelow, M. A. Luda, V. Kaushal, J. Schulz, D. von Lindenfels, F. Schmidt-Kaler, and U. G. Poschinger. Scalable creation of long-lived multipartite entanglement. *Phys. Rev. Lett.*, 119:150503, 15, Oct. 2017. DOI: `10.1103/PhysRevLett.119.150503`.

[19] S. Kimmel, M. P. da Silva, C. A. Ryan, B. R. Johnson, and T. Ohki. Robust extraction of tomographic information via randomized benchmarking. *Phys. Rev. X*, 4:011050, 1, Mar. 2014. DOI: `10.1103/PhysRevX.4.011050`.

[20] B. E. Kane. A silicon-based nuclear spin quantum computer. eng. *Nature (London)*, 393(6681):133–137, 1998. ISSN: 0028-0836. DOI: `10.1038/30156`.

[21] L. M. K. Vandersypen and I. L. Chuang. Nmr techniques for quantum control and computation. *Rev. Mod. Phys.*, 76:1037–1069, 4, Jan. 2005. DOI: `10.1103/RevModPhys.76.1037`.

[22] K. Saeedi, S. Simmons, J. Z. Salvail, P. Dluhy, H. Riemann, N. V. Abrosimov, P. Becker, H.-J. Pohl, J. J. L. Morton, and M. L. W. Thewalt. Room-temperature quantum bit storage exceeding 39 minutes using ionized donors in silicon-28. eng. *Science (American Association for the Advancement of Science)*, 342(6160):830–833, 2013. ISSN: 0036-8075. DOI: `10.1126/science.1239584`.

[23] V. Filidou, S. Simmons, S. D. Karlen, F. Giustino, H. L. Anderson, and J. J. L. Morton. Ultrafast entangling gates between nuclear spins using photoexcited triplet states. eng. *Nature Physics*, 8(8):596–600, 2012. ISSN: 1745-2473. DOI: `0.1038/nphys2353`.

[24] K. R. Brown, A. C. Wilson, Y. Colombe, C. Ospelkaus, A. M. Meier, E. Knill, D. Leibfried, and D. J. Wineland. Single-qubit-gate error below $\mathbf{10^{-4}}$ in a trapped ion. *Phys. Rev. A*, 84:030303, 3, Sept. 2011. DOI: `10.1103/PhysRevA.84.030303`.

[25] M. Rowe, C. J. Myatt, C. Monroe, B. E. King, D. Kielpinski, V. Meyer, Q. A. Turchette, D. J. Wineland, C. A. Sackett, W. M. Itano, and C. Langer. Experimental entanglement of four particles. eng. *Nature (London)*, 404(6775):256–259, 2000. ISSN: 0028-0836. DOI: `10.1038/35005011`.

[26] C. Monroe, D. M. Meekhof, B. E. King, W. M. Itano, and D. J. Wineland. Demonstration of a fundamental quantum logic gate. *Phys. Rev. Lett.*, 75:4714–4717, 25, Dec. 1995. DOI: `10.1103/PhysRevLett.75.4714`.

[27] Q. A. Turchette, C. S. Wood, B. E. King, C. J. Myatt, D. Leibfried, W. M. Itano, C. Monroe, and D. J. Wineland. Deterministic entanglement of two trapped ions. *Phys. Rev. Lett.*, 81:3631–3634, 17, Oct. 1998. DOI: `10.1103/PhysRevLett.81.3631`.

[28] R. Raussendorf and J. Harrington. Fault-tolerant quantum computation with high threshold in two dimensions. *Phys. Rev. Lett.*, 98:190504, 19, May 2007. DOI: `10.1103/PhysRevLett.98.190504`.

[29] C. F. Roos, J. Benhelm, G. Kirchmair, and R. Blatt. Towards fault-tolerant quantum computing with trapped ions. eng. *Nature Physics*, 4(6):463–466, 2008. ISSN: 1745-2473. DOI: `10.1038/nphys9611`.

[30] H. Häffner, S. Gulde, M. Riebe, G. Lancaster, C. Becher, J. Eschner, F. Schmidt-Kaler, and R. Blatt. Precision measurement and compensation of optical stark shifts for an ion-trap quantum processor. *Phys. Rev. Lett.*, 90:143602, 14, Apr. 2003. DOI: `10.1103/PhysRevLett.90.143602`.

[31] J. I. Cirac and P. Zoller. Quantum computations with cold trapped ions. *Phys. Rev. Lett.*, 74:4091–4094, 20, May 1995. DOI: 10.1103/PhysRevLett.74.4091.

[32] D. J. Wineland, C. Monroe, W. M. Itano, D. Leibfried, B. E. King, and D. M. Meekhof. Experimental issues in coherent quantum-state manipulation of trapped atomic ions. eng. *Journal of Research of the National Institute of Standards and Technology*, 103(3):259–328, 1998. ISSN: 1044-677X. DOI: 10.6028/jres.103.019.

[33] A. Sørensen and K. Mølmer. Quantum computation with ions in thermal motion. *Phys. Rev. Lett.*, 82:1971–1974, 9, Mar. 1999. DOI: 10.1103/PhysRevLett. 82.1971.

[34] K. Mølmer and A. Sørensen. Multiparticle entanglement of hot trapped ions. *Phys. Rev. Lett.*, 82:1835–1838, 9, Mar. 1999. DOI: 10.1103/PhysRevLett. 82.1835.

[35] M. Rowe, C. J. Myatt, C. Monroe, B. E. King, D. Kielpinski, V. Meyer, Q. A. Turchette, D. J. Wineland, C. A. Sackett, W. M. Itano, and C. Langer. Experimental entanglement of four particles. eng. *Nature (London)*, 404(6775):256–259, 2000. ISSN: 0028-0836. DOI: 10.1038/35005011.

[36] A. Erhard, J. J. Wallman, L. Postler, M. Meth, R. Stricker, E. A. Martinez, P. Schindler, T. Monz, J. Emerson, and R. Blatt. Characterizing large-scale quantum computers via cycle benchmarking. eng. *Nature Communications*, 10(1):5347–7, 2019. ISSN: 2041-1723. DOI: 10.1038/s41467-019-13068-7.

[37] J. P. Gaebler, T. R. Tan, Y. Lin, Y. Wan, R. Bowler, A. C. Keith, S. Glancy, K. Coakley, E. Knill, D. Leibfried, and D. J. Wineland. High-fidelity universal gate set for $^9\text{Be}^+$ ion qubits. *Phys. Rev. Lett.*, 117:060505, 6, Aug. 2016. DOI: 10.1103/PhysRevLett.117.060505.

[38] C. F. Roos. Ion trap quantum gates with amplitude-modulated laser beams. eng. *New Journal of Physics*, 10(1):013002–, 2008. ISSN: 1367-2630. DOI: 10.1088/1367-2630/10/1/013002.

[39] F. Haddadfarshi and F. Mintert. High fidelity quantum gates of trapped ions in the presence of motional heating. eng. *New journal of physics*, 18(12):123007–, 2016. ISSN: 1367-2630. DOI: 10.1088/1367-2630/18/12/123007.

[40] E. Samuel. On the nature of the molecular forces which regulate the constitution of the luminferous ether. eng. *Transactions of the Cambridge Philosophical Society*, 7:97–112, 1842.

[41]   H. Dehmelt. Radiofrequency spectroscopy of stored ions i: storage**part ii: spectroscopy is now scheduled to appear in volume v of this series. In D. Bates and I. Estermann, editors. Volume 3, Advances in Atomic and Molecular Physics, pages 53–72. Academic Press, 1968. DOI: `10.1016/S0065-2199(08)60170-0`.

[42]   P. Wolfgang and S. Helmut. Notizen: ein neues Massenspektrometer ohne Magnetfeld. *Zeitschrift für Naturforschung A*, 8(7):448–450, 1953. DOI: `doi:10.1515/zna-1953-0710`.

[43]   M. Knoop, N. Madsen, and R. C. Thompson. *Trapped Charged Particles-A Graduate Textbook with Problems and Solutions*. World Scientific, 2016.

[44]   R. E. March, J. F. J. Todd, and G. L. Glish. Quadrupole ion trap mass spectrometry, 2nd edition. eng. *Journal of the American Society for Mass Spectrometry*, 17(5):746–747, 2006. ISSN: 1044-0305.

[45]   S. Gulde. *Experimental Realisation of Quantum Gates and the Deutsch-Jozsa Algorithm with Trapped $^{40}Ca^+$ Ions*. PhD thesis, Universität Innsbruck, 2003.

[46]   D. James. Quantum dynamics of cold trapped ions with application to quantum computation. *Applied Physics. B, Lasers and Optics*, 66(2):181–190, 1998. DOI: `10.1007/s003400050373`.

[47]   P. J. Bardroff, C. Leichtle, G. Schrade, and W. P. Schleich. Endoscopy in the paul trap: measurement of the vibratory quantum state of a single ion. *Phys. Rev. Lett.*, 77:2198–2201, 11, Sept. 1996. DOI: `10.1103/PhysRevLett.77.2198`.

[48]   J. Heinrich. *A Be$^+$ Ion Trap for H2+ Spectroscopy*. PhD thesis, Sorbonne University, Apr. 2018.

[49]   F. G. Major, V. N. Gheorghe, G. Werth, S. P. F. G. Major, G. Werth, et al. *Charged particle traps: physics and techniques of charged particle field confinement*, volume 37. Springer Science & Business Media, 2005.

[50]   D. Gerlich. Inhomogeneous rf fields: a versatile tool for the study of processes with slow ions. *Advances in Chemical Physics*, 82:1–176, 1992.

[51]   P. Staanum, I. S. Jensen, R. G. Martinussen, D. Voigt, and M. Drewsen. Lifetime measurement of the metastable $3d\,^2D_{5/2}$ state in the ^{40}Ca$^+$ ion using the shelving technique on a few-ion string. *Phys. Rev. A*, 69:032503, 3, Mar. 2004. DOI: `10.1103/PhysRevA.69.032503`.

[52]   T. Sauter, W. Neuhauser, R. Blatt, and P. E. Toschek. Observation of quantum jumps. *Phys. Rev. Lett.*, 57:1696–1698, 14, Oct. 1986. DOI: `10.1103/PhysRevLett.57.1696`.

[53] J. C. Bergquist, R. G. Hulet, W. M. Itano, and D. J. Wineland. Observation of quantum jumps in a single atom. *Phys. Rev. Lett.*, 57:1699–1702, 14, Oct. 1986. DOI: `10.1103/PhysRevLett.57.1699`.

[54] W. Nagourney, J. Sandberg, and H. Dehmelt. Shelved optical electron amplifier: observation of quantum jumps. *Phys. Rev. Lett.*, 56:2797–2799, 26, June 1986. DOI: `10.1103/PhysRevLett.56.2797`.

[55] N. V. Vitanov, T. Halfmann, B. W. Shore, and K. Bergmann. Laser-induced population transfer by adiabatic passage techniques. *Annual Review of Physical Chemistry*, 52(1):763–809, 2001.

[56] O. Corfield. *Quantum Coherence in Trapped Ions*. PhD thesis, Imperial College London, 2022.

[57] T. G. Ballance, J. F. Goodwin, B. Nichol, L. J. Stephenson, C. J. Ballance, and D. M. Lucas. A short response time atomic source for trapped ion experiments. eng. *Review of Scientific Instruments*, 89(5):053102–053102, 2018. ISSN: 0034-6748. DOI: `10.1063/1.5025713`.

[58] D. M. Lucas, A. Ramos, J. P. Home, M. J. McDonnell, S. Nakayama, J.-P. Stacey, S. C. Webster, D. N. Stacey, and A. M. Steane. Isotope-selective photoionization for calcium ion trapping. *Phys. Rev. A*, 69:012711, 1, Jan. 2004. DOI: `10.1103/PhysRevA.69.012711`.

[59] S. Gulde, D. Rotter, P. Barton, F. Schmidt-Kaler, R. Blatt, and W. Hogervorst. Simple and efficient photo-ionization loading of ions for precision ion-trapping experiments. *Applied Physics B*, 73(8):861–863, 2001.

[60] J. F. Goodwin. *Sideband Cooling to the Quantum Ground State in a Penning Trap*. PhD thesis, Imperial College London, 2015.

[61] D. J. Wineland and W. M. Itano. Laser cooling of atoms. *Phys. Rev. A*, 20:1521–1540, 4, Oct. 1979. DOI: `10.1103/PhysRevA.20.1521`.

[62] K. E. Cahill and R. J. Glauber. Ordered expansions in boson amplitude operators. *Phys. Rev.*, 177:1857–1881, 5, Jan. 1969. DOI: `10.1103/PhysRev.177.1857`.

[63] M. K. Joshi, P. Hrmo, V. Jarlaud, F. Oehl, and R. C. Thompson. Population dynamics in sideband cooling of trapped ions outside the Lamb-Dicke regime. *Phys. Rev. A*, 99:013423, 1, Jan. 2019. DOI: `10.1103/PhysRevA.99.013423`.

[64] G. Morigi, J. Eschner, J. I. Cirac, and P. Zoller. Laser cooling of two trapped ions: sideband cooling beyond the Lamb-Dicke limit. *Phys. Rev. A*, 59:3797–3808, 5, May 1999. DOI: `10.1103/PhysRevA.59.3797`.

[65] G. Morigi, J. I. Cirac, M. Lewenstein, and P. Zoller. Ground-state laser cooling beyond the Lamb-Dicke limit. eng. *Europhysics Letters*, 39(1):13–18, 1997. ISSN: 0295-5075. DOI: `10.1209/0295-5075/23/1/001`.

[66] D. F. James and J. Jerke. Effective Hamiltonian theory and its applications in quantum information. *Canadian Journal of Physics*, 85(6):625–632, 2007. DOI: `10.1139/p07-060`. eprint: `https://doi.org/10.1139/p07-060`.

[67] R. A. Cline, J. D. Miller, M. R. Matthews, and D. J. Heinzen. Spin relaxation of optically trapped atoms by light scattering. *Opt. Lett.*, 19(3):207–209, Feb. 1994. DOI: `10.1364/OL.19.000207`.

[68] R. Ozeri, C. Langer, J. D. Jost, B. DeMarco, A. Ben-Kish, B. R. Blakestad, J. Britton, J. Chiaverini, W. M. Itano, D. B. Hume, D. Leibfried, T. Rosenband, P. O. Schmidt, and D. J. Wineland. Hyperfine coherence in the presence of spontaneous photon scattering. *Phys. Rev. Lett.*, 95:030403, 3, July 2005. DOI: `10.1103/PhysRevLett.95.030403`.

[69] R. Ozeri, C. Langer, J. D. Jost, B. DeMarco, A. Ben-Kish, B. R. Blakestad, J. Britton, J. Chiaverini, W. M. Itano, D. B. Hume, D. Leibfried, T. Rosenband, P. O. Schmidt, and D. J. Wineland. Hyperfine coherence in the presence of spontaneous photon scattering. *Phys. Rev. Lett.*, 95:030403, 3, July 2005. DOI: `10.1103/PhysRevLett.95.030403`.

[70] H. Uys, M. J. Biercuk, A. P. VanDevender, C. Ospelkaus, D. Meiser, R. Ozeri, and J. J. Bollinger. Decoherence due to elastic rayleigh scattering. *Phys. Rev. Lett.*, 105:200401, 20, Nov. 2010. DOI: `10.1103/PhysRevLett.105.200401`.

[71] D. Wineland and H. Dehmelt. Line shifts and widths of axial, cyclotron and g-2 resonances in tailored, stored electron (ion) cloud. *International Journal of Mass Spectrometry and Ion Physics*, 16(3):338–342, 1975. ISSN: 0020-7381. DOI: `10.1016/0020-7381(75)87031-8`.

[72] W. D. Phillips. Nobel lecture: laser cooling and trapping of neutral atoms. *Rev. Mod. Phys.*, 70:721–741, 3, July 1998. DOI: `10.1103/RevModPhys.70.721`.

[73] S. Stenholm. The semiclassical theory of laser cooling. *Rev. Mod. Phys.*, 58:699–739, 3, July 1986. DOI: `10.1103/RevModPhys.58.699`.

[74] A. J. Rasmusson, M. D'Onofrio, Y. Xie, J. Cui, and P. Richerme. Optimized pulsed sideband cooling and enhanced thermometry of trapped ions. *Phys. Rev. A*, 104:043108, 4, Oct. 2021. DOI: `10.1103/PhysRevA.104.043108`.

[75] M. Joshi. *Coherent Dynamics of Trapped Ions Within and Outside the Lamb-Dicke Regime*. PhD thesis, Imperial College London, 2018.

[76] P. Hrmo. *Ground state cooling of the radial motion of a single ion in a penning trap and coherent manipulation of small numbers of ions*. eng. PhD thesis, 2018.

[77] I. Chang. Acousto-optic devices and applications. *Handbook of optics*, 2:12–1, 1995.

[78] K. Mølmer and A. Sørensen. Multiparticle entanglement of hot trapped ions. *Phys. Rev. Lett.*, 82:1835–1838, 9, Mar. 1999. DOI: `10.1103/PhysRevLett.82.1835`.

[79] A. V. Akimov, N. N. Kolachevsky, A. V. Sokolov, A. N. Matveev, S. I. Kanorsky, R. A. Kits, A. A. Papchenko, and V. N. Sorokin. Spectroscopy of coherent population trapping with a light source based on a femtosecond laser. rus. *Quantum Electronics (Woodbury, N.Y.)*, 34(10):983–988, 2004. ISSN: 1063-7818. DOI: `10.1016/S0079-6638(08)70531-66`.

[80] J. Roßnagel, K. N. Tolazzi, F. Schmidt-Kaler, and K. Singer. Fast thermometry for trapped ions using dark resonances. eng. *New Journal of Physics*, 17(4):45004–, 2015. ISSN: 1367-2630. DOI: `10.1088/1367-2630/17/4/045004`.

[81] J. Toba. *Design of an imaging system and implementation of photoionisation for a linear Paul trap,* Master's thesis, Imperial College London, 2019.

[82] K. Deng, Y. L. Sun, W. H. Yuan, Z. T. Xu, J. Zhang, Z. H. Lu, and J. Luo. A modified model of helical resonator with predictable loaded resonant frequency and q-factor. eng. *Review of Scientific Instruments*, 85(10):104706–104706, 2014. ISSN: 0034-6748. DOI: `10.1063/1.4897478`.

[83] J. Keller, H. L. Partner, T. Burgermeister, and T. Mehlstäubler. Precise determination of micromotion for trapped-ion optical clocks. *Journal of Applied Physics*, 118(10):104501, 2015.

[84] D. Berkeland, J. Miller, J. C. Bergquist, W. M. Itano, and D. J. Wineland. Minimization of ion micromotion in a paul trap. *Journal of Applied Physics*, 83(10):5025–5033, 1998.

[85] S. Mavadia. *Motional Sideband Spectra and Coulomb Crystals in a Penning Trap*. PhD thesis, Imperial College London, 2013.

[86] R. W. P. Drever, J. L. Hall, F. V. Kowalski, J. Hough, G. M. Ford, A. J. Munley, and H. Ward. Laser phase and frequency stabilization using an optical resonator. eng. *Applied Physics B Photophysics and Laser Chemistry*, 31(2):97–105, 1983. ISSN: 0721-7269. DOI: `10.1007/BF00702605`.

[87]   E. D. Black. An introduction to pound–drever–hall laser frequency stabilization. eng. *American Journal of Physics*, 69(1):79–87, 2001. ISSN: 0002-9505. DOI: `10.1119/1.1286663`.

[88]   M. Nickerson. A review of Pound-Drever-Hall laser frequency locking. *JILA, University of Colorado and NIST*, 2019.

[89]   C. Monroe, W. C. Campbell, L.-M. Duan, Z.-X. Gong, A. V. Gorshkov, P. W. Hess, R. Islam, K. Kim, N. M. Linke, G. Pagano, P. Richerme, C. Senko, and N. Y. Yao. Programmable quantum simulations of spin systems with trapped ions. *Rev. Mod. Phys.*, 93:025001, 2, Apr. 2021. DOI: `10.1103/RevModPhys.93.025001`.

[90]   C. D. Bruzewicz, J. Chiaverini, R. McConnell, and J. M. Sage. Trapped-ion quantum computing: progress and challenges. eng. *Applied Physics Reviews*, 6(2):21314–, 2019. ISSN: 1931-9401.

[91]   M. A. Nielsen. *Quantum computation and quantum information.* eng. Cambridge University Press, Cambridge, 10th anniversary ed. Edition, 2010. ISBN: 9781107002173.

[92]   A. Ben-Kish, B. DeMarco, V. Meyer, M. Rowe, J. Britton, W. M. Itano, B. M. Jelenkovi ć, C. Langer, D. Leibfried, T. Rosenband, and D. J. Wineland. Experimental demonstration of a technique to generate arbitrary quantum superposition states of a harmonically bound spin-1/2 particle. *Phys. Rev. Lett.*, 90:037902, 3, Jan. 2003. DOI: `10.1103/PhysRevLett.90.037902`.

[93]   B. Kneer and C. K. Law. Preparation of arbitrary entangled quantum states of a trapped ion. *Phys. Rev. A*, 57:2096–2104, 3, Mar. 1998. DOI: `10.1103/PhysRevA.57.2096`.

[94]   S. A. Gardiner, J. I. Cirac, and P. Zoller. Nonclassical states and measurement of general motional observables of a trapped ion. *Phys. Rev. A*, 55:1683–1694, 3, Mar. 1997. DOI: `10.1103/PhysRevA.55.1683`.

[95]   A. Steane, C. F. Roos, D. Stevens, A. Mundt, D. Leibfried, F. Schmidt-Kaler, and R. Blatt. Speed of ion-trap quantum-information processors. *Phys. Rev. A*, 62:042305, 4, Sept. 2000. DOI: `10.1103/PhysRevA.62.042305`.

[96]   F. Motzoi and F. K. Wilhelm. Improving frequency selection of driven pulses using derivative-based transition suppression. *Phys. Rev. A*, 88:062318, 6, Dec. 2013. DOI: `10.1103/PhysRevA.88.062318`.

[97]   J. A. D. Randall. *High-fidelity entanglement of trapped ions using long-wavelength radiation.* eng. PhD thesis, 2016.

[98] S. Szalay. Multipartite entanglement measures. *Phys. Rev. A*, 92:042329, 4, Oct. 2015. DOI: `10.1103/PhysRevA.92.042329`.

[99] F. Levi and F. Mintert. A quantitative theory of coherent delocalization. eng. *New journal of physics*, 16(3):33007–14, 2014. ISSN: 1367-2630. DOI: `10.1088/1367-2630/16/3/033007`.

[100] O. Corfield, J. Lishman, C. Lee, J. M. Toba, G. Porter, J. M. Heinrich, S. C. Webster, F. Mintert, and R. C. Thompson. Certifying multilevel coherence in the motional state of a trapped ion. *PRX Quantum*, 2:040359, 4, Dec. 2021. DOI: `10.1103/PRXQuantum.2.040359`.

[101] B. Dive, N. Koukoulekidis, S. Mousafeiris, and F. Mintert. Characterization of multilevel quantum coherence without ideal measurements. *Phys. Rev. Research*, 2:013220, 1, Feb. 2020. DOI: `10.1103/PhysRevResearch.2.013220`.

[102] P. M. Lee. *Bayesian statistics : an introduction.* eng. Wiley, Chichester, 4th ed. Edition, 2012. ISBN: 9781118359754.

[103] C. Granade, C. Ferrie, I. Hincks, S. Casagrande, T. Alexander, J. Gross, M. Kononenko, and Y. Sanders. Qinfer: statistical inference software for quantum applications. *Quantum*, 1:5, 2017. DOI: `10.22331/q-2017-04-25-5`.

[104] J. S. Liu and R. Chen. Sequential monte carlo methods for dynamic systems. eng. *Journal of the American Statistical Association*, 93(443):1032–1044, 1998. ISSN: 0162-1459. DOI: `10.1080/01621459.1998.10473765`.

[105] D. Mayne. A solution of the smoothing problem for linear dynamic systems. eng. *Automatica (Oxford)*, 4(2):73–92, 1966. ISSN: 0005-1098. DOI: `10.1016/0005-1098(66)90019-7`.

[106] J. E. Handschin and D. Q. Mayne. Monte carlo techniques to estimate the conditional expectation in multi-stage non-linear filtering. eng. *International Journal of Control*, 9(5):547–559, 1969. ISSN: 0020-7179. DOI: `10.1080/00207176908905777`.

[107] A. Beskos, D. Crisan, and A. Jasra. On the stability of sequential monte carlo methods in high dimensions. eng. *The Annals of Applied Probability*, 24(4):1396–1445, 2014. ISSN: 1050-5164. DOI: `10.1214/13-AAP951`.

[108] J. Liu and M. West. Combined parameter and state estimation in simulation-based filtering. In *Sequential Monte Carlo methods in practice*, pages 197–223. Springer, 2001. DOI: `10.1007/978-1-4757-3437-9_10`.

[109] B. E. King, C. S. Wood, C. J. Myatt, Q. A. Turchette, D. Leibfried, W. M. Itano, C. Monroe, and D. J. Wineland. Cooling the collective motion of trapped ions to initialize a quantum register. *Phys. Rev. Lett.*, 81:1525–1528, 7, Aug. 1998. DOI: `10.1103/PhysRevLett.81.1525`.

[110] E. Farhi, J. Goldstone, S. Gutmann, J. Lapan, A. Lundgen, and D. Preda. A quantum adiabatic evolution algorithm applied to random instances of an np-complete problem. eng. *Science (American Association for the Advancement of Science)*, 292(5516):472–476, 2001. ISSN: 0036-8075. DOI: `10.1126/science.10577`.

[111] I. M. Georgescu, S. Ashhab, and F. Nori. Quantum simulation. *Rev. Mod. Phys.*, 86:153–185, 1, Mar. 2014. DOI: `10.1103/RevModPhys.86.153`.

[112] S. Zaiser, C. T. Cheung, S. Yang, D. B. R. Dasari, S. Raeisi, and J. Wrachtrup. Cyclic cooling of quantum systems at the saturation limit. eng. *NPJ Quantum Information*, 7(1):1–7, 2021. ISSN: 2056-6387. DOI: `10.1038/nphoton.2011.35`.

[113] H. G. Dehmelt and F. L. Walls. "bolometric" technique for the rf spectroscopy of stored ions. *Phys. Rev. Lett.*, 21:127–131, 3, July 1968. DOI: `10.1103/PhysRevLett.21.127`.

[114] D. J. Wineland and H. G. Dehmelt. Principles of the stored ion calorimeter. eng. *Journal of Applied Physics*, 46(2):919–930, 1975. ISSN: 0021-8979. DOI: `10.1063/1.321602`.

[115] W. M. Itano, J. C. Bergquist, J. J. Bollinger, and D. J. Wineland. Cooling methods in ion traps. eng. *Physica Scripta*, 1995:106–120, 1995. ISSN: 1402-4896. DOI: `10.1088/0031-8949/1995/T59/013`.

[116] Y. Li, L.-A. Wu, Y.-D. Wang, and L.-P. Yang. Nondeterministic ultrafast ground-state cooling of a mechanical resonator. *Phys. Rev. B*, 84:094502, 9, Sept. 2011. DOI: `10.1103/PhysRevB.84.094502`.

[117] D. D. B. Rao, S. A. Momenzadeh, and J. Wrachtrup. Heralded control of mechanical motion by single spins. *Phys. Rev. Lett.*, 117:077203, 7, Aug. 2016. DOI: `10.1103/PhysRevLett.117.077203`.

[118] V. Montenegro, R. Coto, V. Eremeev, and M. Orszag. Ground-state cooling of a nanomechanical oscillator with N spins. *Phys. Rev. A*, 98:053837, 5, Nov. 2018. DOI: `10.1103/PhysRevA.98.053837`.

[119] C. Bergenfeldt and K. Mølmer. Cooling a micromechanical resonator to its ground state by measurement and feedback. *Phys. Rev. A*, 80:043838, 4, Oct. 2009. DOI: `10.1103/PhysRevA.80.043838`.

[120] R. Puebla, O. Abah, and M. Paternostro. Measurement-based cooling of a nonlinear mechanical resonator. *Phys. Rev. B*, 101:245410, 24, June 2020. DOI: `10.1103/PhysRevB.101.245410`.

[121] M. Vanner, J. Hofer, G. Cole, and M. Aspelmeyer. Cooling-by-measurement and mechanical state tomography via pulsed optomechanics. *Nature Communications*, 4(1):1–8, 2013.

[122] A. Abragam. *The principles of nuclear magnetism*. eng. International series of monographs on physics. Clarendon Press, Oxford, 1961.

[123] F. Bloch. Nuclear induction. *Phys. Rev.*, 70:460–474, 7-8, Oct. 1946. DOI: `10.1103/PhysRev.70.460`.

[124] E. Treacy. Adiabatic inversion with light pulses. eng. *Physics Letters. A*, 27(7):421–422, 1968. ISSN: 0375-9601. DOI: `10.1016/S0079-6638(08)70531-66`.

[125] T. Watanabe, S. Nomura, K. Toyoda, and S. Urabe. Sideband excitation of trapped ions by rapid adiabatic passage for manipulation of motional states. *Phys. Rev. A*, 84:033412, 3, Sept. 2011. DOI: `10.1103/PhysRevA.84.033412`.